Title: Organism-wide cellular dynamics and epigenomic remodeling in mammalian aging

Authors: Ziyu Lu[1,2], Zehao Zhang[1,2], Zihan Xu[1,2], Abdulraouf Abdulraouf[1,3], Wei Zhou[1,4]*, Junyue Cao[1,4,5]*

Affiliations:
[1]Laboratory of Single Cell Genomics and Population Dynamics, The Rockefeller University, New York, NY, USA
[2]The David Rockefeller Graduate Program in Bioscience, The Rockefeller University, New York, NY, USA
[3]The Tri-Institutional M.D-Ph.D Program, New York, NY, USA
[4]Senior author
[5]Lead Contact
*Correspondence: wzhou@rockefeller.edu (W.Z.), jcao@rockefeller.edu (J.C.)

Abstract:
Aging leads to functional decline across tissues, often accompanied by profound changes in cellular composition and cell-intrinsic molecular states. However, a comprehensive catalog of how the population of individual cell types change with age and the associated epigenomic dynamics is lacking. Here, we constructed a single-cell chromatin accessibility atlas consisting of ~7 million cells from 21 tissue types spanning three age groups in both sexes. This dataset revealed 536 main cell types and 1,828 finer-grained subtypes, defined by unique chromatin accessibility landscapes at ~1.3 million cis-regulatory elements. We observed widespread remodeling of immune lineages, with increases in plasma cells and macrophages, and depletion of T and B cell progenitors. Additionally, non-immune cell populations, including kidney podocytes, ovary granulosa cells, muscle tenocytes and lung aerocytes, showed marked reductions with age. Meanwhile, many subtypes changed synchronously across multiple organs, underscoring the potential influence of systemic inflammatory signals or hormonal cues. At the molecular level, aging was marked by thousands of differentially accessible regions, with the most concordant changes shared across cell types linked to genes related to inflammation or development. Putative upstream factors, such as intrinsic shifts in transcription factor usages and extrinsic cytokine signatures, were identified. Notably, around 40% of aging-associated main cell types and subtypes showed sex-dependent differences, with tens of thousands of chromatin accessibility peaks altered exclusively in one sex. Together, these findings present a comprehensive framework of how aging reshapes the chromatin landscape and cellular composition across diverse tissues, offering a comprehensive resource for understanding the molecular and cellular programs underlying aging and supporting the exploration of targeted therapeutic strategies to address age-related dysfunction.

Main Text:

Introduction:

Aging is the leading risk factor for many diseases, including neurodegenerative disorders, cardiovascular diseases, metabolic conditions, and cancer(*1*). This association underscores the potential of therapies targeting the aging process itself to delay or prevent various age-related diseases, rather than focusing on specific diseases or organs. However, this approach is challenging due to the complexity of aging, which involves widespread changes across various systems and organs (*2*, *3*). Each organ consists of hundreds of unique cellular states with specialized functions, each undergoing varied aging-associated changes. Therefore, a systematic characterization of aging-associated cell states—including their genetic and epigenetic alterations underlying population dynamics—is essential for identifying cellular and molecular targets that could guide the development of targeted therapeutic interventions.

Recent advancements in single-cell genomics have significantly enhanced our ability to map aging-associated cell states. For example, single-cell transcriptomics analyses have enabled us to profile alterations in thousands of genes across millions of cells as they age (*4*–*7*) . However, these analyses typically focus on protein-coding genes and overlook the impact of non-coding genetic elements in regulating cell-type-specific dynamics in aging. Moreover, current single-cell atlas studies often focus on a limited set of organs (*e.g.,* liver, kidney), largely because some other tissues, like the pancreas, are difficult to profile due to high RNA degradation (*8*, *9*). This limitation impedes our ability to assess aging across the entire organism. As a result, we still lack a comprehensive analysis of cell population dynamics and chromatin landscape changes throughout the mammalian body for understanding how non-coding regions, particularly cis-regulatory DNA elements, affect cell states and population dynamics as they age.

Single-cell ATAC-seq(*10*), which analyzes genome-wide chromatin accessibility at the single-cell level, has enabled the mapping of the cell-type-specific chromatin landscape in a range of mammalian tissues(*11*–*14*), aiding in the identification of disease-associated non-coding regions and their corresponding cell types. Among varied scATAC-seq approaches, single-cell ATAC-seq by combinatorial indexing (*sci-ATAC-seq*), allows for high-throughput analysis of tens of thousands of cells from highly heterogeneous tissues in a single experiment(*11*). With a further optimized version of sci-ATAC-seq (EasySci-ATAC), we recently mapped the cell-type-specific chromatin landscape and aging-associated cell population changes in the mammalian brain(*15*). Building on this work, we now extend our analysis beyond a single organ to explore aging-associated changes in cell populations across the entire organism, identifying changes in cellular chromatin states, population dynamics, and associated genetic elements—including cis-regulatory elements and transcription factor motifs—across different ages and sexes.

Results

An organismal, single-cell chromatin accessibility atlas of aging

To map aging-associated cell population dynamics and the cell-type-specific chromatin landscape changes at the organismal scale, we developed an optimized *EasySci-ATAC(15)* protocol that enables high-throughput analysis of mouse tissues across the entire organism (**Methods**). Next we applied this approach to profile 552 samples collected from thirty-two individual mice representing three age groups (1-month, 5-month, and 21-month)(**Table S1**). Each group contained 8-12 sex-balanced biological replicates, except for the female ovary and uterus samples. Twenty-one different tissue types spanning major biological systems were profiled, including the immune system (*i.e.,* bone marrow, spleen, thymus), the cardiovascular system (*i.e.,* heart), the respiratory system (*i.e.,* lung), the digestive system (*i.e.,* liver, pancreas, esophagus, stomach, intestine, cecum, colon), the urinary system (*i.e.,* kidney), the sensory system (*i.e.,* eye), the reproductive system (*i.e.,* ovary/uterus), the musculoskeletal system (*i.e.,* muscle), the integumentary system (*i.e.,* skin), and the adipose tissues, which includes brown adipose tissue (BAT) and white adipose tissues (WAT) in various anatomical locations (*i.e.,* gonadal, inguinal, and mesenteric) (**Fig. 1A**). Of note, the brain was not included here, as it has been extensively analyzed in our previous study(*15*). Also, to enable the investigation of newborn cell dynamics in a companion study, we labeled mice with 5-Ethynyl-2-deoxyuridine (EdU) before tissue collection, similar to our previous work (*16*). This allowed single-cell chromatin accessibility profiling of both sorted DAPI singlets ('all' cells, this study) and EdU+ nuclei ('newborn' cells, analyzed in the companion study) from the same set of samples.

The extracted nuclei from each tissue sample were sorted and combinatorial barcoded through indexed tagmentation, indexed ligation, and indexed PCR (**Fig. 1A**). The resulting libraries were sequenced on the Illumina NovaSeq 6000 system, yielding a total of 95 billion paired-end raw reads. After filtering out low-quality cells and doublets similar to our previous study (*15*) (**Fig. S1A**), we obtained chromatin accessibility profiles for a total of 10,956,311 single cells, including 6,839,086 DAPI singlets and 4,117,225 cells gated on EdU positivity (**Fig. 1B and Fig. S1B**). The median number of cells recovered per tissue range from 115,060 in the esophagus to 1,173,739 in the kidney (**Fig. 1B**). With a low sequencing duplication rate of only 20.1%, we detected a median of 3,031 unique ATAC-seq fragments per nucleus. On average, 29.8% of reads mapped to promoter regions (within ±1 kb of the transcription start site, TSS), aligning with performances from previous single-cell ATAC-seq studies (*11*, *15*) (**Fig. S1C and S1D**). Also, the pseudo bulk ATAC-seq profiles are clustered by tissue type rather than by individual mice, indicating the low technical batch effect across individuals (**Fig. S1E**).

Next, we identified and annotated heterogeneous cell types within each tissue. Applying *SnapATAC2(17)*, we performed dimensionality reduction and Leiden clustering, and manually curated the annotation based on the gene accessibility of known markers (**Table S2, Fig. S2**). Of note, we utilized the full dataset containing 10,956,311 cells for clustering and annotations. Chromatin accessibility alone enabled the identification of diverse cell types, including tissues that are challenging to profile by scRNA-seq due to high RNase levels, such as ductal cells (marked by *Ccn2*), beta-cells (marked by *Gcg*), alpha-cells (marked by *Isn1*) and delta-cells (marked by *Sst*) in the pancreas (*18*, *19*) (**Fig. S2A)**. In total, we annotated 536 organ-level main cell types, which were consolidated into 144 unique categories, with a median of 25 cell types per tissue and 4,860 nuclei per cell type (**Fig. 1C**). While most cell types were restricted to one organ (n = 102), we identified eighteen broadly distributed cell types shared by more than ten tissues, including immune cells (*e.g.,* T cells, B cells), stromal cells (*e.g.,* fibroblasts, smooth muscle cells) and endothelial cells (*e.g.,* vascular and lymphatic endothelial cells).

To globally characterize the cell-type-specific chromatin accessibility landscape, we combined reads from cells of the same type and same tissue, performed peak calling, and iteratively merged the resulting peaks to a universal set of 1,341,077 open chromatin regions (±250 base pairs from peak summit; **Methods**). The genomic distribution of these peaks was largely consistent with previous sn-ATAC-seq profiling (*14*) (**Fig. S3A**): they predominantly located within introns (n=648,244; 48.3%) and intergenic regions (n=404,499; 30.1%), and to a lesser extent at TSS-promoter regions (n=34,487; 2.57%). These regions occupy 12.3% of the genome and intersect with 89.1% of the 339,815 CREs identified by the ENCODE consortium (*20*) (**Fig. S3B**). Using this universal peak set, cells of the same lineage clustered together across tissues, such as immune cells (*e.g.,* T/NK cells, B cells, plasma cells, macrophages) and stromal cells (*e.g.,* adipocytes, pericytes), further validating the accuracy of cell annotations (**Fig. S3C**).

Using an entropy-based method(*12*), we identified 320,304 cis-regulatory elements (CREs) that are cell-type-specific (**Fig. S3D, Table S3; Methods**). We next applied chromVar (*21*) to pinpoint TF motifs specific to each cell type (**Fig. S3E**). The results were consistent with established findings, highlighting the enrichment of *Runx3* in cytotoxic T cells and NK cells (*22*), *Sfpi1* in general myeloid cells (*23*), *Irf4* in plasma cells (*24*), and *Ebf1* in B cells and pericytes (*25*, *26*) (**Fig. S3E**). The enrichment of these motifs was further validated by gene activity and cross-validated across different organs (**Fig. S3F**). Interestingly, we also observed TFs with a negative correlation between motif accessibility and gene activity, such as *Gfi1b* in erythroid cells (**Fig. S3F**), consistent with its role as a transcription repressor during erythroid development in humans(*11*, *27*).

Next, we sought to use cell-type-specific accessible peaks to interpret genetic variants associated with complex traits and diseases. Specifically, we first mapped human SNPs to orthologous coordinates in the mouse genome and then applied linkage disequilibrium score regression (LDSC) to assess GWAS SNP enrichment within cell-type-specific accessible peaks, similar to previous studies(*28*) (**Methods**). Given that many GWAS SNPs reside in non-coding regions, this analysis provides insights into their functional relevance by prioritizing cell types of interest (**Fig. S3G**). For instance, Alzheimer's disease SNPs were significantly enriched in microglia-specific CREs, consistent with prior studies(*29*). Meanwhile, SNPs associated with multiple sclerosis were enriched in B cells, T cells, and plasma cells(*30*, *31*), while LDL-associated SNPs were linked to hepatocytes(*32*) and height-associated SNPs were linked to tenocytes. SNPs for type II diabetes showed the strongest association with pancreatic beta cells(*33*), and those for hypertension with juxtaglomerular cells in the kidney(*34*) (**Fig. S3G**).

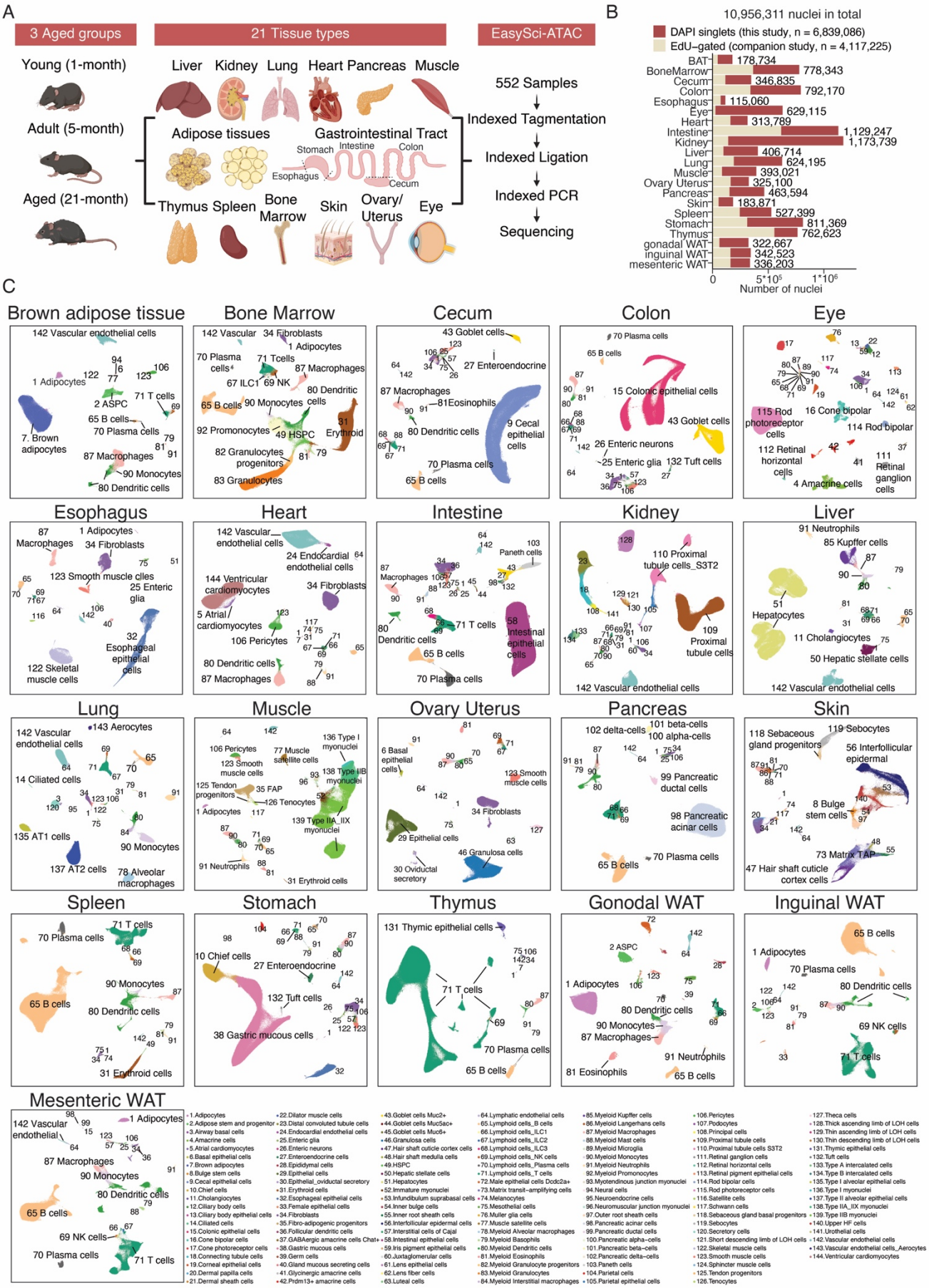
A
3 Aged groups
21 Tissue types
EasySci-ATAC
Young (1-month)
Adult (5-month)
Aged (21-month)
Liver
Kidney
Lung
Heart
Pancreas
Muscle
Adipose tissues
Gastrointestinal Tract
Stomach
Intestine
Colon
Esophagus
Cecum
Thymus
Spleen
Bone Marrow
Skin
Ovary/ Uterus
Eye
552 Samples
Indexed Tagmentation
Indexed Ligation
Indexed PCR
Sequencing
B
10,956,311 nuclei in total
DAPI singlets (this study, n = 6,839,086)
EdU-gated (companion study, n = 4,117,225)
BAT 178,734
BoneMarrow 778,343
Cecum 346,835
Colon 792,170
Esophagus 115,060
Eye 629,115
Heart 313,789
Intestine 1,129,247
Kidney 1,173,739
Liver 406,714
Lung 624,195
Muscle 393,021
Ovary Uterus 325,100
Pancreas 463,594
Skin 183,871
Spleen 527,399
Stomach 811,369
Thymus 762,623
gonadal WAT 322,667
inguinal WAT 342,523
mesenteric WAT 336,203
0
5*10^5
1*10^6
Number of nuclei
C
Brown adipose tissue
Bone Marrow
Cecum
Colon
Eye
Esophagus
Heart
Intestine
Kidney
Liver
Lung
Muscle
Ovary Uterus
Pancreas
Skin
Spleen
Stomach
Thymus
Gonodal WAT
Inguinal WAT
Mesenteric WAT

52 **Figure 1. An organismal, single-cell chromatin accessibility atlas of aging.**

53 **(A)** Experimental scheme to construct an organismal cell atlas of chromatin accessibility across different
54 ages and both sexes.
55 **(B)** Barplot showing the number of cells profiled in each tissue, colored by the sources. DAPI singlets
56 represent the global cell population investigated in this study.
57 **(C)** UMAP visualization of cells from each tissue, colored by 144 unique cell types collapsed from all
58 tissues.

Age- and sex- dependent cell population change at the main cluster level

By quantifying cell type abundances in tissues from 5-month-old mice, we observed significant variability across organs, with both highly abundant populations (*e.g.,* hepatocytes, cecal epithelial cells, brown adipocytes) and rare, organ-specific cell types detected (**Fig. 2A**). Notably, 43 organ-specific cell types constituted less than 1% of their tissue's cellular composition, such as *Ascl1*+ neuroendocrine cells in the lung (0.039%) and *Gja8*+ lens epithelial cells in the eye (0.051%), underscoring the high sensitivity of scATAC-seq to identify low abundant but critical cell populations.

We next examined sex dimorphism for each main cell type. While most cell types exhibited similar population sizes between sexes (Pearson correlation r = 0.99, 0.98, 0.95 for young, adult and aged mice, respectively) (**Fig. S4A**), we identified a subset of cell types displaying strong sex-specific differences in chromatin states. Specifically, we trained k-nearest neighbor (KNN) classifiers to distinguish female and male cells of the same age for each cell type based on chromatin embeddings (**Methods**). We then used the area under the curve (AUC) metric to quantify classification accuracy, and cell types with AUC > 0.9 were considered to exhibit high sex-associated disparity (**Fig. 2B**). This approach revealed high sex-associated chromatin states in hepatocytes, proximal tubule cells, type IIB myonuclei, and multiple cell types from the gonadal white adipose tissue (*e.g.,* adipocytes, adipose stem and progenitor cells, mesothelial cells, and smooth muscle cells)(**Fig. 2B**), mirroring previous reports based on gene expressions (*7*, *35*, *36*). For example, proximal tubule (PT) cells in the kidney, including the general states spanning spatially connected segments (PTS1, PTS2 and PTS3; marked by *Slc34a1*) and a distinct state of segment 3 (PTS3T2, marked by *Slc22a7*) (*37*) was separated into clusters determined by sexes with unique marker gene accessibility (**Fig. 2C and Fig. S4B**). Furthermore, extensive changes underlying the sex difference were found on autosomal chromosomes and exhibited high cell-type-specificity (**Fig. 2C, right**).

We further investigated how aging influences the cell population dynamics across various tissues. Using linear regression, which included an age-sex interaction term, we pinpointed specific cell types that undergo significant changes with age within each organ (**Methods**). This analysis revealed that 146 organ-specific cell types are significantly altered upon aging (FDR of 0.05, $R^2 > 0.4$), with 55 of these showing significant differences between males and females in aging (**Fig. 2D-E; Table S4**). Although aging-associated changes were noted in all profiled tissues, certain organs (*e.g.,* ovary/uterus, liver, thymus) exhibited a higher proportion of cell types with significant age-related changes (**Fig. S5A**), suggesting higher susceptibility to the aging effects in these organs.

A total of 62 main cell types were significantly expanded in aging regardless of sex (**Fig. 2E, Fig. S5B top**). Notably, the majority (68%) of these aging-expanded cell types are immune cells distributed across various organs (**Fig. S5C**). Plasma cells and macrophages were among the most significantly expanded, showing an increased relative proportion in 14 and 12 tissues, respectively, indicating a widespread increase across the organism (**Fig. 2E**). Several less characterized cell population changes were detected across multiple organs, such as the expansion of dendritic cells in the BAT and stomach, and ILC3s in the liver, colon, and cecum (**Fig. S5D**). Additionally, we observed the expansion of other immune cell types with more tissue-specific distributions, such as Kupffer cells in the liver and gamma-delta (γδ) T cells in the iWAT (**Fig. S5D**), consistent with previous studies(*38–42*). In addition to immune cells, we detected a notable expansion of various non-immune cell types during aging. For example, specialized myonuclei associated with neuromuscular junctions (NMJs) and myotendinous junctions showed increased abundance (**Fig. 2E and 2F left**), potentially acting as a compensatory mechanism to maintain muscle integrity and contractile function under age-related stress(*43*). Furthermore, we observed a rise in enteroendocrine cells within the

stomach (**Fig. 2E and 2F left)**, which could contribute to dysregulated digestive processes in aged individuals (*44*). Notably, these expansions were consistent across different sexes and were further validated by re-analysis of an independent single-cell transcriptome atlas of aging(*7*) (**Fig. 2F, right).**

The 29 aging-depleted cell types are predominantly tissue-specific (**Fig. 2E, Fig. S5B bottom**). This includes a notable reduction in immune cell progenitors such as pro-/pre-B cells in the bone marrow, which contributes to the age-related decline in immune function (*45*). Similarly, in the thymus, there is a decrease in immature T cells during the double-negative (DN) and double-positive (DP3) stages, indicative of diminished T cell production in the aging thymus (*46*). Other aging-depleted immune cell types, like NK cells and pDC cells in the spleen, were also detected, aligning with previous findings (*47*, *48*) (**Fig. 2E, Fig. S5B, S5E**). Meanwhile, multiple non-immune cell types are significantly depleted across organs, especially in the ovary/uterus, skin, and lung (**Fig. S6A**). In the ovary/uterus, for example, granulosa cells and theca cells that collaborate in sex hormones production decline with age, together with basal epithelial cells and vascular endothelial cells. (**Fig. 2E, Fig. S6B**). This aligns with the decrease in ovarian follicles that characterizes reproductive aging (*49*, *50*). In the skin, aging is associated with fewer melanocytes—a trend consistent with a 10–20% reduction per decade in individuals over 25–30 years of age (*51*)—as well as lower proportions of dermal papilla cells, outer root sheath cells, and lymphatic endothelial cells (**Fig. 2E, Fig. S6B**), the latter consistent with reduced skin lymphatic density observed in aging(*52*). Similarly, the aged lung exhibits declines in stromal cell types associated with blood vessels, including pericytes, smooth muscle cells (**Fig. 2E, Fig. S6B**), and a specialized endothelial cell type known as aerocytes(*53*) (**Fig. 2F**). These cells are important for maintaining proper vascular structure and function, suggesting that their depletion may contribute to compromised blood flow regulation in the elderly lung(*54*).

Moreover, we observed a decline in other functional cell types, such as kidney podocytes that filter primary urine from plasma (**Fig. 2E-F)**, aligning with previous studies(*55*). The depleted cell populations also include a group of less characterized *Ncam1*+ parietal epithelial cells (**Fig. 2E, Fig. S6B)**, which serve as progenitor cells capable of proliferation and differentiation into podocytes (*56*). The depletion of both mature podocytes and their precursor cells could contribute to the impaired capacity of the kidney to regenerate and maintain proper filtration over time. Additionally, aging-depleted cell types include liver hepatocytes (*57*), muscle tenocytes(*58*), muscle satellite cells (*59*), stomach enteric neurons, and adipocytes from multiple organs (*e.g.,* lung, gWAT, and ovary/uterus) (**Fig. 2E-F and S5B),** validated by re-analysis of external single-cell transcriptome dataset(*7*) (**Fig. 2F)**. Interestingly, some of these aging-decreased cell types (*e.g.,* muscle satellite cells and tenocytes, bone marrow pro-/pre-B cells) exhibited reductions of more than 50% at relatively early stages (between 1 and 5 months) (**Fig. 2F, S5B bottom, S6B**), highlighting an early onset of aging impacts on the population of these cell types.

We further analyzed 55 cell types displaying significant age-sex interactions. Most sex-specific cell types (35 out of 55) are immune cells, including 19 that preferentially expanded in aging females and 15 in aging males (**Fig. 2G)**. For instance, aged male mice showed significant increases in neutrophils (in the lung and intestine) and eosinophils in the muscle (**Fig. 2G)**, consistent with male-specific expansions of these cells observed in prior human studies(*60*, *61*). Conversely, aged females demonstrated increased populations of basophils (in the liver) and NK cells (in the pancreas and bone marrow) (**Fig. 2G)**. Additionally, some cell types exhibited similar trends in both sexes but differed in the extent of change in different organs. For example, ILC2 cells in the bone marrow and hepatic stellate cells in the liver expanded more significantly in males, whereas the increase of interstitial macrophages in the lung and depletion of naive/memory B cells in the spleen was more pronounced in the female (**Fig. 2G-H)**. Interestingly, certain cell types showed opposite trends between the sexes. For instance, the aforementioned specialized proximal tubule (PT) cell

248 type (PT S3T2, characterized by *Slc22a7*) increased in females but decreased in males, whereas the other
249 PT cells (PT S1S2S3, marked by *Slc34a1*) exhibited the opposite pattern (**Fig. 2I)**. The findings were
250 further validated by re-analysis of independent single-cell transcriptome atlas profiling both adult and aged
251 tissues (*7*) (**Fig. 2J).**

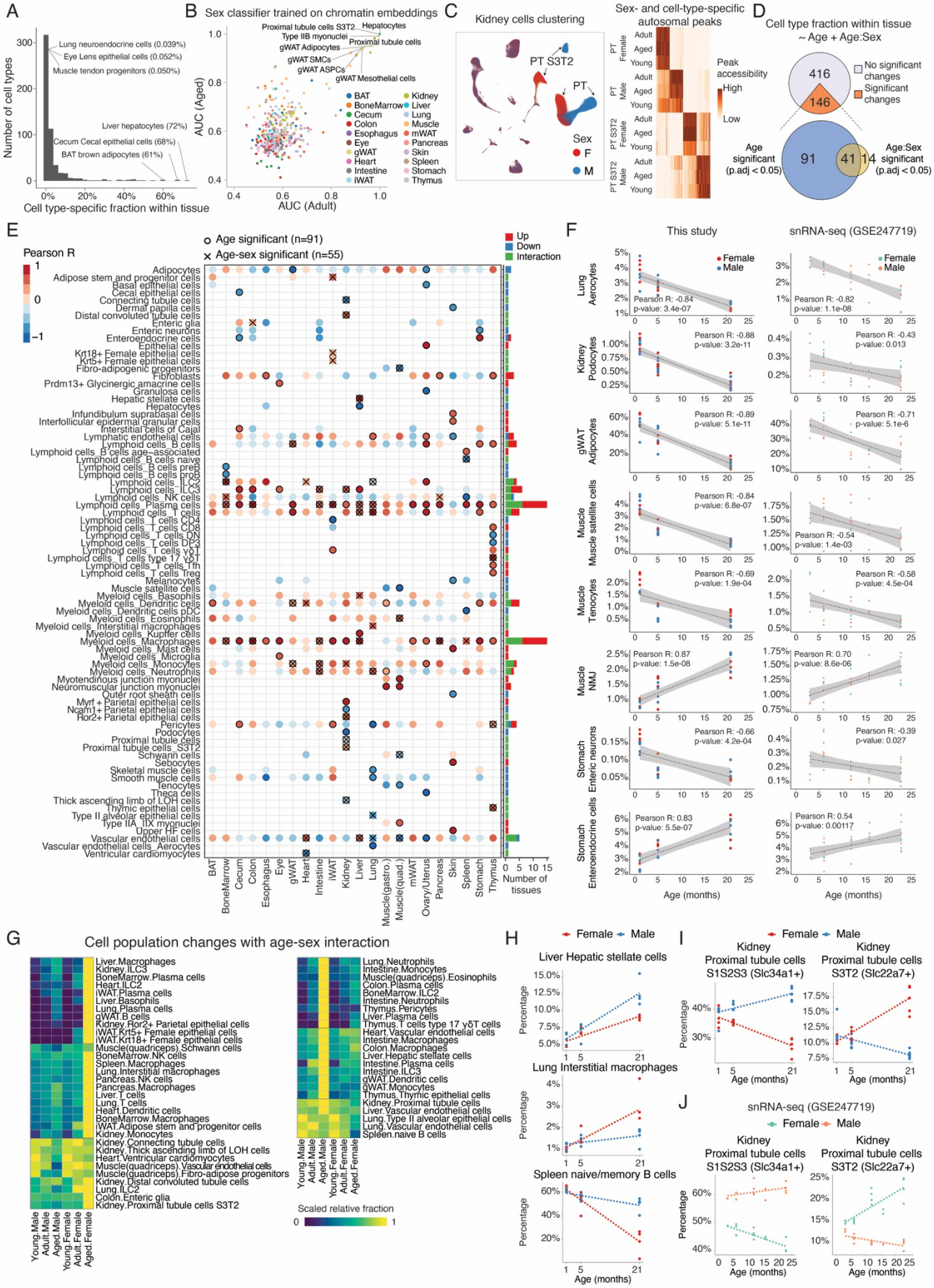
A
Number of cell types
Lung neuroendocrine cells (0.039%)
Eye Lens epithelial cells (0.052%)
Muscle tendon progenitors (0.050%)
Liver hepatocytes (72%)
Cecum Cecal epithelial cells (68%)
BAT brown adipocytes (61%)
Cell type-specific fraction within tissue
B
Sex classifier trained on chromatin embeddings
AUC (Aged)
AUC (Adult)
Proximal tubule cells S3T2
Hepatocytes
Type IIB myonuclei
Proximal tubule cells
gWAT Adipocytes
gWAT SMCs
gWAT ASPCs
gWAT Mesothelial cells
BAT
BoneMarrow
Cecum
Colon
Esophagus
Eye
gWAT
Heart
Intestine
iWAT
Kidney
Liver
Lung
Muscle
mWAT
Pancreas
Skin
Spleen
Stomach
Thymus
C
Kidney cells clustering
PT S3T2
PT
Sex
F
M
Sex- and cell-type-specific autosomal peaks
PT Female
PT Male
PT S3T2 Female
PT S3T2 Male
Adult
Aged
Young
Peak accessibility
High
Low
D
Cell type fraction within tissue
~ Age + Age:Sex
416
146
No significant changes
Significant changes
Age significant (p.adj < 0.05)
91
41
14
Age:Sex significant (p.adj < 0.05)
E
Pearson R
Age significant (n=91)
Age-sex significant (n=55)
Up
Down
Interaction
Adipocytes
Adipose stem and progenitor cells
Basal epithelial cells
Cecal epithelial cells
Connecting tubule cells
Dermal papilla cells
Distal convoluted tubule cells
Enteric glia
Enteric neurons
Enteroendocrine cells
Epithelial cells
Krt18+ Female epithelial cells
Krt5+ Female epithelial cells
Fibro-adipogenic progenitors
Fibroblasts
Prdm13+ Glycinergic amacrine cells
Granulosa cells
Hepatic stellate cells
Hepatocytes
Infundibulum suprabasal cells
Interfollicular epidermal granular cells
Interstitial cells of Cajal
Lymphatic endothelial cells
Lymphoid cells_B cells
Lymphoid cells_B cells age-associated
Lymphoid cells_B cells naive
Lymphoid cells_B cells preB
Lymphoid cells_B cells proB
Lymphoid cells_ILC2
Lymphoid cells_ILC3
Lymphoid cells_NK cells
Lymphoid cells_Plasma cells
Lymphoid cells_T cells
Lymphoid cells_T cells CD4
Lymphoid cells_T cells CD8
Lymphoid cells_T cells DN
Lymphoid cells_T cells DP3
Lymphoid cells_T cells γδT
Lymphoid cells_T cells type 17 γδT
Lymphoid cells_T cells Tfh
Lymphoid cells_T cells Treg
Melanocytes
Muscle satellite cells
Myeloid cells_Basophils
Myeloid cells_Dendritic cells
Myeloid cells_Dendritic cells pDC
Myeloid cells_Eosinophils
Myeloid cells_Interstitial macrophages
Myeloid cells_Kupffer cells
Myeloid cells_Macrophages
Myeloid cells_Mast cells
Myeloid cells_Microglia
Myeloid cells_Monocytes
Myeloid cells_Neutrophils
Myotendinous junction myonuclei
Neuromuscular junction myonuclei
Outer root sheath cells
Myrf+ Parietal epithelial cells
Ncam1+ Parietal epithelial cells
Ror2+ Parietal epithelial cells
Pericytes
Podocytes
Proximal tubule cells
Proximal tubule cells_S3T2
Schwann cells
Sebocytes
Skeletal muscle cells
Smooth muscle cells
Tenocytes
Theca cells
Thick ascending limb of LOH cells
Thymic epithelial cells
Type II alveolar epithelial cells
Type IIA_IIX myonuclei
Upper HF cells
Vascular endothelial cells
Vascular endothelial cells_Aerocytes
Ventricular cardiomyocytes
BAT
BoneMarrow
Cecum
Colon
Esophagus
Eye
gWAT
Heart
Intestine
iWAT
Kidney
Liver
Lung
Muscle(gastro.)
Muscle(quad.)
mWAT
Ovary/Uterus
Pancreas
Skin
Spleen
Stomach
Thymus
Number of tissues
F
This study
snRNA-seq (GSE247719)
Female
Male
Lung Aerocytes
Pearson R: -0.84
p-value: 3.4e-07
Pearson R: -0.82
p-value: 1.1e-08
Kidney Podocytes
Pearson R: -0.88
p-value: 3.2e-11
Pearson R: -0.43
p-value: 0.013
gWAT Adipocytes
Pearson R: -0.89
p-value: 5.1e-11
Pearson R: -0.71
p-value: 5.1e-6
Muscle satellite cells
Pearson R: -0.84
p-value: 6.8e-07
Pearson R: -0.54
p-value: 1.4e-03
Muscle Tenocytes
Pearson R: -0.69
p-value: 1.9e-04
Pearson R: -0.58
p-value: 4.5e-04
Muscle NMJ
Pearson R: 0.87
p-value: 1.5e-08
Pearson R: 0.70
p-value: 8.6e-06
Stomach Enteric neurons
Pearson R: -0.66
p-value: 4.2e-04
Pearson R: -0.39
p-value: 0.027
Stomach Enteroendocrine cells
Pearson R: 0.83
p-value: 5.5e-07
Pearson R: 0.54
p-value: 0.00117
Age (months)
G
Cell population changes with age-sex interaction
Liver.Macrophages
Kidney.ILC3
BoneMarrow.Plasma cells
Heart.ILC2
iWAT.Plasma cells
Liver.Basophils
Lung.Plasma cells
gWAT.B cells
Kidney.Ror2+ Parietal epithelial cells
iWAT.Krt5+ Female epithelial cells
iWAT.Krt18+ Female epithelial cells
Muscle(quadriceps).Schwann cells
BoneMarrow.NK cells
Spleen.Macrophages
Lung.Interstitial macrophages
Pancreas.NK cells
Pancreas.Macrophages
Liver.T cells
Lung.T cells
Heart.Dendritic cells
BoneMarrow.Macrophages
iWAT.Adipose stem and progenitor cells
Kidney.Monocytes
Kidney.Connecting tubule cells
Kidney.Thick ascending limb of LOH cells
Heart.Ventricular cardiomyocytes
Muscle(quadriceps).Vascular endothelial cells
Muscle(quadriceps).Fibro-adipose progenitors
Kidney.Distal convoluted tubule cells
Lung.ILC2
Colon.Enteric glia
Kidney.Proximal tubule cells S3T2
Lung.Neutrophils
Intestine.Monocytes
Muscle(quadriceps).Eosinophils
Colon.Plasma cells
BoneMarrow.ILC2
Intestine.Neutrophils
Thymus.Pericytes
Liver.Plasma cells
Thymus.T cells type 17 γδT cells
Heart.Vascular endothelial cells
Intestine.Macrophages
Colon.Macrophages
Liver.Hepatic stellate cells
Intestine.Plasma cells
Intestine.ILC3
gWAT.Dendritic cells
gWAT.Monocytes
Thymus.Thymic epithelial cells
Kidney.Proximal tubule cells
Liver.Vascular endothelial cells
Lung.Type II alveolar epithelial cells
Lung.Vascular endothelial cells
Spleen.naive B cells
Young.Male
Adult.Male
Aged.Male
Young.Female
Adult.Female
Aged.Female
Scaled relative fraction
0
1
H
Female
Male
Liver Hepatic stellate cells
Lung Interstitial macrophages
Spleen naive/memory B cells
Percentage
Age (months)
I
Kidney Proximal tubule cells S1S2S3 (Slc34a1+)
Kidney Proximal tubule cells S3T2 (Slc22a7+)
J
snRNA-seq (GSE247719)

Figure 2. Age- and sex-dependent cell population changes at the main cell type level.

(A) Histogram showing the distribution of cell type specific fractions within tissue. Only cells from adult mice (5-month-old) were used in this quantification.

(B) K-means classifiers were trained to distinguish male and female cells for each main cell type using spectral embedding calculated by SnapATAC2 (*17*). Scatterplot comparing the area under the curve (AUC) values of models between adult and aged cells. Cell types with high sex dimorphism in both age groups are labeled.

(C) Left: UMAP plots of all kidney cells, colored by sex (right), highlighting distinct chromatin states between sexes of proximal tubule cells (PT). Right: Heatmap displaying accessibility of autosomal peaks with sex- and cell-type-specific patterns, conserved across ages.

(D) Venn diagram showing the number of main cell types whose relative proportions in corresponding tissues are significantly associated with age or age-sex interactions.

(E) Left: Dotplot showing all significantly altered main cell types from (D) across tissues, colored by Pearson correlation between their relative proportion and age. Cell types with significant age or age-sex interactions are marked. Right: Barplot summarizing the number of tissues with significant changes for each cell type, colored by direction (up/down) or interaction.

(F) Scatterplot illustrating examples of main cell types with significant age-related proportional changes (left), alongside validation using published snRNA-seq data (*7*) for the same cell type and tissue (right).

(G) Heatmap showing relative proportions of main cell types with significant age-sex interactions, including female-biased (left) and male-biased (right) cell types.

(H) Scatterplot highlighting cell types that change in the same direction with aging but exhibit sex-dependent magnitude.

(I-J) Scatterplots of two kidney proximal tubule cell types with opposite sex-specific proportional trends **(I)** and snRNA-seq validation results **(J).**

Age- and sex- dependent cell population change at the subtype level

We further explored cell population dynamics at the subtype level. First, we re-clustered each main cell type using *SnapATAC2(17)*, and manually curated cellular subtypes based on cluster-specific gene accessibility. Our analysis revealed significant heterogeneity within main cell types. For instance, amacrine cells in the eye, known for their extensive diversity(*62*), were clustered into thirty-four distinct subtypes (**Fig. 3A**). These subtypes were characterized by unique gene activity, peak accessibility, and TF motif enrichments (**Fig. 3A, Fig. S7A-B**), aligning with previous findings based on single-cell transcriptomic analyses (*62*). In total, our clustering analysis identified 1,828 subtypes from 386 main cell types across the entire organism, with a median of 1,610 cells per subtype and four subtypes per main cell type (**Fig. S7C**). Most subtypes (93.4%) were consistently detected across more than ten samples (**Fig. S7C**). Notably, we identified many rare cell subtypes that have not been extensively explored in prior chromatin accessibility studies. Notable examples include diverse enteroendocrine cells in the small intestine, including L cells (marked by *Gcg*, 0.092% of the total population), K cells (marked by *Gip*, 0.070%), D cells (marked by *Sst*, 0.028%), enterochromaffin cells (marked by *Tph1*, 0.084%), and enteroendocrine progenitor cells (marked by *Neurog3*, 0.081%) (**Fig. S7D-S7E**).

We next investigated cell population changes at the subtype level. Using the same analytical pipeline for identifying aging-associated main cell types, we identified 499 subtypes (out of 228 organ-specific main cell types) with significant cell population dynamics associated with aging (FDR of 0.05, $R^2 > 0.4$) (**Fig. 3B, Table S5**). Of these, 193 subtypes exhibited significant sex-specific aging differences (FDR of 0.05) (**Fig. 3C**). A median of 24 significantly altered subtypes was identified per tissue, ranging from 51 in the kidney to 3 in the esophagus (**Fig. 3C**). While the dynamics of aging-associated subtypes were generally consistent with their main cell type changes (Pearson r: 0.72, p-value $< 2.2 * 10^{-26}$), distinct trends emerged in certain subtypes compared to their parent main cell types (**Fig. 3D**). For instance, specific aging-associated subtypes such as *Lepr1+ Abcg1+* fibroblasts and *Ccr3+ C5ar1+ C5ar2+* mast cells expanded in the aged intestine, while their main cell types remained relatively stable with age (**Fig. S7F-G**). In the liver and lung, while the overall main T cell population increased in aged tissues, subtypes corresponding to naive T cells were depleted (**Fig. S7F-G**). In contrast, we observed an expansion of a subtype corresponding to *Il10+ Foxp3+* regulatory T cell in the iWAT, despite the overall CD4 T cell proportion decreasing with aging (**Fig. S7F-G**). We also observed opposing aging-associated dynamics of subtypes from the same cell type. For example, in the bone marrow hematopoietic stem and progenitor cells (HSPCs), there is a marked decrease in lymphoid progenitors (HSPC-3, marked by *Il7r (63)*), accompanied by a significant expansion of aging-associated megakaryocyte progenitors (HSPC-4, marked by *Gata2, Fhl1, and Hoxb5*) (**Fig. 3E-F)**, consistent with findings from a recent study(*64*).

Several aging-associated subtypes correspond to the same cell type in distinct spatial locations, uncovering region-specific vulnerabilities during aging. For example, renal vascular endothelial cells (ECs) can be clustered into heterogeneous subtypes representing ECs from different anatomical locations within the nephron(*65*), including the artery (*Sox6+*), cortex (*Npr3+, Igfbp3+*), vein (*Lhx6+*), medulla (*Igf1+, Cyp1b1+*), vasa recta (*Aqp1+*), and glomeruli (*Gata5+*) (**Fig. 3G-H**). Interestingly, while the total abundance of ECs remains relatively unchanged at the main cell type level, we observed a pronounced depletion of two EC subtypes—*Lhx6+* vein ECs and *Igf1+, Cyp1b1+* medulla ECs (**Fig. 3I**)—indicating that endothelial cells in these specific regions are more vulnerable to aging. The findings were further validated through a published snRNA-seq dataset(*7*): we observed a consistent decline of *Igf1+ Cyp1b1+* medulla ECs across aging in both sexes, despite a higher baseline proportion in females (**Fig. 3J-K)**.

Meanwhile, certain aging-associated cell subtypes across different spatial locations share similar molecular features. For example, sub-clustering analysis of three specialized renal epithelial cell types—the thick ascending limb of the Loop of Henle (TAL), distal convoluted tubule (DCT), and connecting tubule (CNT)—revealed three subtypes (*i.e.,* TAL-5, DCT-4, and CNT-5) that exhibit significant expansion in aging (**Fig. 3L-M)**, particularly in females. All three subtypes converged into a reactive aging-associated epithelial cell state that is characterized by the activation of transcription factors linked to inflammation and stress responses (*e.g., Creb5, Bnc2, Runx1, Bach2, Fosl2,* and *Klf7***)**, confirmed through gene body accessibility (**Fig. 3N**) and TF motif activity (**Fig. 3O)**. We further validated the existence of these states (**Fig. 3P**) and female-biased expansions (**Fig. 3Q**) by re-clustering the same cell type from a single-cell transcriptomic atlas of aging(*7*). The emergence of this reactive cellular state underscores the potential influence of inflammatory signaling on epithelial cells specifically in the aged female kidney. In summary, our subtype-level analysis revealed both region-specific and shared aging-associated changes.

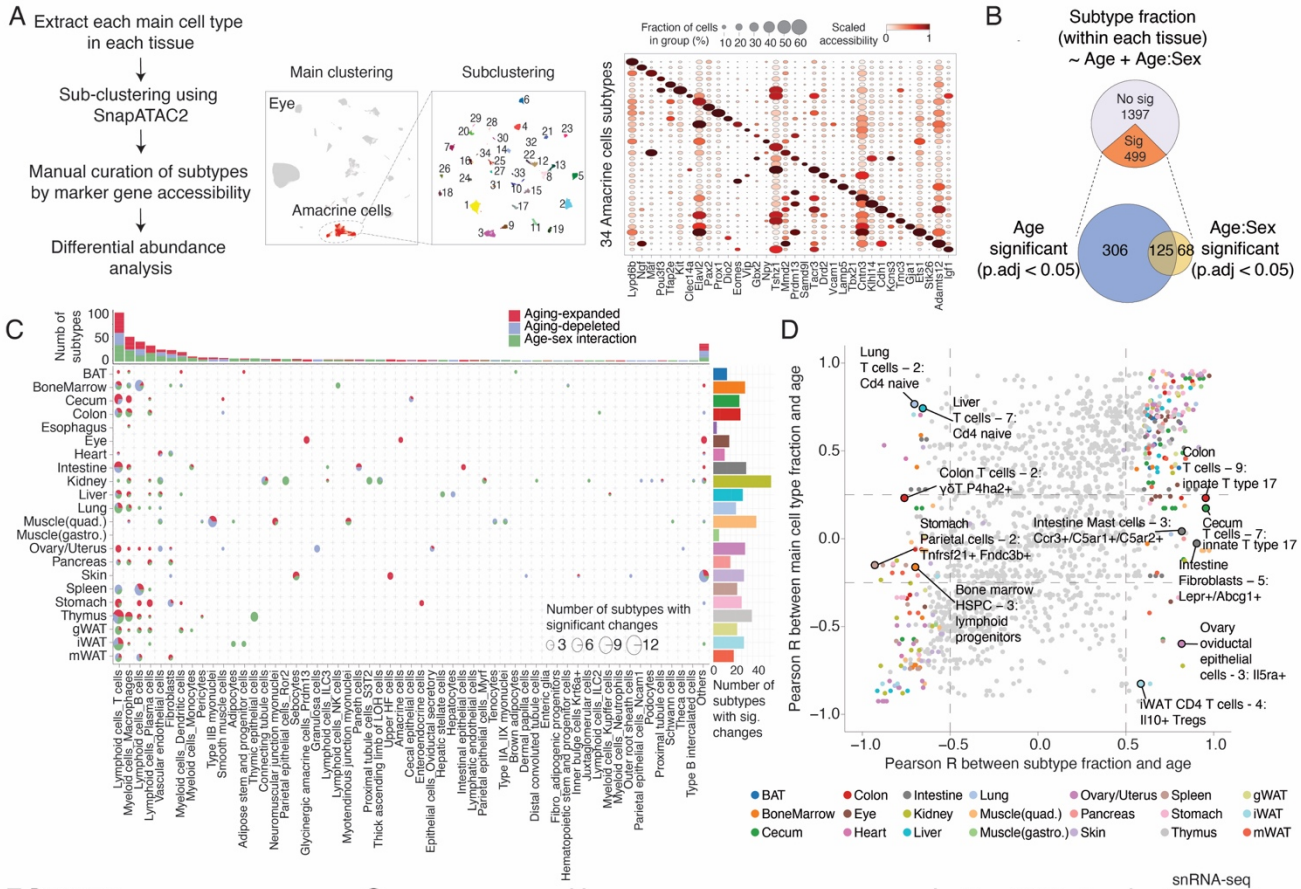
A
Extract each main cell type in each tissue
Sub-clustering using SnapATAC2
Manual curation of subtypes by marker gene accessibility
Differential abundance analysis
Main clustering
Subclustering
Eye
Amacrine cells
Fraction of cells in group (%)
Scaled accessibility
34 Amacrine cells subtypes
B
Subtype fraction (within each tissue) ~ Age + Age:Sex
No sig 1397
Sig 499
Age significant (p.adj < 0.05)
306
125
68
Age:Sex significant (p.adj < 0.05)
C
Numb of subtypes
Aging-expanded
Aging-depeleted
Age-sex interaction
Number of subtypes with significant changes
Number of subtypes with sig. changes
D
Pearson R between main cell type fraction and age
Pearson R between subtype fraction and age
Lung T cells – 2: Cd4 naive
Liver T cells – 7: Cd4 naive
Colon T cells – 2: γδT P4ha2+
Colon T cells – 9: innate T type 17
Stomach Parietal cells – 2: Tnfrsf21+ Fndc3b+
Intestine Mast cells – 3: Ccr3+/C5ar1+/C5ar2+
Cecum T cells – 7: innate T type 17
Intestine Fibroblasts – 5: Lepr+/Abcg1+
Bone marrow HSPC – 3: lymphoid progenitors
Ovary oviductal epithelial cells - 3: Il5ra+
iWAT CD4 T cells - 4: Il10+ Tregs
BAT
BoneMarrow
Cecum
Colon
Eye
Heart
Intestine
Kidney
Liver
Lung
Muscle(quad.)
Muscle(gastro.)
Ovary/Uterus
Pancreas
Skin
Spleen
Stomach
Thymus
gWAT
iWAT
mWAT
E
Bone marrow main clustering
HSPC subclustering
Young
Adult
Aged
Il7r
Gata2
Fhl1
Gene activity
High
Low
F
HSPC - 3 Lymphoid progenitors
HSPC - 4 Aging associated MkPs
Sex
Female
Male
Age (months)
G
Kidney main clustering
Flt1
Vascular endothelial cells
VEC subclustering
H
Sox6
Artery
Npr3
Cortex
Igfbp3
Cortex
Lhx6
Lhx6+ ECs
Igf1
Medulla
Cyp1b1
Medulla
Gata5
Glomeruli
Aqp1
Vasa recta
Kit
Kit+ ECs
Gene activity High Low
I
Kidney VEC All cells
Percentage
VEC - 4: Lhx6+
VEC - 5: Igf1+ Cyp1b1+
J
snRNA-seq (GSE247719) Kidney VEC
Igf1
Cyp1b1
Gene exprs
K
Igf1+ Cyp1b1+ VECs
L
Slc12a1
Thick ascending limb of LOH cells
TAL
Slc12a3
Distal convoluted tubule cells
DCT
Calb1
Connecting tubule cells
CNT
M
TAL - 5
DCT - 4
CNT - 5
N
Kidney TAL
Kidney DCT
Kidney CNT
Gene accessibility
Subcluster id
O
Motif activity
chromVar deviations
P
snRNA-seq (GSE247719)
Thick ascending limb of LOH cells
Creb5
Runx1
Distal convoluted tubule cells
Samd5
Connecting tubule cells
Dcdc2a
Gene expression
Q
Creb5+ TAL
Creb5+ DCT
Creb5+ CTL

Figure 3 Age- and sex-dependent cell population change at the subtype level.

(A) Left: schematic of the sub-clustering workflow. Middle: example UMAP plots showing sub-clustering analysis of eye amacrine cells, colored by subcluster ID. Right: dotplot displaying marker gene accessibility for amacrine cell subtypes.

(B) Venn diagram showing the number of cell subtypes with significant changes associated with age or age-sex interactions.

(C) Top: barplot showing the number of aging-associated subtypes for each main cell type. Center: dotplot summarizing the number aging-associated subtypes across main cell types and tissues. Right: barplot showing the number of aging-associated subtypes per tissue.

(D) Scatterplot comparing aging-associated cellular fraction changes between aging-associated subtypes and their corresponding main cell types. Subtypes with distinct trends compared to their parent main cell types are labeled.

(E) UMAP plots showing sub-clustering of bone marrow HSPCs to identify different subtypes, colored by subcluster ID (top middle), age group (top right), and marker gene accessibilities for lymphoid progenitor cells (bottom left) and age-associated megakaryocyte progenitors (bottom right).

(F) Scatter plot showing cell proportion changes for lymphoid progenitor cells (HSPC-3) and age-associated megakaryocyte progenitors (HSPC-4), with a linear regression fit. Each dot represents one animal.

(G) UMAP plot showing sub-clustering results of kidney vascular endothelial cells to identify different subtypes, colored by subcluster ID (bottom).

(H) UMAP plots of kidney vascular endothelial cells, colored by the accessibility of genes that mark vascular cells across different spatial locations.

(I) Scatter plots and boxplots showing the fractions of all kidney endothelial cells (top), vein endothelial cells (*Lhx6*+ VEC-4, center), and medulla endothelial cells (*Igf1*+ *Cyp1b1*+ VEC-5, bottom) across three age groups.

(J) UMAP plots of vascular endothelial cells from a published snRNA-seq study (*7*), colored by the expression of genes marking medulla endothelial cells (as in **H**).

(K) Scatterplot showing the aging-associated decline in the kidney medulla endothelial cells identified from a snRNA-seq atlas of aging(*7*).

(L) UMAP plots showing all kidney cells (Left) and sub-clustering analysis (middle and right) for thick ascending limb cells (TAL, top), distal convoluted tubule cells (DCT, center), and connecting tubule cells (CNT, bottom), colored by main cell type specific markers (left), subtype ID (middle) and age group (right). Squares indicate the aging-associated cell subtypes.

(M) Scatter plots showing the relative fractions of three reactive subtypes identified in (**K**) across ages, with separate linear regression fits for each sex.

(N) Dotplots showing the gene marker accessibility marking the reactive states (TAL-5, DCT-4 and CNT-5) in each renal epithelial cell type.

(O) Violinplots showing the motif accessibilities of transcription factors marking the reactive states in each renal epithelial cell type.

(P) UMAP plots showing sub-clustering results for TAL, DCT, and CNT cells from published snRNA-seq data(*7*), colored by the expression of genes that mark reactive states (as in **N**).

(Q) Scatterplots showing the relative fractions of reactive subtypes identified in **(P)** across aging, with separate linear regression fits for each sex.

382 **Aging-associated population dynamics of broadly distributed immune subtypes**

383 We next examined whether broadly distributed cells displayed similar dynamics across multiple organs in
384 aging. We first analyzed immune cells, including T cells (n = 1,264,322 cells), B cells (n = 1,079,641 cells),
385 plasma cells (n = 157,545 cells), innate lymphoid cells (NK cells, ILC1, ILC2 and ILC3) (n = 87,550 cells),
386 monocytes and macrophages (n = 581,877 cells), and dendritic cells (n = 306,562 cells) isolated from
387 various organs.

388 Clustering analysis for each cell type revealed a total of sixty-seven highly heterogeneous immune cell
389 subtypes, each defined by distinct chromatin accessibility patterns at key marker genes (**Fig. 4A-B**). For
390 instance, the combined clustering of T cells yielded sixteen subtypes spanning a differentiation trajectory
391 from T progenitor/double-negative (DN) cells, through double-positive (DP) cells, and onward to mature T
392 cell states (**Fig. 4A-B, top left**), including CD4 T cells (*Cd4*+), CD8 T cells (*Cd8b1*+), γδ T cells (*Tcrg-C4*+),
393 and innate-like T cells (*Zbtb16*+) (**Fig. S8A**). Similarly, we identified eight B cell clusters forming a trajectory
394 from pro-B and pre-B cells (*Erg+, Rag1+, Il7r*+) through naive/memory B cells (*Cd55+, Fcer2a*+) and finally
395 transitioned into aging-associated states marked by either *Tbx21* or *Pstpip2* (**Fig. 4A-B, top right; Fig.**
396 **S8B**). These aging-associated B cell states closely mirror recent single-cell transcriptomic findings(*66*).
397 Within the plasma cell population, we detected IgA, IgM, and IgG plasma cells, each comprising several
398 distinct subtypes (**Fig. 4A-B, middle left**). For innate lymphoid cells, ten clusters were identified, including
399 multiple subtypes within NK cells, ILC2, and ILC3 (**Fig. 4A-B, middle right; Fig. S8C**). Monocytes and
400 macrophages were resolved into twelve subtypes (**Fig. 4A-B, bottom left**), capturing the transition from
401 *Ace*+ monocytes to *Lyve1*+ tissue-resident macrophages, and various specialized macrophages across
402 different tissues. Dendritic cells (DC) were categorized into fourteen subtypes (**Fig. 4A-B, bottom right**),
403 including *Xcr1*+ type I DCs, *Sirpa*+ type II DCs, *Ccr7*+ migratory DCs, and *Siglech*+ plasmacytoid DCs,
404 with diverse subsets observed within each major type.

405 We then quantified the tissue composition of each immune subtype. Although many subtypes were
406 detected globally, certain subtypes exhibited high organ specificity (**Fig. 4C**). For example, immature T
407 cells (T cells -1, T cells - 2, T cells -3, and T cells - 4) were predominantly in the thymus, while *Gzma*+ γδ
408 T cells (T cells - 13) were mainly localized to the intestine, cecum, and colon(**Fig. 4C**). Similarly, B cell
409 progenitors (B cells - 1 and B cells - 2) were primarily found in the bone marrow, and IgA+ plasma cells
410 (plasma cells - 1, plasma cells -2, and plasma cells - 3) were enriched in gastrointestinal organs (*e.g.,*
411 intestine, cecum, and colon)(**Fig. 4C**). For macrophages (MAC), *Cxcl16*+ *Tlr12*+ macrophages (MAC-6
412 and MAC-7) were constrained to the small and large intestine, while *Spic*+ macrophages were unique to
413 bone marrow (MAC-9) and spleen (MAC-10)(**Fig. 4C**). The latter aligns with previous reports about the
414 role of *Spic* in the development of iron-recycling macrophages in these two organs(*67*). Certain dendritic
415 cells also demonstrated tissue-specific characteristics, such as *Apol7c*+ type I DCs (DC-3), *Il22ra2*+, and
416 *C1qtnf3*+ type II DCs (DC-9 and DC-10), which were exclusively identified in the gut(**Fig. 4C**).

417 We next assessed how these immune subtypes changed with aging (**Fig. 4D**). Six immune subtypes were
418 found significantly depleted across multiple tissues, including naive CD4+ T cells in ten tissues, naive
419 CD8+ T cells in five tissues, and immature B cells in the bone marrow, spleen, and mWAT(**Fig. 4D**). We
420 also observed a significant depletion of organ-specific immune progenitor cells, such as immature T cells
421 in the thymus and pro-B/pre-B cells in the bone marrow, which subsequently led to a reduction of
422 naive/memory B cells in tissues like the spleen and mWAT(**Fig. 4D**). In addition, we uncovered less-
423 characterized immune cell dynamics validated across multiple organs. For instance, *Zfp683*+ tissue-
424 resident memory T cells were consistently depleted in the intestine, iWAT, and mWAT (T cells - 12, **Fig.**
425 **4D**), and *Gzma*+ resting NK cells (*68*) were depleted in both the spleen and bone marrow (NK - 1; **Fig.**

4D). Notably, the depletion of this resting NK cell subtype occurred concurrently with an expansion of a *Gpr55*+ *Ifi211*+ proinflammatory NK cell subtype (*69*) (NK - 3) in the same organs (**Fig. 4D**).

In contrast to these depletions, the majority of immune subtypes (42 out of 67) significantly expanded during aging in at least one tissue (**Fig. 4D**). These expansions included nine T cell subtypes, eight NK and ILC subtypes, five B cell subtypes, seven dendritic cell subtypes, and nearly all plasma cell and monocytes/macrophages ('MoMa') subtypes (**Fig. 4D**). Notable examples of broadly expanding populations included *Zbtb16*+ *Il23r*+ type 17 innate T cells (T cells - 15), *Gzmk*+ CD8 T cells (T cells - 10), *Il21*+ follicular helper T cells (T cells - 9), *Foxp3*+ regulatory T cells (T cells - 7), *Tbx21*+ aging-associated B cells (B cells - 6), *Chst1*+ *Wipf3*+ IgM plasma cells (plasma cells - 5), *Clec4d*+ monocytes (MoMa - 4), and *F13a1*+ *Lyve1*+ macrophages (MoMa - 5), each of which expanded in multiple organs (**Fig. 4D**). Beyond these widespread patterns, some aging-associated expansions were confined to specific organs. For example, several immune subtypes expanded preferentially in the gastrointestinal tract, such as *Gpr15*+ *Stc2*+ IgA plasma cells (plasma cells - 3; **Fig. 4E-F, left**), *Tlr12*+ macrophages (macrophages - 7; **Fig. 4E-F, right**), *Ccr6*+ *Trappc3l*+ ILC3 cells (NK/ILC - 7), and *Apol7c*+ type I DCs (dendritic cells - 3) (**Fig. 4D**). We also identified tissue-specific expansions of *Cd163l*+ *Sox13*+ ILC3 cells (NK/ILC - 8) in the eye, kidney, and liver, as well as *Pcsk1*+ ILC2s (NK/ILC - 9) in the ovary/uterus and *Cybb*+ ILC2s (NK/ILC - 10) in the bone marrow (**Fig. 4D**). Interestingly, some immune subtypes exhibited opposite trends depending on the organ. For instance, *Klrk1*+ *Gas7*+ CD8 effector T cells (T cells - 8) expanded in the liver and lung but were depleted in gastrointestinal tissues (*e.g.,* colon and cecum) (**Fig. 4D**), potentially due to distinct local microenvironmental cues that shape tissue-specific aging dynamics.

Aging-associated immune cell dynamics also differed notably between males and females. For example, *Gzmk*+ CD8 exhausted T cells exhibited greater expansion in females (**Fig. 4G, left**), notably in the lung, pancreas, and mWAT, while type 17 innate T cells showed a stronger increase in males, especially in the stomach, gWAT, and mWAT (**Fig. 4G, right)**. Overall, however, we observed that females tend to have a greater expansion of immune cell subtypes than males during aging (53 female-biased subtypes compared to 31 male-biased subtypes, **Fig. S8D**), including *Tbx21*+ aging-associated B cells (in mWAT, pancreas, thymus; **Fig. 4H**), *Gpr55*+ *Ifi211*+ NK cells (in bone marrow, pancreas, iWAT, spleen; **Fig. 4I-J, left**), *Sox5*+ *Ifnlr1*+ *Zfp362*+ macrophages (in thymus, gWAT; **Fig. 4I-J, middle**) and *Dtx1*+ *Sripb1a*+ type II dendritic cells (**Fig. 4I-J, right**). These subtypes potentially contribute to the higher prevalence of autoimmune diseases in women(*70*). Interestingly, we observed an enrichment of male-biased subtypes within gastrointestinal tissues, with 15 out of 31 originating from the esophagus, stomach, intestine, cecum, and colon, compared to only 2 out of 53 in female-biased ones (**Fig. S8D**). Noteworthy examples include the expansion of *Ccr9*+ ILC3s (NK/ILC-5) and *Cyp26b1*+ ILC3s (NK/ILC-6) in the intestine (**Fig. S8D**), reflecting more pronounced changes in the innate immunity during male intestinal aging (*71*).

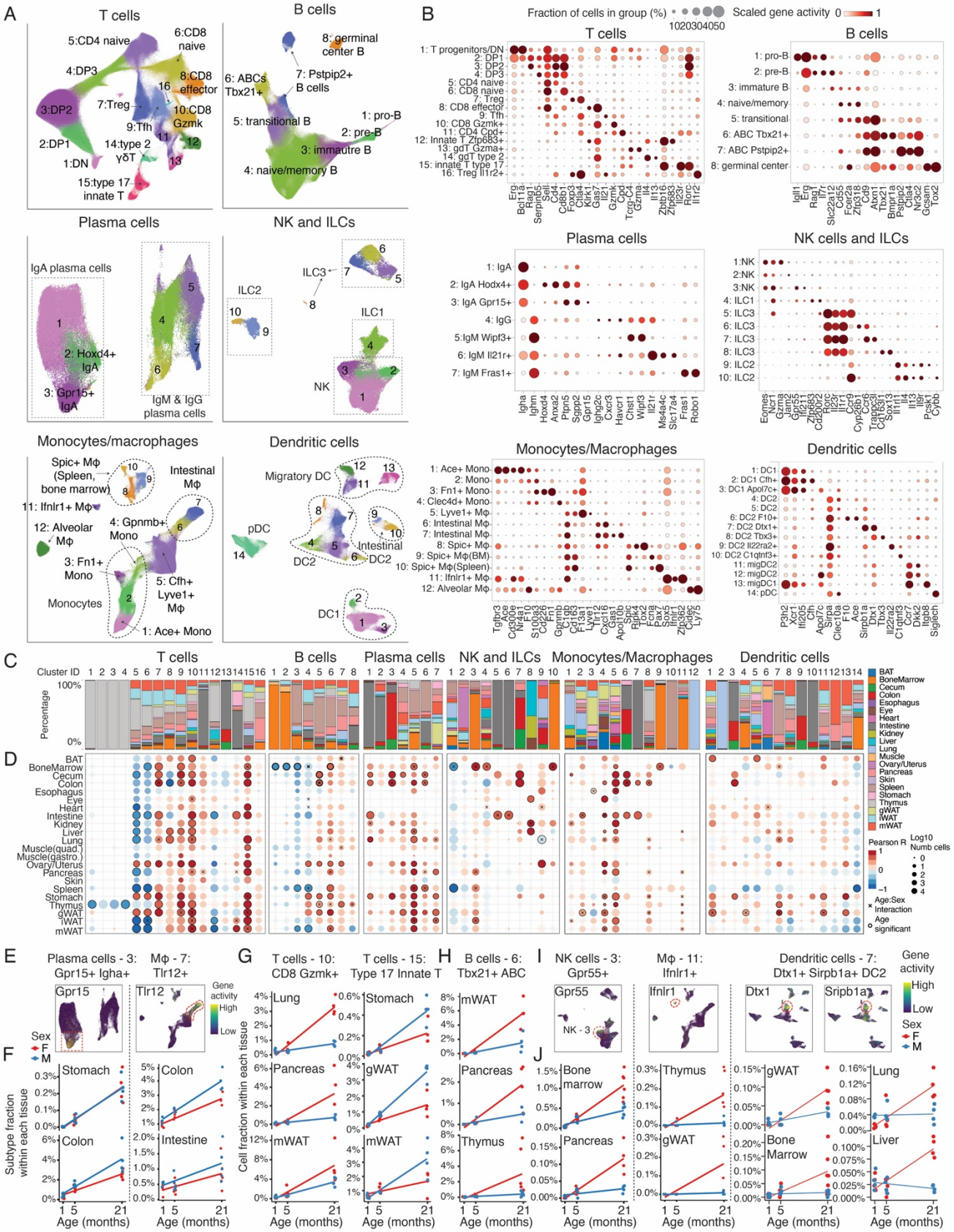
A
T cells
B cells
Plasma cells
NK and ILCs
Monocytes/macrophages
Dendritic cells
B
Fraction of cells in group (%)
Scaled gene activity
C
Cluster ID
Percentage
D
Pearson R
Log10 Numb cells
Age:Sex Interaction
Age significant
E
Plasma cells - 3: Gpr15+ Igha+
Mϕ - 7: Tlr12+
Gene activity
High
Low
Sex
F
M
F
Subtype fraction within each tissue
Age (months)
G
T cells - 10: CD8 Gzmk+
T cells - 15: Type 17 Innate T
Cell fraction within each tissue
H
B cells - 6: Tbx21+ ABC
I
NK cells - 3: Gpr55+
Mϕ - 11: Ifnlr1+
Dendritic cells - 7: Dtx1+ Sirpb1a+ DC2
J

Figure 4. Aging-associated dynamics of broadly distributed immune subtypes.

(A) UMAP plots showing combined clustering results for T cells, B cells, plasma cells, innate lymphoid cells, macrophages and dendritic cells across tissues, colored by subtype id.

(B) Dotplots showing accessibilities of genes used for annotating immune cell subtypes.

(C) Stacked bar plots showing the tissue composition for each immune subtype.

(D) Dotplots showing the proportional changes of each immune subtype in each tissue across aging, colored by Pearson correlation between their relative proportion (within each tissue) and age. Subtypes with significant age or age-sex interactions are marked.

(E) UMAP plots highlighting aging-expanded subtypes of plasma cell (left) and macrophage (right) in gastrointestinal tissues, colored by marker gene accessibility (*Gpr15* for plasma cell-3 and *Tlr12* for macrophage-7).

(F) Scatterplot showing the relative fractions of *Gpr15*+ *Igha*+ plasma cells and *Tlr12*+ macrophages along aging.

(G) Scatterplots showing the relative fractions of *Gzmk*+ CD8 T cells (left) and *Il23r*+ *Zbtb16*+ type 17 innate T cells (right) along aging, with separate linear regression fits for each sex.

(H) Scatterplot showing the relative fractions of *Tbx21*+ aging-associated B cells along aging, with separate linear regression fits for each sex.

(I) UMAP plots showing subtypes exhibiting female-biased expansion along aging, colored by accessibilities of marker genes. (*Gpr55 for NK-3*, *Ifnlr1* for macrophage-11, *Dtx1* and *Sirbp1a* for dendritic cells-7).

(J) Scatterplot showing the relative fractions of *Gpr55*+ NK cells (left), *Ifnlr1*+ macrophages (middle) and *Dtx1*+ *Sirbp1a*+ type 2 dendritic cells (right) along aging, with separate linear regression fits for each sex.

483 **Aging-associated population dynamics of broadly distributed non-immune subtypes**

484 Next, we expanded our analysis to aging-associated dynamics in non-immune cell populations, focusing
485 on vascular endothelial cells (VECs) (n = 426,160 cells, **Fig. 5A-B, top**), fibroblasts (n = 377,181 cells, **Fig.**
486 **5A-B, middle**), and smooth muscle cells (n = 101,284 cells, **Fig. 5A-B, bottom**), which are broadly
487 distributed across organs. Unlike immune cells that share molecular states across tissues, these non-
488 immune cell populations displayed remarkable organ specificity, with most (34 out of 61) clusters
489 dominated by a single tissue (>90% of cells from one tissue). For example, we identified VECs specific to
490 the liver (marked by *Gata4*) and the lung (marked by *Foxf1*) (**Fig. 5C**). The tissue specificity was further
491 confirmed through motif footprinting analyses of marker TFs (**Fig. 5D**), and consistent with previous study
492 (*72*). Similarly, tissue-specific TFs were observed in different fibroblast populations: *Six1* in bone marrow
493 fibroblasts, *Foxf1* in gastrointestinal fibroblasts, *Tbx20* in cardiac fibroblasts, *Hoxc9* in kidney fibroblasts,
494 and *Tbx5* in lung fibroblasts (**Fig. 5E**). We also identified subtypes exhibiting sex specificity. For instance,
495 we identified subtypes of smooth muscle cells unique to female gonadal organs (*e.g.,* ovary, uterus, and
496 gWAT). These cells were marked by the transcription factors *Wt1* and *Esr1,* supported by both gene
497 accessibility and motif activity (**Fig. 5F**).

498 We further examined how these broadly distributed non-immune subtypes changed with aging (**Fig. 5G**).
499 Compared to immune cells that overall expand across organs, these broadly distributed non-immune cell
500 types exhibited strong tissue-specific changes during aging (**Fig. 5G**). For example, we observed an age-
501 associated depletion of various organ-specific endothelial subtypes, such as cells in the kidney (VEC-14,
502 *Igf1*+ kidney medulla endothelial), lung (VEC-7, *Tbx2*+ lung aerocytes), and muscle (VEC-1, *Aqp7*+) (**Fig.**
503 **5G and S9A**). By contrast, organ-specific endothelial cells in the liver (VEC-9, *Clec4g*+ sinusoidal
504 endothelial) and pancreas (VEC-4, *Lamb1*+ VECs) expanded significantly during aging (**Fig. 5G and S9B**).
505 The expansion of liver sinusoidal endothelial cells aligns with previous findings from *Tabula Muris*
506 *Senis(57)*. Fibroblasts (FB) likewise displayed tissue-specific aging trajectories, showing expansion in
507 aged bone marrow (*Btla*+ FB-13), colon (*Edil3*+ FB-21), cecum (*Prkcq*+ FB-19), stomach (*Csf2rb*+ FB-3),
508 and mWAT (*Nkx6-1*+ FB-17) (**Fig. 5G and S9C**). In contrast, two fibroblast subtypes (ovary *Tgfa*+ FB-9
509 and stomach *Sox6*+ FB-23) significantly decreased in aging (**Fig. 5G and S9D**). For smooth muscle cell
510 (SMC) subtypes, there is a strong depletion of several subtypes across organs, such as colon (*Hoxd3*+
511 SMC-15), lung (*Tbx5*+ SMC-3), and ovary/uterus (*Gata2*+ SMC-2) (**Fig. 5G and S9F**). In the cecum,
512 however, there was an increased population of SMCs marked by inflammatory gene markers such as *Il7*
513 and *Serpina1c* (SMC-5, **Fig. 5G and S9G**).

514 Importantly, we identified several cell subtypes that shared similar aging dynamics across multiple tissues.
515 For example, a *Slc7a14*+ *Lhx6*+ *Meox2*+ vein endothelial cell subtype (VEC-5) was significantly depleted
516 in several aged tissues (*e.g.,* muscle, gWAT, and ovary/uterus) (**Fig. 5H-II**), which could contribute to the
517 endothelium dysfunction in aging. Likewise, an aging-associated fibroblast subtype characterized by
518 elevated inflammatory markers (*e.g., Ifi207*, *Ifi205*, *Ear1*) expanded in several aged organs (*e.g.,* mWAT,
519 stomach, cecum, esophagus) in a male-specific manner (**Fig. 5J-K**). Of note, these aging-associated
520 subtype dynamics were validated through external datasets (*7*), such as the depletion of *Lhx6*+ endothelial
521 cells in gWAT (**Fig. 5L-M)** and the expansion of *Csf2rb*+ fibroblasts in the stomach (**Fig. S9E**).

522

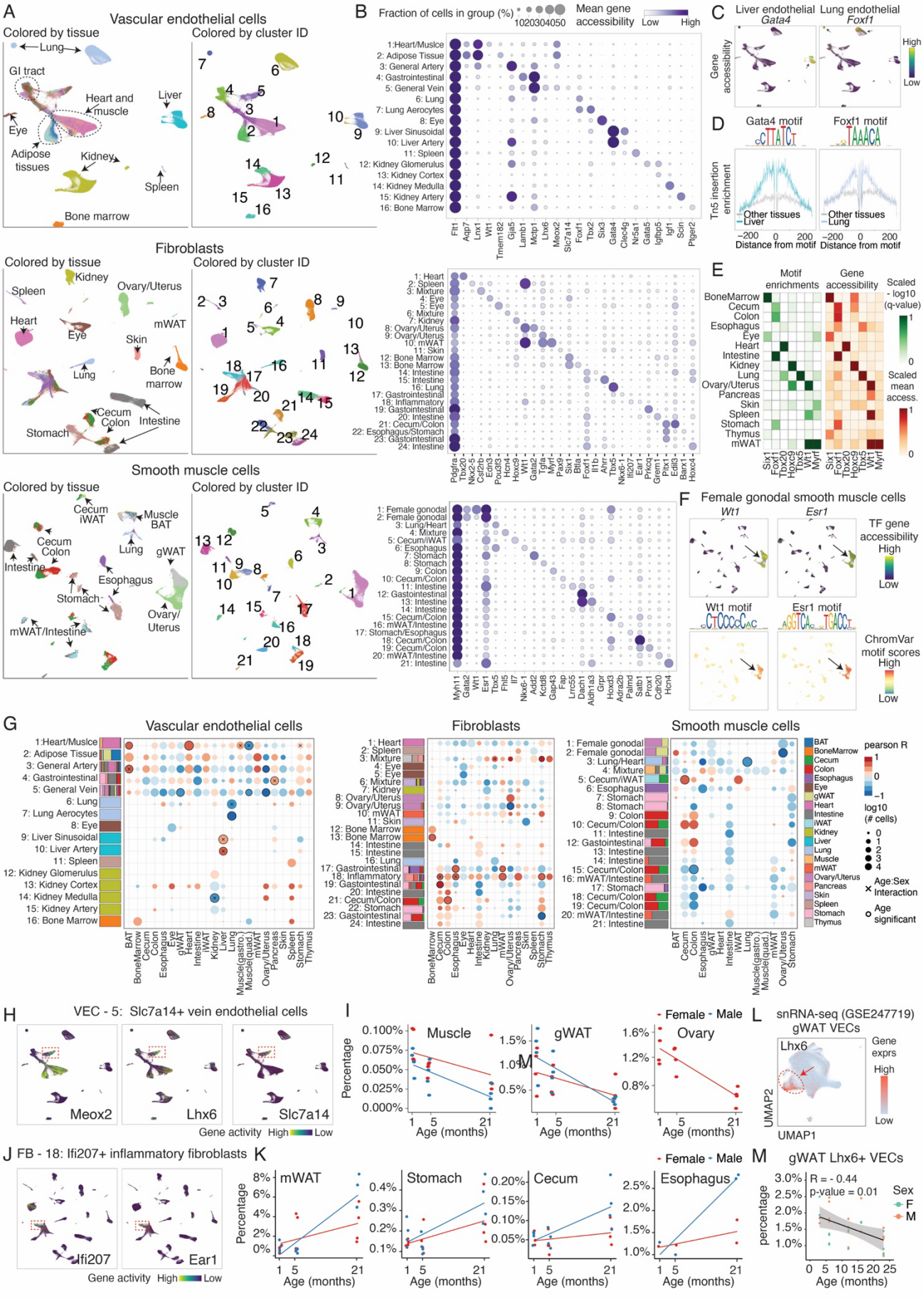
A
Vascular endothelial cells
Colored by tissue
Colored by cluster ID
Lung
GI tract
Heart and muscle
Liver
Eye
Adipose tissues
Kidney
Spleen
Bone marrow
Fibroblasts
Colored by tissue
Colored by cluster ID
Kidney
Spleen
Ovary/Uterus
Heart
Eye
mWAT
Skin
Lung
Bone marrow
Cecum
Colon
Intestine
Stomach
Smooth muscle cells
Colored by tissue
Colored by cluster ID
Cecum iWAT
Muscle BAT
Cecum
Colon
Lung
gWAT
Intestine
Esophagus
Stomach
Ovary/ Uterus
mWAT/Intestine
B
Fraction of cells in group (%)
Mean gene accessibility
Low
High
1:Heart/Muslce
2: Adipose Tissue
3: General Artery
4: Gastrointestinal
5: General Vein
6: Lung
7: Lung Aerocytes
8: Eye
9: Liver Sinusoidal
10: Liver Artery
11: Spleen
12: Kidney Glomerulus
13: Kidney Cortex
14: Kidney Medulla
15: Kidney Artery
16: Bone Marrow
1: Heart
2: Spleen
3: Mixture
4: Eye
5: Eye
6: Mixture
7: Kidney
8: Ovary/Uterus
9: Ovary/Uterus
10: mWAT
11: Skin
12: Bone Marrow
13: Bone Marrow
14: Intestine
15: Intestine
16: Lung
17: Gastrointestinal
18: Inflammatory
19: Gastointestinal
20: Intestine
21: Cecum/Colon
22: Esophagus/Stomach
23: Gastointestinal
24: Intestine
1: Female gonodal
2: Female gonodal
3: Lung/Heart
4: Mixture
5: Cecum/iWAT
6: Esophagus
7: Stomach
8: Stomach
9: Colon
10: Cecum/Colon
11: Intestine
12: Gastointestinal
13: Intestine
14: Intestine
15: Cecum/Colon
16: mWAT/Intestine
17: Stomach/Esophagus
18: Cecum/Colon
19: Cecum/Colon
20: mWAT/Intestine
21: Intestine
C
Liver endothelial
Lung endothelial
Gata4
Foxf1
Gene accessibility
High
Low
D
Gata4 motif
Foxf1 motif
Tn5 insertion enrichment
Other tissues
Liver
Other tissues
Lung
Distance from motif
Distance from motif
E
Motif enrichments
Gene accessibility
Scaled - log10 (q-value)
Scaled mean access.
BoneMarrow
Cecum
Colon
Esophagus
Eye
Heart
Intestine
Kidney
Lung
Ovary/Uterus
Pancreas
Skin
Spleen
Stomach
Thymus
mWAT
F
Female gonodal smooth muscle cells
Wt1
Esr1
TF gene accessibility
High
Low
Wt1 motif
Esr1 motif
ChromVar motif scores
High
Low
G
Vascular endothelial cells
Fibroblasts
Smooth muscle cells
pearson R
log10 (# cells)
Age:Sex Interaction
Age significant
BAT
BoneMarrow
Cecum
Colon
Esophagus
Eye
gWAT
Heart
Intestine
iWAT
Kidney
Liver
Lung
Muscle
mWAT
Ovary/Uterus
Pancreas
Skin
Spleen
Stomach
Thymus
H
VEC - 5: Slc7a14+ vein endothelial cells
Meox2
Lhx6
Slc7a14
Gene activity
High
Low
I
Muscle
gWAT
Ovary
Female
Male
Percentage
Age (months)
L
snRNA-seq (GSE247719)
gWAT VECs
Lhx6
Gene exprs
High
Low
UMAP1
UMAP2
J
FB - 18: Ifi207+ inflammatory fibroblasts
Ifi207
Ear1
Gene activity
High
Low
K
mWAT
Stomach
Cecum
Esophagus
Female
Male
Percentage
Age (months)
M
gWAT Lhx6+ VECs
R = - 0.44
p-value = 0.01
Sex
F
M
percentage
Age (months)

Figure 5. Aging-associated dynamics of vascular endothelial cells, fibroblasts, and smooth muscle cells across organs.

(A) UMAP visualization showing the combined clustering for vascular endothelial cells (VECs, top), fibroblasts (FBs, middle) and smooth muscle cells (SMCs, bottom) across tissues, colored by tissue origin (Left) and cluster ID (Right).

(B) Dot plots showing the accessibility of marker genes for cell clusters of VEC (top), FB (middle) and SMC (bottom), including a general marker for each cell type (*Flt1* for VEC, *Pdgfra* for FBs, *Myh11* for SMCs)

(C) UMAP plot of VECs colored by accessibilities of the liver VEC marker *Gata4* and lung VEC marker *Foxf1*

(D) Motif footprinting analysis showing enrichment of GATA4 motifs in liver VECs and FOXF1 motifs in lung VECs compared with other tissues.

(E) Heatmaps showing the motif enrichments and gene body accessibility of tissue-specific transcription factors. Motif enrichment scores (-log10 q-value) were computed with HOMER (*73*) using tissue-specific peaks and scaled to the top enriched tissue.

(F) UMAP plots of SMCs colored by gene accessibility (Top) and chromVar motif deviation scores (Bottom) for gonadal SMC markers *Wt1* and *Esr1*.

(G) The stacking bar plots show tissue composition per cluster for VECs (Left), FBs (Middle), and SMCs (Right). The dot plots show aging-associated proportional changes of clusters across tissues, colored by Pearson correlation between cluster proportion (normalized per tissue) and age. Clusters with significant age/age-sex effects are annotated (p-adjusted < 0.05).

(H) UMAP of VECs colored by the accessibility of VEC-5 markers (*Meox2*, *Lhx6*, *Slc7a14*).

(I) Scatterplots showing the age-related decline in VEC-5 proportions in muscle (quadriceps), gonadal white adipose tissue (gWAT), and ovary/uterus.

(J) UMAP of FBs colored by the accessibility of FB-18 markers (*Ifi207*, *Ear1*).

(K) Scatterplots showing the age-associated increase in FB-5 proportions in mesenteric WAT (mWAT), stomach, cecum, and esophagus.

(L) UMAP plot showing gWAT VEC cells isolated from snRNA-seq data (*7*), colored by *Lhx6* expression (VEC-5 marker).

(M) Scatterplot showing age-dependent reduction in *Lhx6*+ gWAT endothelial cells.

Age- and sex-dependent epigenetic signatures of aging

We next investigated the organism-wide epigenetic aging program by examining 349 organ-specific main cell types. For each major cell type in each tissue, we performed differential accessibility (DA) analyses in females and males separately (**Methods**). From these analyses, we identified both shared and sex-specific age-associated alterations in chromatin accessibility. We then carried out linkage analysis to map downstream genetic targets of these chromatin sites and examined upstream regulators by assessing the activity of intrinsic transcription factors and extrinsic cytokine signaling pathways that drive epigenetic reprogramming during mammalian aging (**Fig. 6A**).

In total, we identified 1,318,007 and 959,361 cell-type-specific and aging-associated DA peaks in females and males, respectively (**Fig. 6B, Fig. S10A, Table S6-S8**). While the number of DA peaks generally correlated with cell numbers, a few cell types exhibited notably strong aging-related chromatin changes, standing out as outliers with high regression residuals—such as B cells from brown adipose tissue or kidney, tenocytes, and muscle satellite cells (**Fig. S10B**). Among the identified DA peaks, a total of 540,386 cell-type-specific DA peaks were present in both sexes, most (96.9%) exhibiting consistent changes in the same cell type across both males and females (Spearman correlation of log transformed fold change = 0.86, p-value < $2.2 * 10^{-16}$, **Fig. 6C-D**).

While many DA peaks were restricted to only a few cell types (91.4% found in no more than 3 cell types), we also uncovered a subset of peaks (n = 803) that were consistently altered across many cell types (n >= 10) and tissues (**Fig. 6E**). This subset highlights coordinated chromatin dynamics across diverse cell types and regions during mammalian aging. Notable examples include increased promoter accessibility of the mineralocorticoid receptor *Nr3c2* (in 63 cell types, **Fig. 6F-G, left**) and the proinflammatory cytokine *Il7* (in 26 cell types, **Fig. 6F-G, middle left**), predominantly within immune cells. Increased *Nr3c2* activity also marked the aging-associated B cell states (**Fig. 4B**). Conversely, we identified DA peaks with decreased accessibility in aging, such as promoters of *Sox4* (in 25 cell types) and *Sox11* (in 19 cell types)(**Fig. 6E**). Specifically, *Sox11*, a transcription factor involved in angiogenesis (*74*), showed reduced accessibility in endothelial cells across multiple organs (**Fig. 6F-G, middle right**), which could contribute to the global functional decline of the vascular system.

Aging-associated chromatin alterations were not always uniform across cell types. For example, 131 peaks showed opposite changes in different cell types (at least five cell types in each direction). One example is a peak in the intron of *Epha3*, which displayed increased accessibility in T cells and macrophages across 12 tissues but decreased accessibility in non-immune cell types such as vascular cells, neurons, and epithelial cells (**Fig. 6F-G, right, Fig. S10C**). These cell-type-specific patterns were confirmed across both sexes (**Fig. 6F**), suggesting that aging-associated chromatin alterations are shaped by unique cellular contexts and lineage-specific regulatory networks.

These epigenetic changes in aging also vary by sex. Considering peaks with significantly increased accessibility in aging, we found 195,893 sex-specific peaks in females and 140,770 in males (**Fig. 6H**). Top female-specific DA peaks validated across multiple cell types from different tissues included intronic peaks at the senescence-associated gene *Cdkn2b* (in 18 cell types) and promoter peaks of the interferon-inducible gene *Ligp1* (in 14 cell types) and *Ifi211* (in 16 cell types) (**Fig. 6H**). Similarly, we observed male-specific DA peaks shared across multiple cell types, such as the increased promoter accessibility of *Tsbp1* across 18 cell types (**Fig. 6H**). We also identified cell-type-specific chromatin accessibility changes that were highly sex-dependent. For example, aged hepatocytes in females showed up-regulation of peaks overlapping with *Bnc2* (**Fig. 6I, left)**, a gene involved in extracellular matrix production and degradation

(*75*). In contrast, aged hepatocytes in males showed up-regulation of peaks overlapping with *Cidea* (**Fig. S6D, left**), a gene involved in lipid particle organizations. Similarly, in a subtype of proximal tubule cells segment 3 (PT S3T2), peaks overlapping *Mill2* were more accessible in aged females (**Fig. S6D, right**), whereas intronic peaks in *Tifa*—a gene associated with programmed cell death (*76*)—were more accessible in aged males (**Fig. 6I, right**). Consistent with these findings, this cellular state specifically declined in aged males (**Fig. 2H**). Notably, these sex- and cell-type-specific peaks were further validated by corresponding changes in promoter accessibility and gene expression during aging (**Fig. 6I-J and S6E**).

To infer putative target genes of aging-associated chromatin alterations in cis-regulatory elements (CRE), we linked non-promoter DA peaks to nearby promoters based on their co-accessibility across samples for each cell type, thus generating promoter-CRE linkages. We then integrated the data with a published snRNA-seq atlas of aging (*7*) to identify genes exhibiting consistent changes between promoters and expressions with age (**Methods**). This analysis identified 21,360 and 14,564 cell-type-specific gene-promoter-CRE linkages in males and females, respectively, with 12,862 linkages shared by both sexes (**Table S9**). In total, this revealed 15,090 CREs linked to aging-associated changes in 2,001 differentially expressed (DE) genes across 86 organ-specific cell types (**Fig. 6K**). Collapsing sex-shared, up-regulation linkages across cell types revealed concordant changes supported in three molecular evidences (i.e, genes, promoters and putative enhancers) (**Fig. 6L**). One notable example is *Nr3c2*, linked to 25 CREs, most located in intronic regions (**Fig. 6M**). These CREs showed strongly increased accessibility during aging across multiple immune cell types and tissues, in line with changes in promoter accessibility and gene expression from the same cell type (**Fig. 6N**).

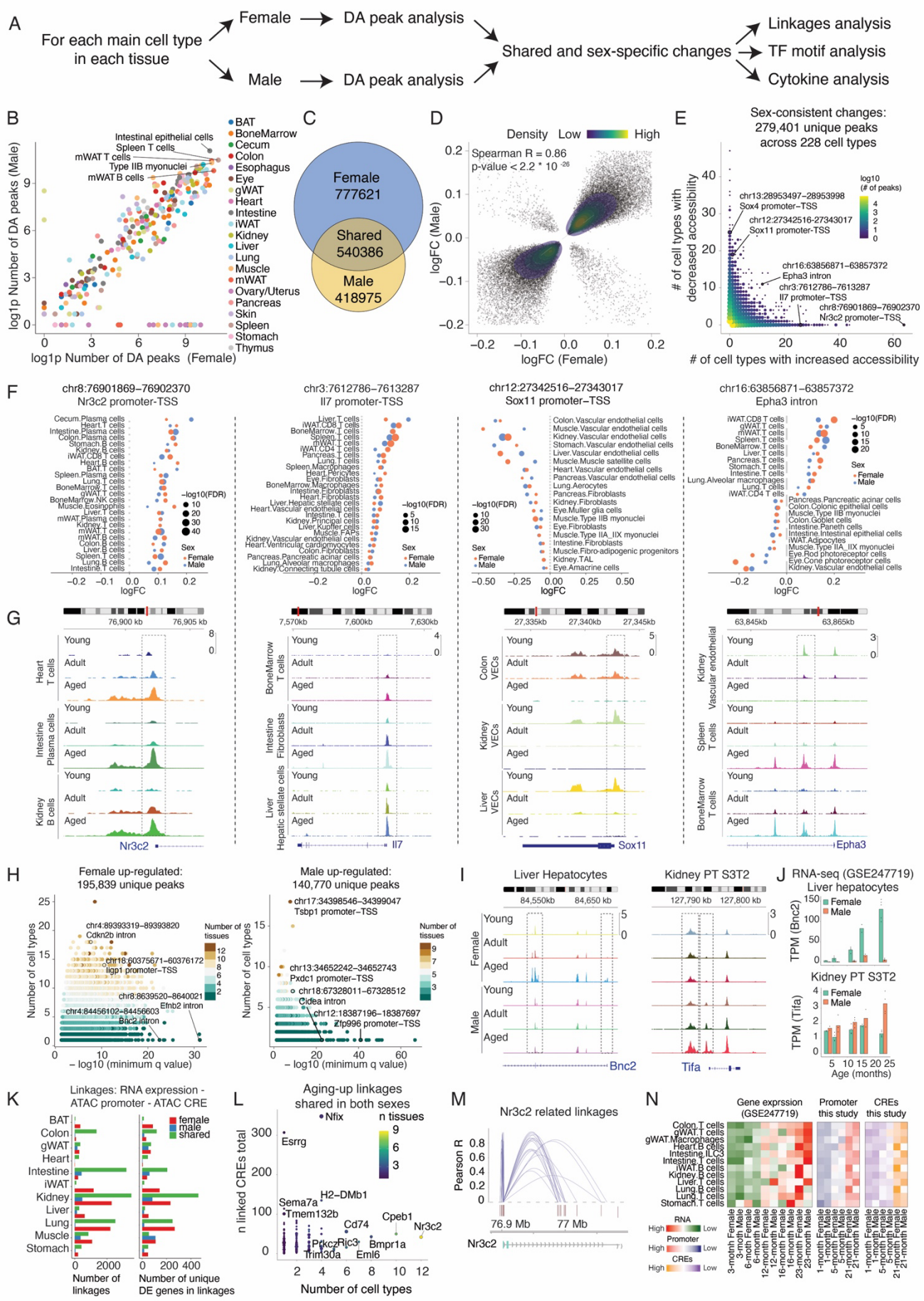
A
For each main cell type in each tissue
Female
DA peak analysis
Male
DA peak analysis
Shared and sex-specific changes
Linkages analysis
TF motif analysis
Cytokine analysis
B
log1p Number of DA peaks (Male)
log1p Number of DA peaks (Female)
Intestinal epithelial cells
Spleen T cells
mWAT T cells
Type IIB myonuclei
mWAT B cells
BAT
BoneMarrow
Cecum
Colon
Esophagus
Eye
gWAT
Heart
Intestine
iWAT
Kidney
Liver
Lung
Muscle
mWAT
Ovary/Uterus
Pancreas
Skin
Spleen
Stomach
Thymus
C
Female 777621
Shared 540386
Male 418975
D
Density Low High
Spearman R = 0.86
p-value < 2.2 * 10 -26
logFC (Male)
logFC (Female)
E
Sex-consistent changes: 279,401 unique peaks across 228 cell types
# of cell types with decreased accessibility
# of cell types with increased accessibility
log10 (# of peaks)
chr13:28953497–28953998
Sox4 promoter–TSS
chr12:27342516-27343017
Sox11 promoter-TSS
chr16:63856871–63857372
Epha3 intron
chr3:7612786–7613287
Il7 promoter–TSS
chr8:76901869–76902370
Nr3c2 promoter–TSS
F
chr8:76901869–76902370
Nr3c2 promoter-TSS
chr3:7612786–7613287
Il7 promoter-TSS
chr12:27342516–27343017
Sox11 promoter–TSS
chr16:63856871–63857372
Epha3 intron
–log10(FDR)
Sex
Female
Male
logFC
G
Young
Adult
Aged
Heart T cells
Intestine Plasma cells
Kidney B cells
BoneMarrow T cells
Intestine Fibroblasts
Liver Hepatic stellate cells
Colon VECs
Kidney VECs
Liver VECs
Kidney Vascular endothelial
Spleen T cells
BoneMarrow T cells
Nr3c2
Il7
Sox11
Epha3
H
Female up-regulated: 195,839 unique peaks
Male up-regulated: 140,770 unique peaks
Number of cell types
– log10 (minimum q value)
Number of tissues
chr4:89393319–89393820
Cdkn2b intron
chr18:60375671–60376172
Iigp1 promoter–TSS
chr8:8639520–8640021
Efnb2 intron
chr4:84456102–84456603
Bnc2 intron
chr17:34398546–34399047
Tsbp1 promoter–TSS
chr13:34652242–34652743
Pxdc1 promoter–TSS
chr18:67328011–67328512
Cidea intron
chr12:18387196–18387697
Zfp996 promoter–TSS
I
Liver Hepatocytes
Kidney PT S3T2
Female
Male
Young
Adult
Aged
Bnc2
Tifa
J
RNA-seq (GSE247719)
Liver hepatocytes
Kidney PT S3T2
TPM (Bnc2)
TPM (Tifa)
Female
Male
Age (months)
K
Linkages: RNA expression - ATAC promoter - ATAC CRE
BAT
Colon
gWAT
Heart
Intestine
iWAT
Kidney
Liver
Lung
Muscle
Stomach
female
male
shared
Number of linkages
Number of unique DE genes in linkages
L
Aging-up linkages shared in both sexes
n linked CREs total
n tissues
Nfix
Esrrg
H2–DMb1
Sema7a
Tmem132b
Cd74
Cpeb1
Nr3c2
Prkcz
Ric3
Bmpr1a
Trim30a
Eml6
Number of cell types
M
Nr3c2 related linkages
Pearson R
76.9 Mb
77 Mb
Nr3c2
N
Gene exprssion (GSE247719)
Promoter this study
CREs this study
Colon.T cells
gWAT.T cells
gWAT.Macrophages
Heart.B cells
Intestine.ILC3
Intestine.T cells
iWAT.B cells
Kidney.B cells
Liver.T cells
Lung.B cells
Lung.T cells
Stomach.T cells
RNA
Promoter
CREs
High
Low
3-month Female
6-month Female
12-month Female
16-month Female
23-month Female
3-month Male
6-month Male
12-month Male
16-month Male
23-month Male
1-month Female
5-month Female
21-month Female
1-month Male
5-month Male
21-month Male

Figure 6. Aging-associated changes of chromatin accessibility.

(A) Scheme for computational analyses to identify differentially accessible (DA) peaks along aging, their putative gene targets, and upstream regulators.

(B) Scatterplot comparing the number of DA peaks between males and females for each main cell type. Cell types with a high number of DA peaks are labeled.

(C) Venn plot of cell-type-specific DA peaks shared or unique to males and females.

(D) Correlation of log transformed fold change (logFC, aging-associated accessibility changes per month, calculated via edgeR (*77*)) for DA peaks shared between sexes.

(E) Scatterplot summarizing DA peaks with concordant changes with aging in both sexes. Axes show counts of cell types with increased (x-axis) or decreased (y-axis) accessibility; color denotes peak density.

(F) Dot plots showing log transformed fold change (logFC) for DA peaks with consistent increases (promoters of *Nr3c2* and *Il7*), decreases (promoters of *Sox4*), or divergent trends (intronic peak of *Epha3*) across cell types.

(G) Genomic tracks visualizing the accessibilities of DA peaks in (**F**) across three age groups.

(H) Dot plots of sex-specific DA peaks for females (Left) and males (Right). Y-axis: number of cell types with significant increases; x-axis: -log10(q-value) for the most significant cell type. Color denotes the number of tissues with significant increases.

(I) Genomic tracks of female-specific DA peak in liver hepatocytes (Left) and male-specific DA peak kidney proximal tubule cells S3T2 (Right).

(J) Barplot showing validation of sex-specific chromatin accessibility changes using gene expression data (*7*) of the same genes in the same cell type as in (**I**). Dots represent gene expression of target genes across independent animals, quantified by transcripts per million (TPM).

(K) Barplot showing the number of cell-type-specific, aging-associated gene-promoter-CRE linkages (Left) and the number of unique genes within those linkages (Right) for each tissue.

(L) Dot plot of genes with aging-upregulated linkages in both sexes. X-axis: cell-type count; y-axis: CRE count per gene. Color denotes the number of tissues containing cell types with significant increases.

(M) Genome browser plot showing links between putative cis-regulatory elements and promoters for *Nr3c2*.

(N) Heatmaps showing coordinated increases in gene expression, promoter accessibility, and linked distal CRE accessibility of *Nr3c2* across multiple immune cells with aging.

Intrinsic and extrinsic regulators of epigenetic reprogramming in mammalian aging

We then explored upstream regulators of these aging-associated chromatin changes by performing motif enrichment analyses of DA peaks in each cell type. Aging-upregulated peaks were enriched for inflammatory motifs that are confirmed across multiple cell types, including IFN-stimulated response elements (ISRE) in 80 cell types, IRF1 in 77 cell types, IRF2 in 85 cell types, NF-κB in 57 cell types, and AP-1 in 71 cell types (**Fig. 7A-B**). In contrast, downregulated peaks were enriched for TF families linked to stem cell maintenance and development, such as *SOX15* (in 18 cell types) and *E2A* (in 29 cell types) (**Fig. 7A**). Sex-specific patterns also emerged. For example, female-specific upregulated peaks were enriched for *POU* motifs in B cells and male-specific upregulated peaks were enriched for inflammatory TF motifs (IRFs and AP-1) in intestinal epithelial cells (**Fig. 7C**).

These TF activity changes were further supported by corresponding gene expression dynamics observed in single-cell RNA-seq data. For example, in the aged B cells in the lung, we detected reduced motif accessibility for Ebf1 and Ets1 (**Fig. 7D-E**), transcription factors involved in B cell development (*25*) and quiescent state maintenance (*78*), aligning with their decreased expression in both sexes (**Fig. 7F**). Meanwhile, aged B cells exhibited decreased expression and increased motif accessibility for Irf2 (**Fig. 7D-E**), reflecting its role as a transcriptional repressor of inflammatory signaling (*79*, *80*). Pou2f2, a TF involved in B proliferation and plasma cell differentiation(*81*), showed increased motif accessibility exclusively in female-upregulated peak sets, corroborated by female-specific increases in Pou2f2 expression(**Fig. 7D-E**). This pattern is consistent with the preferential expansion of aging-associated B cells in female tissues (**Fig. 4D and 4H**). Moreover, the aging-associated changes in EBF and IRF motifs were detected in B cells body-wide, highlighting a global chromatin transition in B cells during aging (**Fig. 7G**).

Recognizing the strong inflammatory signature underlying these changes, we next explored whether cytokines known to drive immune responses could contribute to global epigenetic remodeling. Using the Immune Dictionary dataset (*82*), which encompasses scRNA-seq profiles of various immune cell types responding to 86 cytokines, we compared aging-related DA peaks and associated gene changes with those induced by different cytokines (**Fig. 7H, Methods**). This revealed that aging signatures, especially in female B cells from the lung, resembled those induced by specific cytokines such as interferons (IFNs), IL4, IL12, IL15, IL18, and IL21 (**Fig. 7I**). Cross-referencing aging-upregulated gene expression changes with cytokine-responsive transcripts further validated these links (**Fig. 7J**).

To reinforce this connection, we examined whether cytokine signatures were supported by changes in the accessibility of either secretion or receptor genes (**Fig. 7K-L**). For example, for secretion factors, we observed an increased accessibility of *Infg* and *Il21* in T cells, as well as *Il4* and *Il15* in B cells (**Fig. 7L**), aligning with activation of corresponding signatures, particularly in females (**Fig. 7I**). On the other hand, the upregulated response to IL2 and IL15 matched with increased accessibility of the receptor gene, *Il2rb*, in the aged B cells (**Fig. 7L**). A consistent trend was observed by analysis of recent snRNA-seq data (*7*), such as the increased expression of *Il21* in T cells, *Il2rb* and *Il15* in B cells (**Fig. 7N** and **Fig. S10F**).

Extending this analysis to all B cells across tissues uncovered the widespread emergence of cytokine signatures associated with aging, especially IL2, IL15, IFNγ, IL4, and IL21(**Fig. 7M**). Notably, the upregulated IL21 signatures were consistent with the global expansion of *Il21*+ T cells from in our previous analysis (**T cells - 9, Fig. 4B and 4D**) and were further confirmed at the plasma protein level in humans (*3*)(**Fig. S10G**). Interestingly, a previous study has described the function of IL21 in inducing the expression of Tbx21 (a marker of aging-associated B cells, **Fig. 4B**) in B cells and promoting their differentiation into

plasma cells in systemic lupus erythematosus (*83*), suggesting a potential similar role of *Il21* in the epigenome reprogramming of B cells during aging. Similarly, we analyzed cytokine signatures in macrophages by leveraging expression changes following cytokine treatments of the same cell type from Immune Dictionary. This revealed activation of a distinct set of cytokines, including IL15, IL7, IL1α, IL18, and TNFα (**Fig. S10H**), that may underlie age-related molecular shifts in macrophages.

In summary, our integrative multi-level framework reveals a global, sex-dependent epigenetic reprogramming linked to inflammatory signaling and cytokine-driven pathways. These findings provide a roadmap for understanding the regulatory underpinnings of aging across diverse cell types and tissues—from intrinsic TF regulators to extrinsic cytokine signaling—and highlight candidate upstream factors that could be targeted to mitigate age-related epigenetic dysregulation.

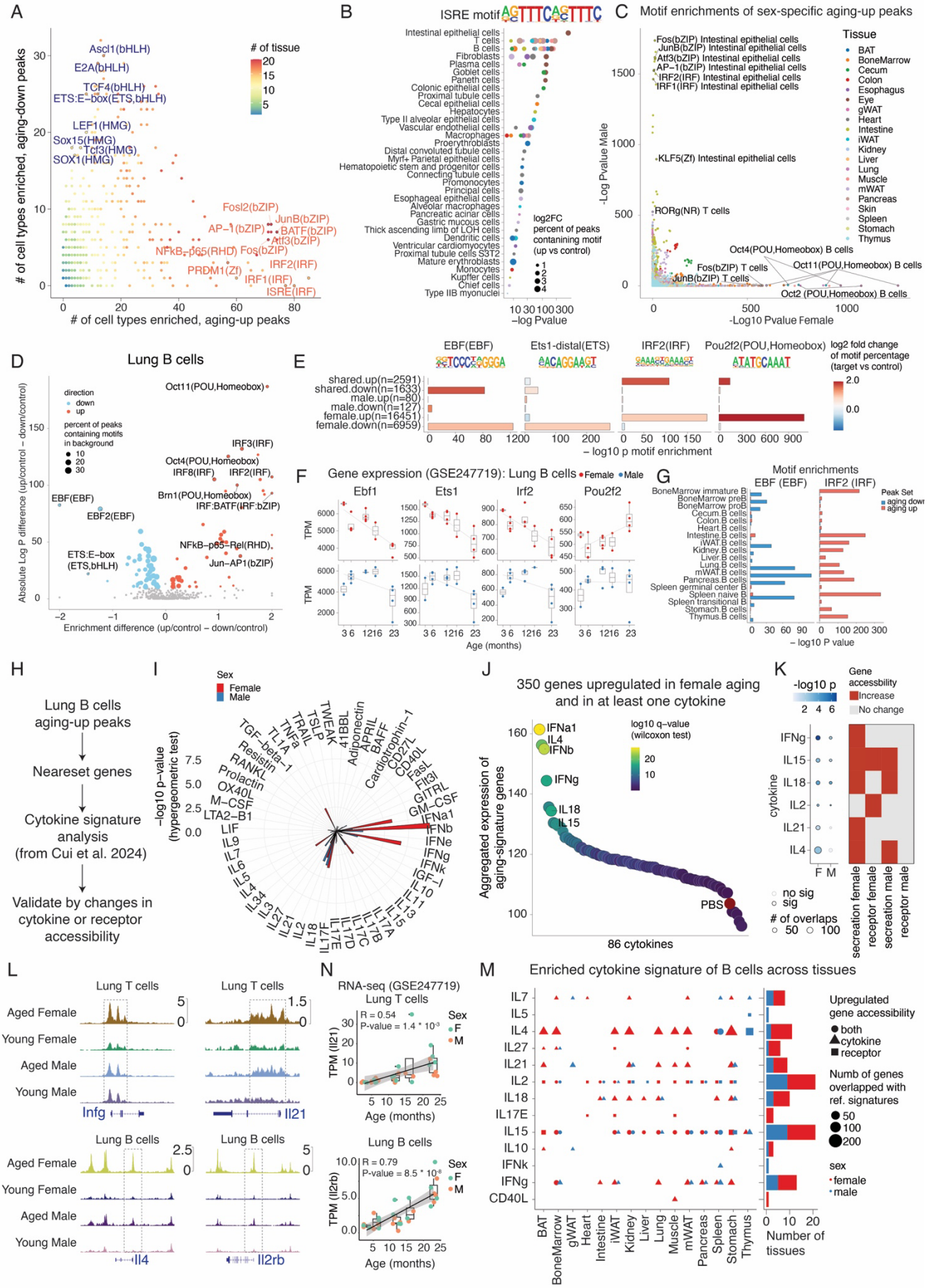
A
# of cell types enriched, aging-down peaks
# of cell types enriched, aging-up peaks
# of tissue
Ascl1(bHLH)
E2A(bHLH)
TCF4(bHLH)
ETS:E-box(ETS,bHLH)
LEF1(HMG)
Sox15(HMG)
Tcf3(HMG)
SOX1(HMG)
Fosl2(bZIP)
JunB(bZIP)
AP-1(bZIP)
BATF(bZIP)
Atf3(bZIP)
NFkB-p65(RHD)
Fos(bZIP)
IRF2(IRF)
PRDM1(Zf)
IRF1(IRF)
ISRE(IRF)
B
ISRE motif
Intestinal epithelial cells
T cells
B cells
Fibroblasts
Plasma cells
Goblet cells
Paneth cells
Colonic epithelial cells
Proximal tubule cells
Cecal epithelial cells
Hepatocytes
Type II alveolar epithelial cells
Vascular endothelial cells
Macrophages
Proerythroblasts
Distal convoluted tubule cells
Myrf+ Parietal epithelial cells
Hematopoietic stem and progenitor cells
Connecting tubule cells
Promonocytes
Principal cells
Esophageal epithelial cells
Alveolar macrophages
Pancreatic acinar cells
Gastric mucous cells
Thick ascending limb of LOH cells
Dendritic cells
Ventricular cardiomyocytes
Proximal tubule cells S3T2
Mature erythroblasts
Monocytes
Kupffer cells
Chief cells
Type IIB myonuclei
log2FC
percent of peaks
containing motif
(up vs control)
−log Pvalue
C
Motif enrichments of sex-specific aging-up peaks
Fos(bZIP) Intestinal epithelial cells
JunB(bZIP) Intestinal epithelial cells
Atf3(bZIP) Intestinal epithelial cells
AP-1(bZIP) Intestinal epithelial cells
IRF2(IRF) Intestinal epithelial cells
IRF1(IRF) Intestinal epithelial cells
KLF5(Zf) Intestinal epithelial cells
RORg(NR) T cells
Oct4(POU,Homeobox) B cells
Oct11(POU,Homeobox) B cells
Fos(bZIP) T cells
JunB(bZIP) T cells
Oct2 (POU,Homeobox) B cells
-Log Pvalue Male
-Log10 Pvalue Female
Tissue
BAT
BoneMarrow
Cecum
Colon
Esophagus
Eye
gWAT
Heart
Intestine
iWAT
Kidney
Liver
Lung
Muscle
mWAT
Pancreas
Skin
Spleen
Stomach
Thymus
D
Lung B cells
direction
down
up
percent of peaks
containing motifs
in background
Oct11(POU,Homeobox)
IRF3(IRF)
Oct4(POU,Homeobox)
IRF8(IRF)
IRF2(IRF)
EBF(EBF)
EBF2(EBF)
Brn1(POU,Homeobox)
IRF:BATF(IRF:bZIP)
NFkB-p65-Rel(RHD)
ETS:E-box
(ETS,bHLH)
Jun-AP1(bZIP)
Absolute Log P difference (up/control − down/control)
Enrichment difference (up/control − down/control)
E
EBF(EBF)
Ets1-distal(ETS)
IRF2(IRF)
Pou2f2(POU,Homeobox)
log2 fold change
of motif percentage
(target vs control)
shared.up(n=2591)
shared.down(n=1633)
male.up(n=80)
male.down(n=127)
female.up(n=16451)
female.down(n=6959)
− log10 p motif enrichment
F
Gene expression (GSE247719): Lung B cells
Female
Male
Ebf1
Ets1
Irf2
Pou2f2
TPM
Age (months)
G
Motif enrichments
EBF (EBF)
IRF2 (IRF)
Peak Set
aging down
aging up
BoneMarrow immature B
BoneMarrow preB
BoneMarrow proB
Cecum.B cells
Colon.B cells
Heart.B cells
Intestine.B cells
iWAT.B cells
Kidney.B cells
Liver.B cells
Lung.B cells
mWAT.B cells
Pancreas.B cells
Spleen germinal center B
Spleen naive B
Spleen transitional B
Stomach.B cells
Thymus.B cells
− log10 P value
H
Lung B cells
aging-up peaks
Neareset genes
Cytokine signature
analysis
(from Cui et al. 2024)
Validate by changes in
cytokine or receptor
accessibility
I
Sex
Female
Male
−log10 p−value
(hypergeometric test)
TGF−beta−1
Resistin
RANKL
Prolactin
OX40L
M−CSF
LTA2−B1
LIF
IL9
IL7
IL6
IL5
IL4
IL35
IL3
IL27
IL21
IL2
IL18
IL17F
IL17E
IL17D
IL17C
IL17B
IL17A
IL15
IL13
IL11
IL10
IGF−I
IFNk
IFNg
IFNe
IFNb
IFNa1
GM−CSF
GITRL
Flt3l
FasL
CD40L
CD27L
Cardiotrophin−1
APRIL
BAFF
Adiponectin
4−1BBL
TWEAK
TSLP
TRAIL
TNFa
TL1A
J
350 genes upregulated in female aging
and in at least one cytokine
log10 q−value
(wilcoxon test)
IFNa1
IL4
IFNb
IFNg
IL18
IL15
PBS
Aggregated expression of
aging-signature genes
86 cytokines
K
-log10 p
Gene
accessbility
Increase
No change
IFNg
IL15
IL18
IL2
IL21
IL4
cytokine
F M
no sig
sig
# of overlaps
50
100
secreation female
receptor female
secreation male
receptor male
L
Lung T cells
Aged Female
Young Female
Aged Male
Young Male
Infg
Il21
Lung B cells
Il4
Il2rb
N
RNA-seq (GSE247719)
Lung T cells
R = 0.54
P-value = 1.4 * 10-3
Sex
F
M
TPM (Il21)
Age (months)
Lung B cells
R = 0.79
P-value = 8.5 * 10-6
TPM (Il2rb)
M
Enriched cytokine signature of B cells across tissues
IL7
IL5
IL4
IL27
IL21
IL2
IL18
IL17E
IL15
IL10
IFNk
IFNg
CD40L
BAT
BoneMarrow
gWAT
Heart
Intestine
iWAT
Kidney
Liver
Lung
Muscle
mWAT
Pancreas
Spleen
Stomach
Thymus
Upregulated
gene accessibility
both
cytokine
receptor
Numb of genes
overlapped with
ref. signatures
50
100
200
sex
female
male
Number of
tissues

Figure 7. Identifying upstream regulators of aging-associated chromatin changes.

(A) Sex-shared aging-associated up-regulated and down-regulated differentially accessible (DA) peaks for each main cell type were analyzed for transcription factor (TF) motif enrichment using HOMER (*73*). The scatter plot summarizes the number of cell types exhibiting significant motif enrichments (p.adj < 0.05) in either up-regulated (red) or down-regulated (blue) peak sets. TF motifs enriched across multiple cell types are labeled.

(B) Dot plot showing the enrichment of interferon-stimulated response element (ISRE) motifs in aging-up DA peaks across cell types from diverse tissues. Dot size represents the fold change in ISRE-containing peaks in DA sets compared to a background peak set (**Methods**). Each dot represents one cell type from a specific tissue, colored by the tissue of origin.

(C) Comparison of TF motif enrichment significance between female-specific and male-specific aging-up peak sets for each main cell type. Cell types with strong sex-specific motif enrichments are labeled.

(D) Scatter plot showing enriched TF motifs in sex-shared, aging-up (red), and aging-down (blue) peaks from lung B cells. The x-axis denotes the difference in motif frequency (%) between DA and background peaks; the y-axis represents statistical significance.

(E) Barplots showing motif enrichment for exemplary TFs: Ebf1 and Ets1 (down-regulated in both sexes), Irf2 (up-regulated in both sexes), and Pou2f2 (female-biased up-regulation) in lung B cells.

(F) Scatterplot and barplot showing age-related expression changes of TFs highlighted in (**E**) in lung B cells, quantified using transcripts per million (TPM) for each animal.

(G) Enrichment significance of EBF and IRF motifs for DA peaks from B cells across tissues, demonstrating conserved aging-associated regulatory patterns.

(H) Scheme for computational analyses to identify cytokines potentially drive aging-associated chromatin remodeling in lung B cells.

(I) Circle plot showing enrichments (-log10(p-value), hypergeometric test) of cytokine-specific signatures (derived from Immune Dictionary dataset (*82*)) in aging-associated genes identified in lung B cells from this study.

(J) Dot plot displaying aggregated gene expressions of 350 genes shared between aging and cytokine treatments. Top conditions recapitulating aging-associated expression profiles were labeled.

(K) Left: dot plot showing the enrichment score (-log10(p-value), hypergeometric test) of cytokine signatures in the male and female lung B cells as in **(I)**. Right: Heatmap indicating the aging-associated changes in the accessibility of cytokine secretion or receptor genes.

(L) Genomic tracks showing aging-associated accessibility increases at *Ifng* and *Il21* in lung T cells and *Il4* and *Il2rb* in B cells.

(N) Scatterplot showing increased gene expressions of *Il21* in T cells and *Il2rb* in B cells with age, together with a linear regression line.

(M) Left, dot plot summarizing the enriched cytokine signatures using aging-up peak sets of B cells from each tissue. Only signatures that can be supported by increased accessibilities of secretion or receptor genes are shown. Right: barplot summarizing the number of tissues with activated signatures for each cytokine, splitting males and females.

Discussion

Aging involves global deterioration in cellular and organismal function. While advancements in genomics techniques, especially single-cell RNA-seq and spatial transcriptomics, have been used to explore age-associated changes in cell-type- and region-specific gene expression (*15*, *57*, *84*, *85*), few studies have systematically investigated cell population shifts, chromatin dynamics, as well as age-sex interaction on the scale of the entire organism. Here, by profiling around seven million cells from 21 mouse tissues at three ages and in both sexes, we constructed a single-cell chromatin accessibility atlas of aging with unprecedented depth and breadth. We reported the aging-associated dynamics of 536 tissue-level main cell types and 1,828 finer-grained subtypes, each defined by the accessibility at approximately 1.3 million cis-regulatory elements. Our findings reveal widespread cell population shifts, lineage-specific epigenomic reprogramming, and striking sex-dependent patterns, laying a foundation for understanding the regulatory logic of mammalian aging.

A key insight of our study is the extensive cell population dynamics accompanying age. Notably, 146 organ-specific cell types (approximately 25% of all organ-specific cell types) changed significantly with age. Many of these are immune cells. For example, we observed a widespread increase in plasma cells and macrophages across various tissues, aligning with previous findings of immunoglobulin accumulation (*85*) and monocyte/macrophage propagation (*86*) in aging. Tissue-specific population changes, such as the expansion of neutrophils in the liver and lung, and depletion of lymphoid progenitors in primary immune organs (e.g., pre-/pro-B cells in the bone marrow and immature T cells in the thymus) were identified. Beyond immune-related changes, our study also reveals additional vulnerabilities in non-immune cell lineages. For example, we observed profound depletion of specialized functional cell types across multiple organs, such as kidney podocytes, muscle tenocytes and satellite cells, ovary granulosa cells, and lung aerocytes. These depletions likely contribute to age-related loss of tissue homeostasis and functions.

Beyond shifts in broad cell types, our high-resolution analysis identified 1,828 subtypes—nearly one-third of which show significant aging dynamics. We identified subtypes exhibiting cell state changes that diverge from their parent population. For example, naive T cell subtypes in the lung and liver sharply decline, although total T cell proportions rise with age. Likewise, we detected region-specific vulnerability of endothelial cells in the kidney medulla and vein, distinct expansions in fibroblast and mast cell subpopulations in the intestine, and the emergence of a shared reactive state (*Creb5*+ *Bnc2*+ *Runx1*+) across different epithelial cell types in the kidney. These findings suggest that aging promotes a variety of cell-state transitions, including those localized to particular anatomical niches or widespread across distinct parent cell types potentially triggered by common circulating factors.

Coordinated expansion or depletion of the same subtype in multiple organs underscores a broader organism-level program. Immune subtypes, in particular, display strikingly synchronous changes, such as the global expansion of *Gzmk*+ CD8 T cells, regulatory T cells, *Il21*+ CD4 T cells, *Il23r*+ innate T cells and *Tbx21*+ B cells. Certain changes were restricted to a few organs, including the depletion of *Zfp683*+ tissue-resident memory T cells in adipose and gut tissues, or the decline of *Gzma*+ resting NK cells in spleen and bone marrow. However, this synchronization extends beyond mobile immune lineages: certain endothelial and fibroblast populations, also show parallel shifts across distinct tissues, such as the depletion of *Slc7a14*+ *Lhx6*+ *Meox2*+ vein endothelial cell and the expansion of an *Ifi207*+ *Ear1*+ aging-associated fibroblast subtype. This points to systemic inflammatory signals or hormonal cues that modulate cell fates body-wide.

At the molecular level, we identified extensive chromatin reprogramming associated with aging. Our differential accessibility analyses uncovered 279,401 peaks changing with age, including a subset consistently altered across many cell types (e.g., promoter peaks of *Nr3c2* and *Il7* that frequently gain accessibility, and *Sox4* or *Sox11* peaks that frequently lose accessibility). Linking chromatin changes to RNA-seq data validated the effects from accessibilities to expressions and revealed putative enhancers regulating aging-associated genes. Motif analysis further supports a shift from TFs involved in tissue maintenance or stemness (*e.g., SOX, E2A*) to those mediating inflammatory and stress responses (*e.g., NF-κB, IRFs, AP-1*). Specifically, as an example to showcase the potential of our data to reveal anti-aging targets, we focused on cytokines and identified the activation of IL15, IL21, IL4, and IFNγ signatures in aged B cells, indicating these extrinsic signals may reinforce or drive the cell-state transitions observed in aging.

Crucially, we found extensive sexual dimorphism. Around forty percent of aging-associated main cell types (55 out of 146) and subtypes (193 out of 499) exhibited sex differences. Notable examples include the male-biased expansion of hepatic stellate cells in the liver and the female-biased expansion of interstitial macrophages in the lung. Overall, female mice appeared to mount a more pronounced immune activation in aging at both proportional and molecular levels, consistent with the higher incidence of autoimmune diseases in women (*87*, *88*). This included female-specific upregulation of TFs like *Pou2f2* in B cells, aligning with female-biased expansions of aging-associated B cell subtypes. We also observed subtypes that shift in opposite directions by sex, such as *Slc22a7*+ proximal tubule cells (PT S3T2) increasing in aged females but decreasing in males—trends replicated by single-cell transcriptomic data. At the epigenetic level, we detected tens of thousands of cell-type-specific peaks that changed exclusively in one sex, highlighting sex as a major axis of aging heterogeneity.

In summary, this organism-level single-cell chromatin accessibility atlas illuminates how aging remodels the cellular composition and regulatory landscape of multiple tissues. Although many changes are highly tissue-specific, we uncovered “coordinated” cellular and molecular dynamics that are shared across different organs, including immune remodeling, broad depletion of functional cell types, the emergence of inflammation-related states, and sex-dependent trajectories. By cataloging these changes, we offer a resource for understanding the molecular logic of aging and for guiding therapeutic strategies aimed at preserving or restoring youthful tissue states. This work also highlights molecular candidates to mitigate aging-related dysfunction by targeting broad-spectral cell types across tissues, including intrinsic transcription factors, extrinsic cytokines, and individual receptors (*Nr3c2* for immune cells, *Epha3* for T cells, *Il2rb* for B cells). Looking forward, we anticipate that this atlas will serve as a critical reference for evaluating anti-aging interventions and refining our understanding of how chromatin remodeling, cell state transitions, and tissue physiology intersect in the aging mammalian body.

Acknowledgments
We thank members of the Cao lab for helpful discussions and feedback. We also thank members of the Rockefeller University High-Performance Computing Core, Comparative Bioscience Center, Genomics Resource Center, Bioinformatics Resource Center and Flow Cytometry Resource Center for their invaluable support.

Funding: This work was funded by grants from NIH (DP2HG012522, R01AG076932, and RM1HG011014 to J.C.), the Sagol Network GerOmic Award and Hevolution/AFAR New Investigator Awards in Aging Biology for J.C.. W.Z. was funded by the SNF RU Institute for Global Infectious Disease Research and Kellen Women's Entrepreneurship Fund. The project was supported by a Longevity Impetus Grant from Norn Group.

Author contributions: J.C. and W.Z. conceptualized and supervised the project; Z.L. optimized nuclei extraction methods and EasySci-ATAC protocols; Z.L. performed mouse dissection, nuclei extraction, and single-cell ATAC-seq experiment; Z.L. performed all computational analyses with insights from Z.X, Z.Z, and A.A.; J.C., W.Z., and Z.L. wrote the manuscript with input from all co-authors.

Competing interests: J.C., W.Z., and Z.L. are inventors on a patent application (U.S. 63/377,061) submitted by Rockefeller University that covers the methods for *EasySci* development.

Data availability: Raw FASTQ files, processed count matrices, cell metadata, and peak metadata can be downloaded from NCBI GEO under accession number GSE288730 (reviewer's token: exitcckgbfmzpkl). An interactive website facilitating the visualization of our data across cell type, age, and sex is available at https://mouseagingatacatlas.org.

Code availability: Custom code and scripts used for processing sequencing reads of EasySci-ATAC-seq library were deposited in Zenodo (*89*) (https://doi.org/10.5281/zenodo.8395492) .

Supplementary Materials

Materials and Methods:

Animals and organ collection

The C57BL/6 wild-type mice at one month (n=10, 5 males and 5 females), five months (n=10, 5 males and 5 females), and twenty-one months (n=12, 6 males and 6 females) were obtained from The Jackson Laboratory. Detailed information on animal individuals in this study is provided in Table S1A. Mice were housed socially and maintained on a regular 12h/12h day/night cycle. In order to analyze newborn cells from the same set of samples in parallel, all mice were labeled with EdU (25 mg/kg, i.p. injection) at 24-hour intervals for five days. Tissues were harvested one day after the final injection. To control for circadian effects, sample harvest was performed around the same period (4-7 PM) across all individuals. Mice were euthanized utilizing inhalation of carbon dioxide (CO2). After euthanization, major organs were quickly transferred into ice-cold PBS, and the following tissues were collected: brown adipose tissue, bone marrow, cecum, colon, esophagus, eye, heart, small intestine (spanning duodenum, jejunum, and ileum), kidney, liver, lung, muscle (quadriceps and gastrocnemius), ovary and uterus, pancreas, back skin, spleen, stomach, thymus, gonadal white adipose tissue, inguinal white adipose tissue, mesenteric adipose tissue. Dissected mouse tissues were snap-frozen in liquid nitrogen and stored at -80C. All animal procedures were in accordance with institutional regulations under the IACUC protocol 21049.

Nuclei extraction from multiple mammalian organs

Nuclei extraction was performed using the method from (*90*) and (*7*) with slight modifications. Before extraction, frozen tissues were placed inside aluminum foil, and smashed into powders on dry ice with a hammer. 10X PBS-hypotonic stock solution was prepared as follows: 6.83 g of Na_2HPO_4-$2H_2O$ (Sigma, 71643-250G), 3.5 g of NaH_2PO_4-H_2O (CATALOG), 1.2 g of KH_2PO_4 (Sigma, P285-500), 1 g of KCl (Sigma, P9541-1KG) and 3 g of NaCl (Sigma, P9888-500G) in nuclease-free water to a final volume of 500 mL. On the day of nuclei extraction, 1X nuclei lysis buffer was prepared freshly as follows: final concentration of 1X PBS-hypotonic stock solution, 3 mM $MgCl_2$ (VWR, 97062-848), 0.025% IGEPAL CA-630 (VWR, IC0219859650), 0.1% Tween-20 (Sigma, P9416-100ML), 1X cOmplete, EDTA-free Protease Inhibitor Cocktail (Sigma, 11873580001). In addition, a final concentration of 0.33M sucrose (Sigma, S0389) was included in the lysis buffer for these tissues: esophagus, stomach, intestinal, cecum, colon, spleen, thymus, bone marrow and skin. The powdered tissues were then transferred into 10-20 mL nuclei lysis buffer, followed by brief vortexing and incubation for 10-15 minutes at 4C on a rotator. Extracted nuclei were then filtered through 40 um cell strainers (VWR, 470236-276), stained with 4',6-diamidino-2-phenylindole staining (DAPI, Invitrogen D1306), and FACS sorted for singlets.

EasySci library construction and sequencing

The EasySci-ATAC library was prepared following the prior study (*15*), except for a few modifications. The sorted nuclei were pelleted down at 500g for 5 minutes, resuspend in nuclei buffer [10 mM Tris-HCl pH 7.5 (VWR, 97062-936), 10 mM NaCl (VWR, 97062-858), 3 mM $MgCl_2$ (VWR, 97062-848), 0.025% IGEPAL CA-630 (VWR, IC0219859650), 0.1% Tween-20 (Sigma, P9416-100ML), 1X cOmplete, EDTA-free Protease Inhibitor Cocktail (Sigma, 11873580001)] to a final concentrations of 1000~2000 nuclei/μL. Nuclei were mixed in a 1:1 ratio with 2X TD buffer [20 mM Tris-HCl pH 7.5, 20 mM $MgCl_2$, 20% Dimethylformamide (Fisher, AC327175000)] and dispensed 10 μL into each well of four 96-well plates. 1 μL barcoded Tn5 was

loaded into each well. Tagmentation reaction was performed at 37°C for 30 minutes with gentle shaking at 300 rpm and stopped by adding 11 µL of 2X Stop buffer [40 mM EDTA (VWR, 37062-656), 1 mM Spermidine (Sigma, S0266-1G)] to each well. Samples were pooled and washed twice and resuspended resuspended in nuclei buffer. 5 µL of resuspended nuclei were distributed into each well of 96-well plates. 2 µL indexed EasySci P5 ligation adapters and 3 µL ligation mix [1 µL nuclease-free water, 1 µL 10X T4 DNA ligase buffer, 1 µL T4 DNA ligase (NEB, M0202L)] were added to each well. Ligation was performed at room temperature for 30 minutes with medium-speed rocking (350g) and stopped by adding 2 µL of 18 mM EDTA to each well. After that, nuclei were pooled, washed, resuspended using nuclei buffer, and subjected to another round of FAC sort based on DAPI staining to remove doublets. Then, sorted nuclei were distributed into PCR plates as 5 uL per well. Proteinase K treatment was performed by mixing each well with 0.25 µL 18.9 mg/mL proteinase K (Sigma, 3115828001), 0.25 µL 1% SDS, and 0.5 µL EB buffer, and plates were incubated at 65°C for 16 hours. Then, 2 µL 10% Tween-20 was added to each well to quench the SDS. Following on, 1 µL of 10 µM universal P5 primer (5′-AATGATACGGCGACCACCGAGATCTACAC-3′, IDT), 1 µL of 10 µM indexed P7 primer (5'-CAAGCAGAAGACGGCATACGAGAT[i7]GTGACTGGAGTTCAGACGTGTGCTCTTCCGATCT-3', IDT) and 10 µL NEBNext High-Fidelity 2X PCR Master Mix (NEB M0541L) were added into each well. Amplification was carried out using the following program: 72°C for 5 minutes, 98°C for 30 seconds, 13-14 cycles of 98°C for 10 seconds, 66°C for 30 seconds, 72°C for 30 seconds and a final 72°C for 5 minutes. Final PCR products were pooled and purified by column purification using a Zymo DNA Clean & Concentrator kit (Zymoresearch, D4014) followed by gel extraction using Zymoclean Gel DNA Recovery Kit (Zymoresearch, D4007) to remove adapter dimers. Library concentrations were determined by Qubit and the libraries were visualized by electrophoresis on a 2% E-Gel™ EX Agarose Gels (Invitrogen G402022).

Processing of sequencing reads

Base calls were converted to fastq format and demultiplexed using Illumina's bcl2fastq/v2.19.0.316 tolerating one mismatched base in barcodes (edit distance (ED) <= 1). Then, indexed Tn5 barcodes and ligation barcodes were extracted, and corrected to their nearest barcode (edit distance (ED) <= 1). Reads with uncorrected barcodes (ED >= 2) were removed. Tn5 adaptors were removed from 5'-end and clipped from 3'-end using trim_galore/0.4.1 (https://github.com/FelixKrueger/TrimGalore). Trimmed reads were mapped to the mouse genome (mm10) using STAR/v2.5.2b with default settings. Aligned reads were filtered using samtools/v1.4.1 to retain reads mapped in proper pairs with quality score MAPQ > 30 and to keep only the primary alignment. Duplicates were removed by picard MarkDuplicates/v2.25.2 per PCR sample. Deduplicated bam files were converted to bedpe format using bedtools/v2.30.0, which were further converted to offset-adjusted (+4 bp for plus strand and -5 bp for minus) fragment files (.bed). Deduplicated reads were further split into constituent cellular indices using the Tn5 and ligation barcodes, and sparse matrices counting reads overlapping with promoter regions (±1 kb around transcription start site) were generated for quality filtering. In the meantime, fragment files were used to generate h5ad files for all downstream analyses with the snap.pp.import_data() function of SnapATAC2/v2.5.1. Cell-by-bin matrices were also generated with SnapATAC2 function snap.pp.add_tile_matrix() containing insertion counts across genome-wide 5000-bp bins.

Cell filtering, dimensionality reduction, clustering, and annotations

The following analyses were performed on the dataset of each tissue separately. After initial processing, cells with less than 1000 unique reads or less than 15% of reads in promoter regions were discarded. The

promoter ratio cutoff was adjusted to 0.1 for the eye dataset due to the observation of a lower promoter ratio in corneal epithelial cells. Then, we used an iterative clustering strategy to detect potential doublet cells from each organ, similar to our previous study (*15*, *91*). Briefly, doublet scores were calculated for each cell using SnapATAC2 function snap.pp.scrublet(). Meanwhile, all cells of each organ were subjected to clustering and sub-clustering analysis with spectral embedding and graph-based clustering implemented in SnapATAC2. Cells labeled as doublets (defined by a doublet probability cutoff of 0.5) or from doublet-derived sub-clusters (defined by a doublet ratio cutoff of 0.2) were manually examined and filtered out. We then generated gene activity matrices for each organ by counting the Tn5 insertions in the TSS and gene body regions for each gene using SnapATAC2 function snap.pp.make_gene_matrix(). Gene activity matrices were then used for cell type annotations.

To identify clusters of cells corresponding to different cell types, we subjected cells after data cleaning to dimension reduction and Leiden clustering using SnapATAC2 functions snap.tl.spectral(), snap.pp.knn() and snap.tl.leiden() with the default setting. UMAP coordinates were calculated based on the spectral embedding matrices using the function UMAP() with min_dist=0.01 from the Python package umap/v0.5.2 (*92*). For cell annotations, we first obtained a draft of annotations by integrating our chromatin data (subsampled to 2,000 cells per Leiden cluster) with the published sn-RNA-seq datasets (*7*) through Seurat/4.3.0.1 (*7*, *93*) label transfer, and we manually reviewed and refined the annotations for each Leiden cluster based on accessibilities of known markers listed in Table S2.

Peak calling

After cell annotation, reads from each main cell type of each tissue were concatenated. Then, Tn5-corrected single-base insertions were extracted and subjected to peak calling using macs3/v3.0.0b3 (*94*), with the following parameters: --nomodel --extsize 200 --shift -100 -q 0.1. Peak summits were extended by 250bp on either side and then merged iteratively, similar to (*12*). Specifically, the peak with the smallest p-value was kept and any peak that directly overlapped with it was removed. Then, this process was repeated to the second most significant peak and so on until all peaks were either kept or removed. Interactive merging was performed first across main cell types within each tissue, and then across all tissues to generate the universal peak set across the entire organism. The peak count matrices were generated using the SnapATAC2 function snap.pp.make_peak_matrix(). Peak annotations were performed using the HOMER function annotatePeaks.pl.

Identifications of cell-type-specific peaks

We used a Shannon entropy-based method to identify cell type-specific peaks, similar to previous studies (*12*, *95*). Starting from 144 unique cell types collapsed from all tissues, we first aggregated the peak count matrix for each cell type and normalized the aggregated matrix to counts per million (CPM). We then converted the CPM values into probabilities by dividing each cell type's CPM by the total CPM across all cell types for a given peak: $p_i = q_i / \Sigma q_i$, where "q_i" is the CPM value of the i-th cell type of a given peak. Next, we calculated Shannon entropy for each peak, which measures how uniformly accessibility is distributed across cell types: $H = - \Sigma (p_i * \log(p_i))$ where "p_i" is the probability of the i-th cell type for a given peak. To determine statistical significance, we generated a background distribution of entropy values using a set of peaks with low variability. Specifically, for each peak, we calculated the fold change between the most accessible cell type (quantified by CPM) and the average accessibility across all cell types. We then grouped peaks based on their mean accessibility into thirty bins. Within each bin, peaks with fold-change values below the 25th percentile were considered low-variable peaks, while those in the top 25th

percentile were considered high-variable peaks. The entropy threshold was set at a p-value of 0.05, using the low-variability peaks as the background. Cell type-specific peaks were identified from the high-variable peak set if their entropy values fell below this threshold. Cell-type-specific peaks, along with their maximum and average accessibility values quantified by CPM, can be found in Table S3.

LDSC analysis

To estimate enrichments of heritability for human traits in cell-type-specific peaks, we applied LDSC (*96*), which takes summary statistics from a given GWAS as input and quantifies the enrichment of heritability in an annotated set of SNPs conditioned on a baseline model that accounts for the non-random distribution of heritability across the genome. The LDSC computational pipeline was modified from (*97*) and the LDSC tutorial (https://github.com/bulik/ldsc/wiki/Cell-type-specific-analyses). Specifically, we first used the UCSC utility liftOver to lift all GWAS SNPs from the human to the mouse genome. We then took the top 2000 differentially accessible peaks per main cell type identified from the entropy-based method, and annotated each SNP according to whether or not it overlapped these cell-type-specific peaks. We then followed the recommended workflow for running LDSC using HapMap SNPs, precomputed files corresponding to 1000 genomes phase 3, excluding the MHC region to generate an LDSC model for each chromosome and peak set. GWAS summary statistics were obtained from the Broad LD Hub (https://data.broadinstitute.org/alkesgroup/sumstats_formatted/) and from GWAS catalogs (*98*) (https://www.ebi.ac.uk/gwas/downloads/summary-statistics). Coefficient P values calculated from LDSC were corrected for multiple hypotheses for each trait using the Benjamini-Hochberg method.

Identifications of sex dimorphism for main cell types

To examine cell types with sex dimorphism in chromatin accessibility profiles, we trained k-nearest neighbor (KNN) classifiers to distinguish male and female cells of the same age for each main cell type using python package sklearn/v1.0.2. Spectral embeddings generated from SnapATAC2 were used as input features to predict the sex of individual cells. Datasets were filtered to include only cell types with at least 200 total cells and a minimum of 50 cells per sex. We performed five independent train-test splits, using 80% of the data for training and 20% for testing, with stratified sampling to maintain sex balance. To ensure computational efficiency, we subsampled both training and test sets to a maximum of 2000 cells per cell type. Classification performance was evaluated using area under the curve (AUC) metrics, with cell types exhibiting AUC > 0.9 considered to display strong sex-associated chromatin differences.

Sub-clustering analysis

Sub-clustering analysis was performed using SnapATAC2, same as main clustering. Briefly, we subjected cells of the same type within the same tissue to feature selection (n_features=50000), dimension reduction and leiden clustering (resolution=1.5). UMAP coordinates were calculated based on the spectral embedding matrices (min_dist=0.01). We then examined the resulting Leiden clusters and manually merged those that overlapped in UMAP space without clear differences in gene accessibility. For certain cell types with pronounced sex dimorphism, including liver hepatocytes, kidney proximal tubule cells, type IIB myonuclei in muscle, adipocytes, and adipose stem and progenitor cells from gonadal white adipose tissue, sub-clustering was performed separately for males and females to capture cell-state differences rather than sex-based differences.

Differential Abundance Analysis

For each mouse individual, we quantified the proportion of each main cell type or subtype within each tissue, and applied a linear regression model (proportion ~ age + age:sex) to assess age-associated population dynamics while accounting for sex effects. The analysis was conducted using the R function lm(). Quadriceps and gastrocnemius muscles were analyzed separately, as they were from distinct anatomical locations. In the model, age was treated as a continuous variable (in months), while sex was considered a binary categorical variable. To identify significantly changing subtypes, we filtered results based on the following criteria: $R^2 > 0.4$ and a q-value (for either the age term or the age:sex interaction term) < 0.05. Multiple hypothesis correction was performed separately for each tissue using the Benjamini-Hochberg method. Additionally, Pearson correlation coefficients were calculated between the proportion of each main cell type or subtype and age. Based on these correlations, cell types and subtypes were classified into three groups: aging-up (q-value of the age term < 0.05, q-value of the age:sex interaction > 0.05, Pearson r > 0), aging-down (q-value of the age term < 0.05, q-value of the age:sex interaction > 0.05, Pearson r < 0), interaction-significant (q-value of the age:sex interaction < 0.05).

Differential Peak Analysis

In order to reduce the search space for differential peak analysis, we first selected highly accessible and highly variable peaks for each main cell type. First, the accessibility levels of all 1.3M peaks for each condition were quantified by counts per million (CPM) after aggregating data of the same age. Peaks were then ranked based on their CPM value in the most accessible condition, and only those above the 75th percentile were retained for each main cell type. These highly accessible peaks were further grouped into thirty bins based on their maximum accessibility. Within each bin, peaks with fold-change values (max condition vs. mean of three age groups) in the top 25th percentile were classified as highly variable peaks. This preselection was conducted separately for males and females, and the resulting peaks were collapsed across sexes.

Pre-filtered peaks for each main cell type were then analyzed for differential accessibility using edgeR/v3.36.0 (*12*, *77*). The analysis was performed at the pseudo-bulk level by aggregating single-cell peak counts from the same mouse sample, treating each individual mouse as a replicate. Age was treated as a continuous variable (in months). Only cell types with more than 200 cells in all three age groups were included in the analysis. Additionally, male and female samples were tested separately, with log fold-change (logFC), p-values, and q-values computed for each sex independently using edgeR. Differentially accessible peaks were categorized as follows: sex-shared, aging up-regulated peaks (p-value-female < 0.05 and p-value-male < 0.05, q-value-male < 0.05 or q-value-male < 0.05, logFC-female > 0, logFC-male > 0); sex-shared, aging down-regulated peaks (p-value-female < 0.05 and p-value-male < 0.05, q-value-male < 0.05 or q-value-male < 0.05, logFC-female < 0, logFC-male < 0); female-specific DA peaks (p-value-male > 0.05, q-value-female < 0.05); male-specific DA peaks (p-value-female > 0.05, q-value-male < 0.05).

Identifying aging-associated linkages of genes, promoters and cis-regulatory elements

This analysis aims to identify links between cis-regulatory elements and their putative target genes, and to validate accessibility changes with gene expression data. First, we focused on aging-associated differentially accessible (DA) peaks identified previously. Pearson correlation coefficients were computed between DA promoters and nearby non-promoter DA peaks (±500 kb) across samples, after pseudo-bulking each mouse individual. A background distribution was also generated by pairing DA promoters

with randomly selected peaks, and a threshold of Pearson correlation was defined with an empirical FDR = 0.05. The correlation analyses were performed separately for sex-shared, female-specific and male-specific peaks. In the meantime, we collected snRNA-seq data of mouse aging from (*7*), re-annotated the cells for consistent cell type labels between RNA-seq and ATAC-seq, and followed with differential gene expression changes using edgeR/v3.36.0 (*77*). Similar to differential accessible analysis, the differential expression analysis was performed separately for males and females in terms of each main cell type in each tissue, and at the pseudo-bulk level by aggregating single-cell gene counts from the same mouse individual. Differentially expressed genes, including sex-shared (p-value < 0.1 in both males and females, with the same logFC direction), female-specific (p-value < 0.1 in females but > 0.1 in males) and male-specific changes (p-value < 0.1 in males but > 0.1 in females) were defined. Finally, aging-associated linkages (gene-promoter-CRE) were defined if a gene exhibited consistent changes (up-regulated or down-regulated) in the same cell type from the same tissue across three layers, i.e, expression changes based on RNA-seq data, accessibility changes of promoters and non-promoter peaks based on ATAC-seq data, significant correlations between accessibilities of promoters and linked non-promoter sites.

Transcription factor motif analysis

We used Signac/v1.7.0 (*99*) and chromVAR/v1.16.0 (*21*) to quantify motif accessibility of transcription factors in Figure 3N, 5C, 5I, S3E, S3F and S7B. Position weight matrices of transcription factor binding sites were obtained from JASPAR2022 (*100*). A Signac object containing a peak count matrix of cells of interest was constructed using the Signac functions CreateChromatinAssay() and CreateSeuratObject(). Motif information was then added via AddMotifs(), and motif deviation scores were calculated for each single cell using RunChromVAR(). In Figure S3F, to compare motif activity and gene accessibility of transcription factors across cell types, motif deviation scores were rescaled to the range (0,10) using the R function rescale(), averaged per cell type, and scaled to z-score across cell types. In Figure 5C, motif footprinting analysis was performed using the Footprint() function in Signac.

For motif enrichment analysis of aging-associated differentially accessible (DA) peaks (Figure 7A, 7C, 7D, and 7E), we used the HOMER function findMotifsGenome.pl (*73*). A background peak set with minimal age-related changes was selected for each main cell type as a control for HOMER analysis. Specifically, accessible peaks for each cell type were grouped into thirty bins, based on accessibility in the highest condition. Within each bin, peaks with fold-change values (maximum condition vs. the mean of three age groups) in the bottom 10th percentile were classified as invariable peaks. The same background peak set was used to assess transcription factor motif enrichment across all aging-associated peak sets of a given cell type. Motif enrichments were quantified as the percentage of peaks containing a given motif in the target peak set relative to the background. Significance values (-log10 q-value) were calculated within HOMER.

Cytokine-related analysis

To evaluate the contribution of cytokine signaling to age-related molecular changes in B cells and macrophages, aging-upregulated DA peaks of each sex identified from chromatin accessibility data were first collapsed to their nearest genes using the HOMER function annotatePeaks.pl. The resulting gene sets (female-upregulated and male-upregulated) were compared to cytokine-induced gene sets of the same cell type from the Immune Dictionary Data (*82*). A hypergeometric test was performed using the R function phyper(). We only kept conditions containing more than ten DE genes after cytokine treatments identified from Immune Dictionary for this comparison.

As an additional measure of aging signatures across cytokine treatments, we overlapped the aging-upregulated gene signatures from our study with the union of genes that exhibited increased expression in at least one cytokine treatment. This overlapping gene set represents shared features between aging and cytokine responses. To identify cytokines that mimic aging phenotypes, we compared the aggregated expression of these genes across cytokine treatments to the PBS control. Statistical evaluation was conducted using Wilcoxon rank-sum tests (wilcox.test() in R).

To minimize cross-activation effects, we excluded cytokines whose receptors were not expressed (TPM < 1) in the target cell type, based on gene expression profiles from the Immune Dictionary. To further validate cytokine signaling changes and refine potential targets, we further analyzed chromatin accessibility changes in genes encoding cytokines and their receptors. Differential analyses were performed using gene accessibility matrices at the pseudo-bulk level, with females and males analyzed separately.

Finally, cytokine signatures were defined based on the following criteria: significant overlap with aging-peak-associated genes (p-value < 0.05, hypergeometric test); significant aging-mimicking activation compared to PBS (p-value < 0.05, Wilcoxon rank-sum test); can be supported by increased chromatin accessibility of the underlying genes in at least one cell type within the same tissue, or from increased chromatin accessibility of receptor genes in the target cell type.

Supplementary figures

Figs. S1 to S10

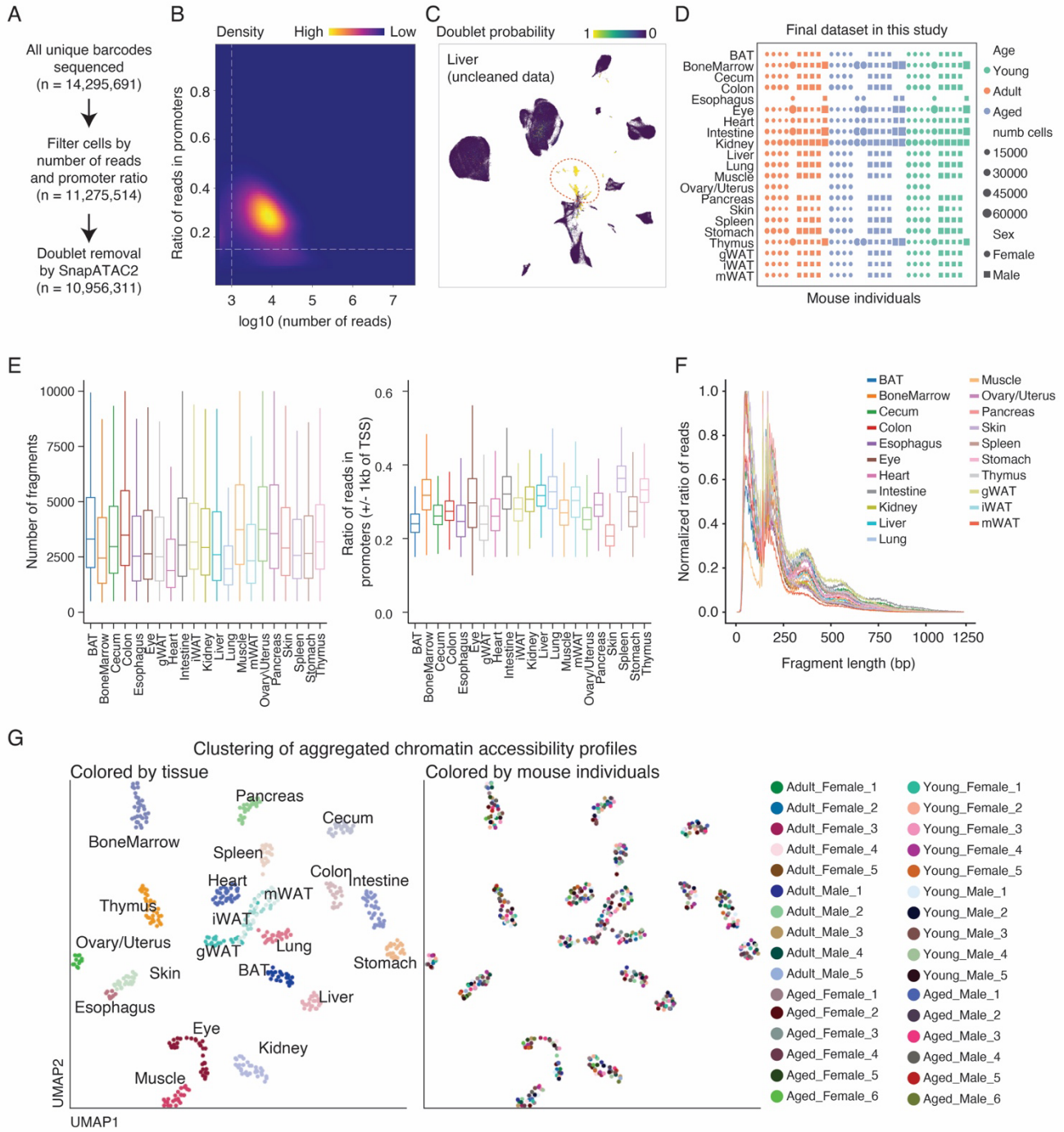
A
All unique barcodes sequenced (n = 14,295,691)
Filter cells by number of reads and promoter ratio (n = 11,275,514)
Doublet removal by SnapATAC2 (n = 10,956,311)
B
Density
High
Low
Ratio of reads in promoters
log10 (number of reads)
C
Doublet probability
Liver (uncleaned data)
D
Final dataset in this study
Mouse individuals
Age
Young
Adult
Aged
numb cells
15000
30000
45000
60000
Sex
Female
Male
E
Number of fragments
Ratio of reads in promoters (+/- 1kb of TSS)
F
Normalized ratio of reads
Fragment length (bp)
G
Clustering of aggregated chromatin accessibility profiles
Colored by tissue
Colored by mouse individuals
UMAP1
UMAP2

Figure S1. Overview of dataset quality.

(A) Scheme of data cleaning procedures. All sequenced cells underwent initial filtering determined by reads number and promoter ratio, followed by doublet removal using a modified pipeline based on SnapATAC2 (*17*).

(B) Density plot showing the distribution of the number of reads per nucleus versus the ratio of reads in promoters. Dash lines indicated cutoffs used for filtering (promoter ratio > 0.15 and > 1,000 unique reads).

(C) An example UMAP plot showing all liver cells (before doublet removal), colored by doublet probability. Circle indicated doublet cells.

(**D**) Dot plot showing the total number of cells obtained from each mouse individual after all quality control filterings.

(E) Box plot showing the number of fragments (left) and the ratio of reads mapped to promoters (± 1kb of TSS, right) per nucleus across tissues.

(**F**) Line plot showing the fragment length distributions of aggregated single cell ATAC-seq data across tissues.

(G) UMAP visualization of the aggregated chromatin accessibility profiles from all samples across tissues, colored by organ (left) and mouse individuals (right).

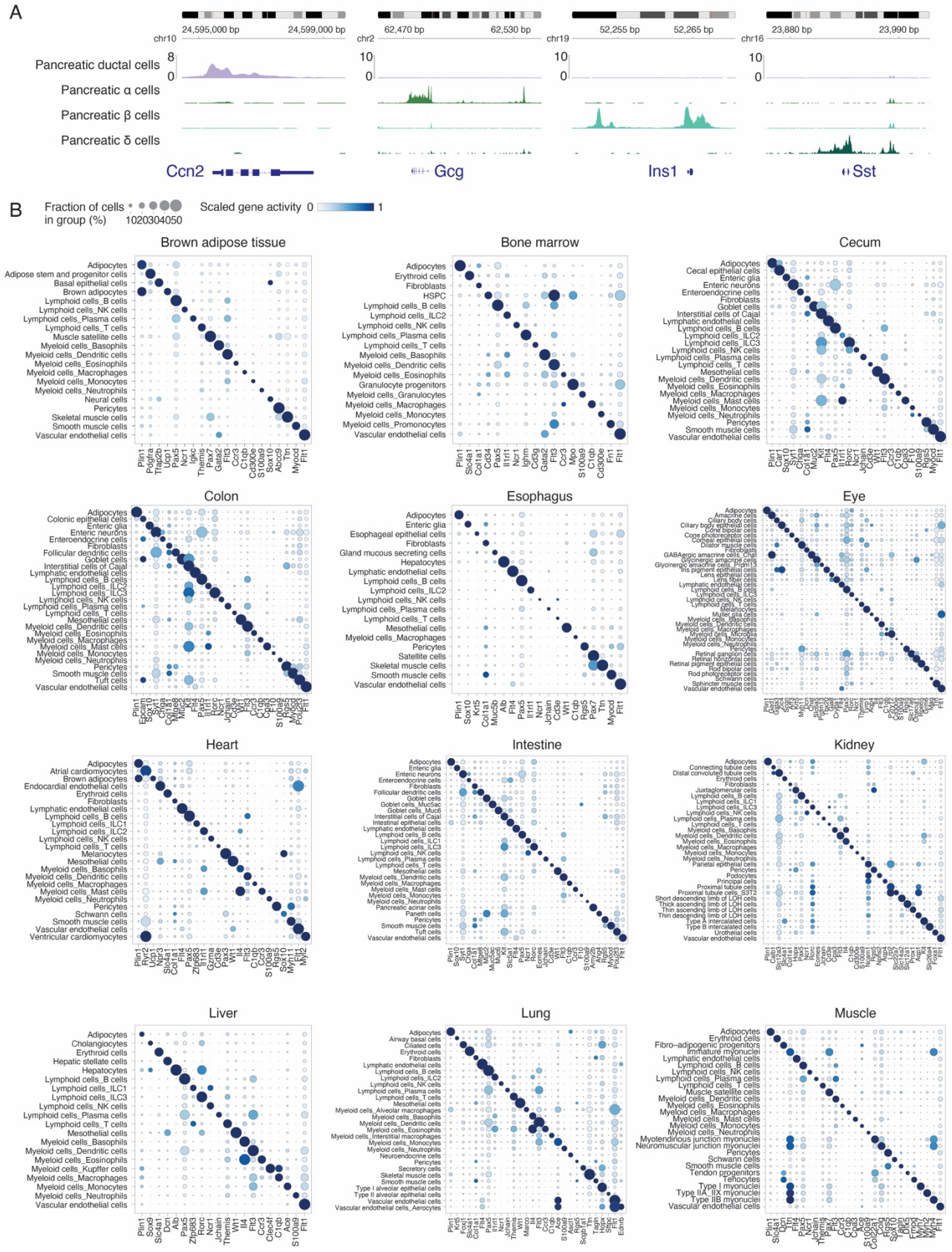
A
chr10
24,595,000 bp
24,599,000 bp
chr2
62,470 bp
62,530 bp
chr19
52,255 bp
52,265 bp
chr16
23,880 bp
23,990 bp
Pancreatic ductal cells
Pancreatic α cells
Pancreatic β cells
Pancreatic δ cells
Ccn2
Gcg
Ins1
Sst
B
Fraction of cells in group (%)
Scaled gene activity
Brown adipose tissue
Bone marrow
Cecum
Colon
Esophagus
Eye
Heart
Intestine
Kidney
Liver
Lung
Muscle

Figure S2. Annotation of main cell types using gene accessibilities.
(A) Genomic tracks showing examples of cell type annotation using accessibilities of marker genes for pancreatic ductal cells (*Ccn2*), alpha cells (*Gcg*), beta cells (*Ins1*), and delta cells (*Sst*).
(B) Dot plots showing gene markers used for annotating main cell types across tissues. The size of the dot encodes the percentage of cells within a cell type in which that marker was detected, and its color encodes the average accessibility level. A complete list of markers can be found in **Table S2**.

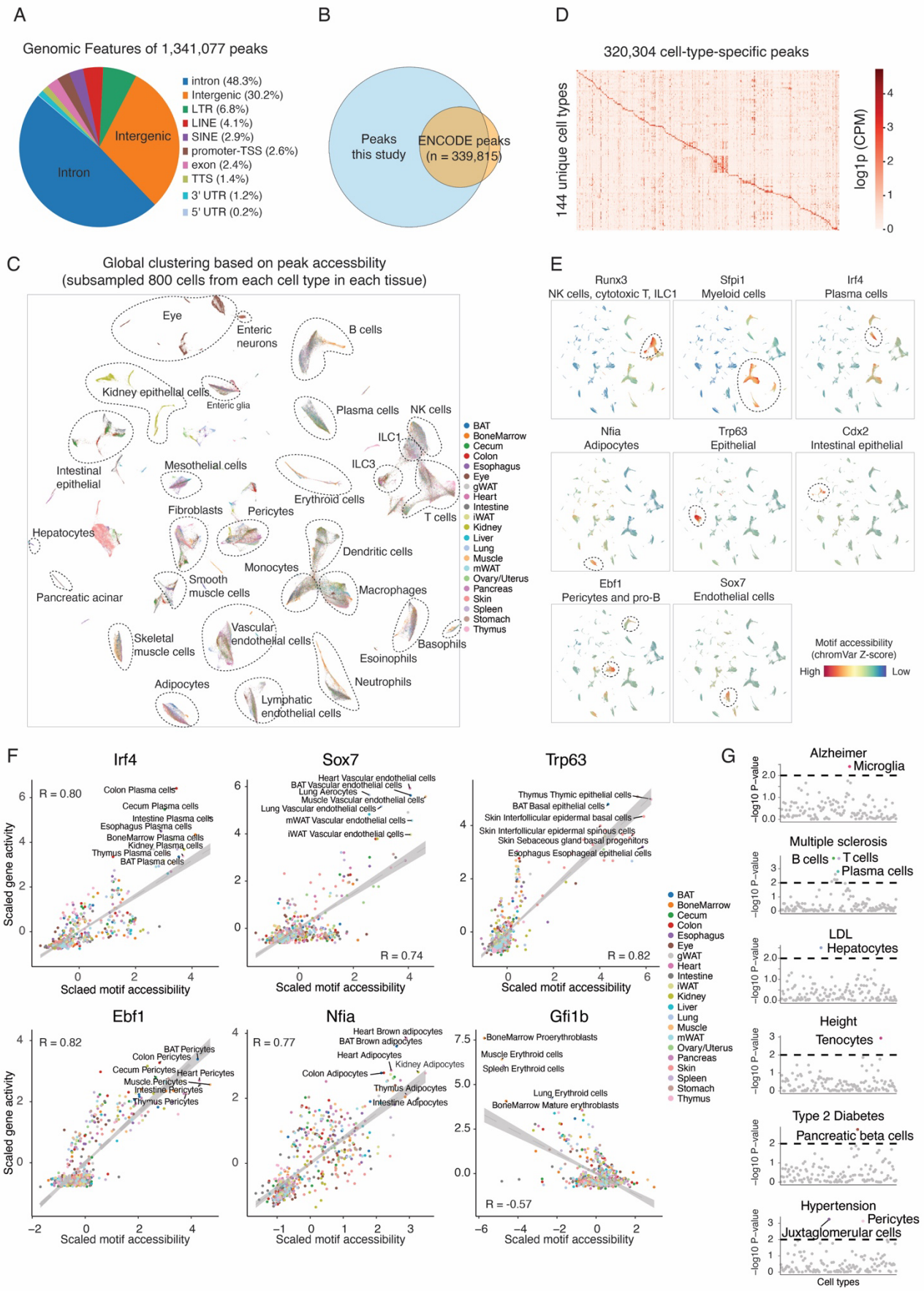
A
Genomic Features of 1,341,077 peaks
Intron
Intergenic
intron (48.3%)
Intergenic (30.2%)
LTR (6.8%)
LINE (4.1%)
SINE (2.9%)
promoter-TSS (2.6%)
exon (2.4%)
TTS (1.4%)
3' UTR (1.2%)
5' UTR (0.2%)
B
Peaks this study
ENCODE peaks (n = 339,815)
D
320,304 cell-type-specific peaks
144 unique cell types
log1p (CPM)
C
Global clustering based on peak accessbility
(subsampled 800 cells from each cell type in each tissue)
Eye
Enteric neurons
B cells
Kidney epithelial cells
Enteric glia
Plasma cells
NK cells
ILC1
ILC3
Intestinal epithelial
Mesothelial cells
Erythroid cells
Fibroblasts
Pericytes
T cells
Hepatocytes
Dendritic cells
Monocytes
Smooth muscle cells
Macrophages
Pancreatic acinar
Vascular endothelial cells
Skeletal muscle cells
Basophils
Esoinophils
Neutrophils
Adipocytes
Lymphatic endothelial cells
BAT
BoneMarrow
Cecum
Colon
Esophagus
Eye
gWAT
Heart
Intestine
iWAT
Kidney
Liver
Lung
Muscle
mWAT
Ovary/Uterus
Pancreas
Skin
Spleen
Stomach
Thymus
E
Runx3
NK cells, cytotoxic T, ILC1
Sfpi1
Myeloid cells
Irf4
Plasma cells
Nfia
Adipocytes
Trp63
Epithelial
Cdx2
Intestinal epithelial
Ebf1
Pericytes and pro-B
Sox7
Endothelial cells
Motif accessibility
(chromVar Z-score)
High
Low
F
Irf4
R = 0.80
Colon Plasma cells
Cecum Plasma cells
Intestine Plasma cells
Esophagus Plasma cells
BoneMarrow Plasma cells
Kidney Plasma cells
Thymus Plasma cells
BAT Plasma cells
Scaled gene activity
Sclaed motif accessibility
Sox7
Heart Vascular endothelial cells
BAT Vascular endothelial cells
Lung Aerocytes
Muscle Vascular endothelial cells
Lung Vascular endothelial cells
mWAT Vascular endothelial cells
iWAT Vascular endothelial cells
R = 0.74
Scaled motif accessibility
Trp63
Thymus Thymic epithelial cells
BAT Basal epithelial cells
Skin Interfollicular epidermal basal cells
Skin Interfollicular epidermal spinous cells
Skin Sebaceous gland basal progenitors
Esophagus Esophageal epithelial cells
R = 0.82
Scaled motif accessibility
Ebf1
R = 0.82
BAT Pericytes
Colon Pericytes
Cecum Pericytes
Heart Pericytes
Muscle Pericytes
Intestine Pericytes
Thymus Pericytes
Scaled gene activity
Scaled motif accessibility
Nfia
R = 0.77
Heart Brown adipocytes
BAT Brown adipocytes
Heart Adipocytes
Kidney Adipocytes
Colon Adipocytes
Thymus Adipocytes
Intestine Adipocytes
Scaled motif accessibility
Gfi1b
BoneMarrow Proerythroblasts
Muscle Erythroid cells
Spleen Erythroid cells
Lung Erythroid cells
BoneMarrow Mature erythroblasts
R = -0.57
Scaled motif accessibility
G
Alzheimer
Microglia
Multiple sclerosis
B cells
T cells
Plasma cells
LDL
Hepatocytes
Height
Tenocytes
Type 2 Diabetes
Pancreatic beta cells
Hypertension
Pericytes
Juxtaglomerular cells
−log10 P-value
Cell types

Figure S3. Identifications and characterizations of cell-type-specific cis-regulatory elements (CREs).

(A) Genomic features of 1,341,077 peaks across the mouse genome. Peaks were annotated using HOMER. TSS, transcription start site; TTS, transcription termination site; UTR, untranslated region.

(B) Venn plot showing the overlap between the peak set determined in this study and from the mouse ENCODE registry (*20*).

(C) UMAP visualization of the entire dataset subsampled to a maximum of 800 cells per main cell type per tissue, colored by the tissue type. Dimension reduction was performed using the peak-count matrix. The same cell types from multiple tissues that clustered together were circled.

(D) Heatmap showing the aggregated accessibility of peaks specific to each main cell type, quantified by counts per million.

(E) UMAP plots as in (C), colored by motif accessibilities (quantified by chromVar (*21*)) of the lineage-specific transcription factor.

(F) Scatter plots showing the example TFs whose gene accessibility levels are positively or negatively correlated with motif accessibility across cell types and tissues. Each point indicates a cell type from a specific tissue. Gene accessibilities were quantified as counts per million, and motif activities were quantified by chromVar (*21*).

(G) Scatter plots showing the enrichments of the phenotype-associated SNPs in cell-type-specific peaks. X-axis: 144 unique cell types collapsed across tissues; y-axis: significance of enrichments (-log10 p-value). Top enriched cell types were labeled for each phenotype.

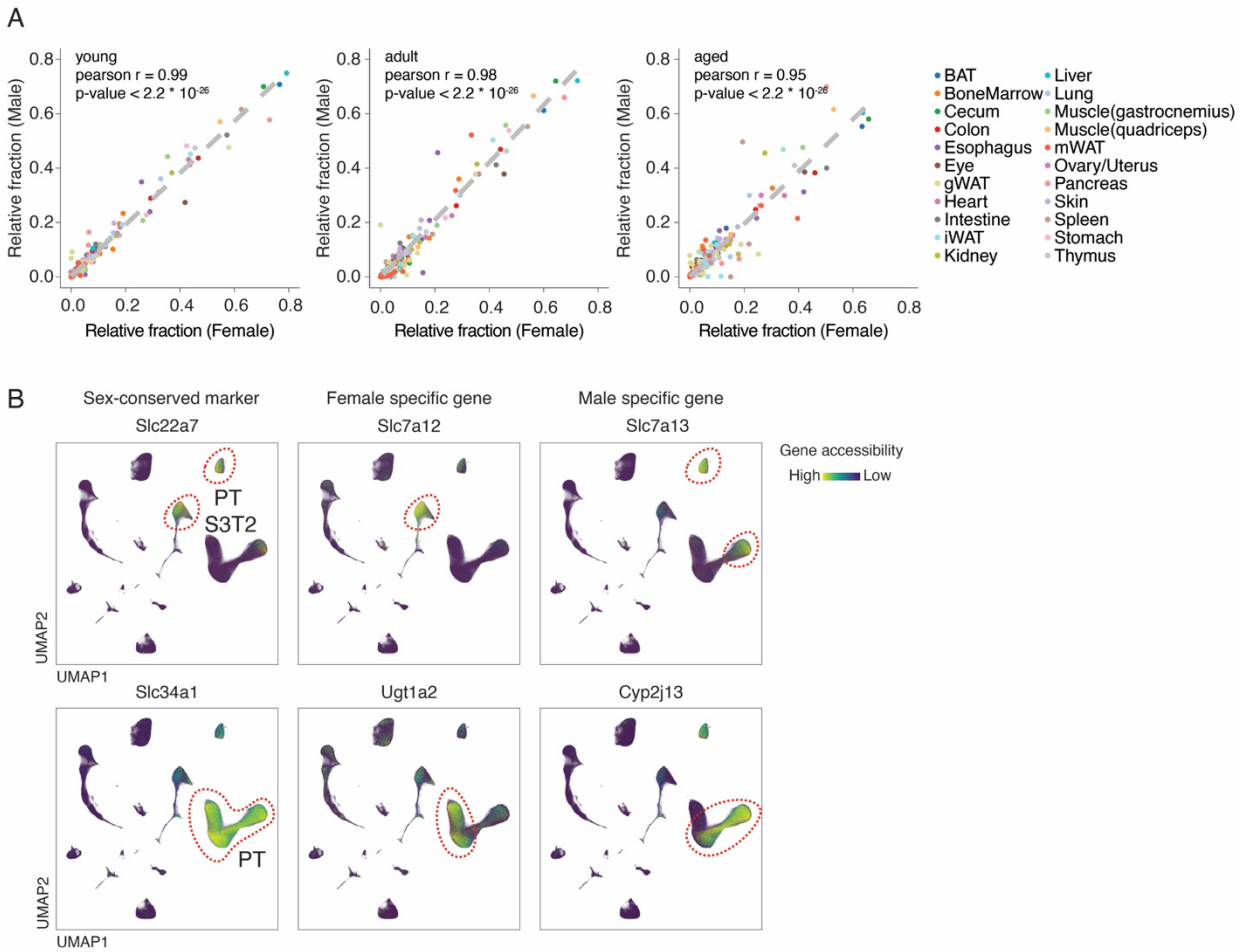

Figure S4. Examinations of sex dimorphism in cell proportion and molecular states.
(**A**) Scatterplot showing the fraction of each main cell type in each tissue between males and females, stratified by age groups. Each dot represents a cell type in a specific tissue.
(**B**) UMAP plots of all kidney cells, colored by accessibility of genes shared between sexes (left; *Slc34a1* for general proximal tubule cells (PT), *Slc22a7* for PT S3T2), unique to females (middle) and males (right).

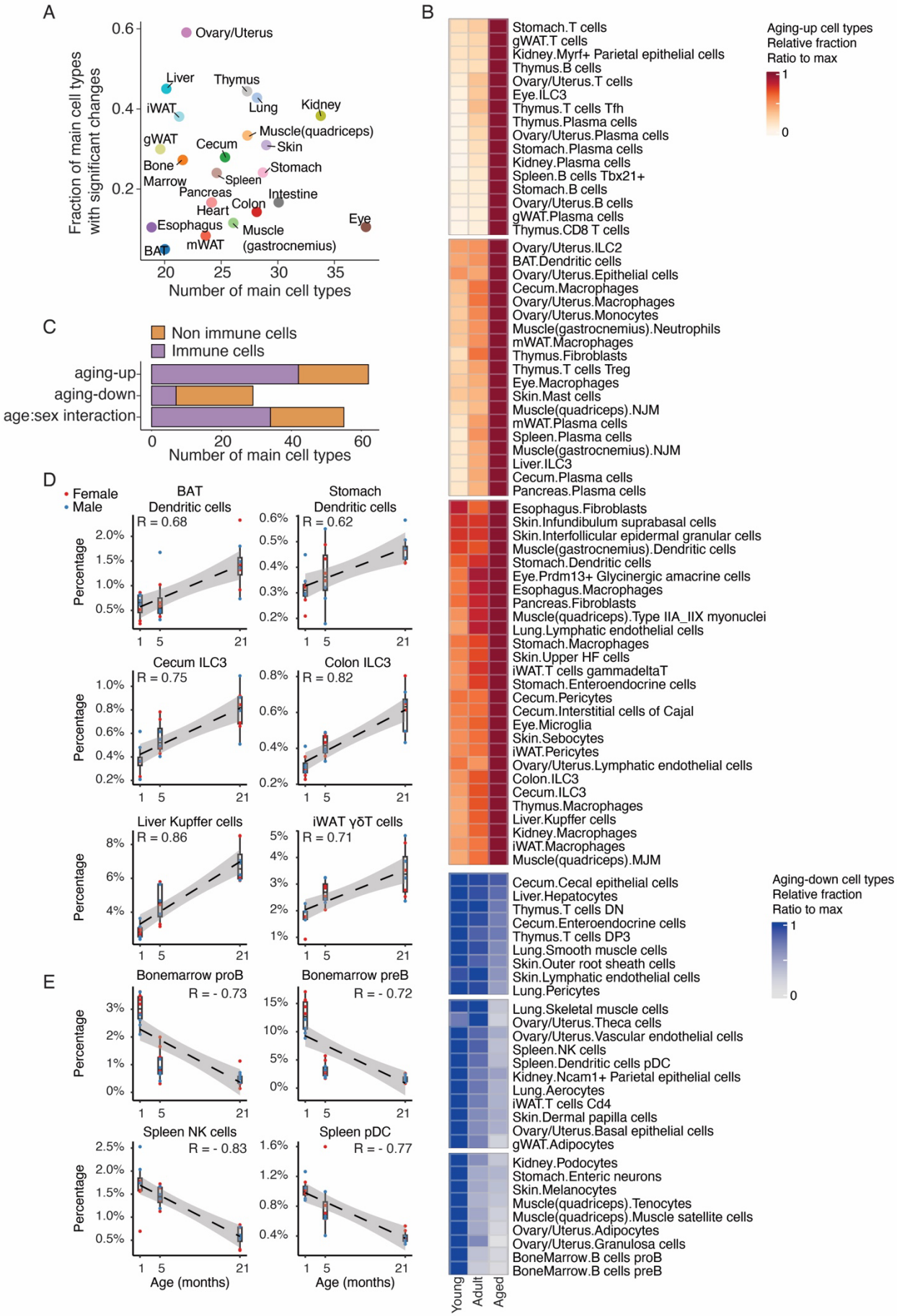
A
Fraction of main cell types with significant changes
Number of main cell types
Ovary/Uterus
Liver
Thymus
iWAT
Lung
Kidney
Muscle(quadriceps)
gWAT
Cecum
Skin
Bone Marrow
Spleen
Stomach
Pancreas
Intestine
Heart
Colon
Eye
Esophagus
Muscle (gastrocnemius)
mWAT
BAT
B
Aging-up cell types
Relative fraction
Ratio to max
Stomach.T cells
gWAT.T cells
Kidney.Myrf+ Parietal epithelial cells
Thymus.B cells
Ovary/Uterus.T cells
Eye.ILC3
Thymus.T cells Tfh
Thymus.Plasma cells
Ovary/Uterus.Plasma cells
Stomach.Plasma cells
Kidney.Plasma cells
Spleen.B cells Tbx21+
Stomach.B cells
Ovary/Uterus.B cells
gWAT.Plasma cells
Thymus.CD8 T cells
Ovary/Uterus.ILC2
BAT.Dendritic cells
Ovary/Uterus.Epithelial cells
Cecum.Macrophages
Ovary/Uterus.Macrophages
Ovary/Uterus.Monocytes
Muscle(gastrocnemius).Neutrophils
mWAT.Macrophages
Thymus.Fibroblasts
Thymus.T cells Treg
Eye.Macrophages
Skin.Mast cells
Muscle(quadriceps).NJM
mWAT.Plasma cells
Spleen.Plasma cells
Muscle(gastrocnemius).NJM
Liver.ILC3
Cecum.Plasma cells
Pancreas.Plasma cells
Esophagus.Fibroblasts
Skin.Infundibulum suprabasal cells
Skin.Interfollicular epidermal granular cells
Muscle(gastrocnemius).Dendritic cells
Stomach.Dendritic cells
Eye.Prdm13+ Glycinergic amacrine cells
Esophagus.Macrophages
Pancreas.Fibroblasts
Muscle(quadriceps).Type IIA_IIX myonuclei
Lung.Lymphatic endothelial cells
Stomach.Macrophages
Skin.Upper HF cells
iWAT.T cells gammadeltaT
Stomach.Enteroendocrine cells
Cecum.Pericytes
Cecum.Interstitial cells of Cajal
Eye.Microglia
Skin.Sebocytes
iWAT.Pericytes
Ovary/Uterus.Lymphatic endothelial cells
Colon.ILC3
Cecum.ILC3
Thymus.Macrophages
Liver.Kupffer cells
Kidney.Macrophages
iWAT.Macrophages
Muscle(quadriceps).MJM
Aging-down cell types
Relative fraction
Ratio to max
Cecum.Cecal epithelial cells
Liver.Hepatocytes
Thymus.T cells DN
Cecum.Enteroendocrine cells
Thymus.T cells DP3
Lung.Smooth muscle cells
Skin.Outer root sheath cells
Skin.Lymphatic endothelial cells
Lung.Pericytes
Lung.Skeletal muscle cells
Ovary/Uterus.Theca cells
Ovary/Uterus.Vascular endothelial cells
Spleen.NK cells
Spleen.Dendritic cells pDC
Kidney.Ncam1+ Parietal epithelial cells
Lung.Aerocytes
iWAT.T cells Cd4
Skin.Dermal papilla cells
Ovary/Uterus.Basal epithelial cells
gWAT.Adipocytes
Kidney.Podocytes
Stomach.Enteric neurons
Skin.Melanocytes
Muscle(quadriceps).Tenocytes
Muscle(quadriceps).Muscle satellite cells
Ovary/Uterus.Adipocytes
Ovary/Uterus.Granulosa cells
BoneMarrow.B cells proB
BoneMarrow.B cells preB
Young
Adult
Aged
C
Non immune cells
Immune cells
aging-up
aging-down
age:sex interaction
Number of main cell types
D
Female
Male
BAT Dendritic cells R = 0.68
Stomach Dendritic cells R = 0.62
Cecum ILC3 R = 0.75
Colon ILC3 R = 0.82
Liver Kupffer cells R = 0.86
iWAT γδT cells R = 0.71
Percentage
E
Bonemarrow proB R = - 0.73
Bonemarrow preB R = - 0.72
Spleen NK cells R = - 0.83
Spleen pDC R = - 0.77
Age (months)

Figure S5. Aging-associated changes in main cell type proportions across tissues.
(A) Scatterplot showing the fraction of main cell types whose proportions changed significantly with age or age-sex interaction in each tissue.
(B) Heatmaps visualizing proportional changes in all aging-associated, sex-independent main cell types. The fraction of each main cell type within its tissue of origin was calculated per sample, averaged within each age group, and normalized to the most abundant condition. Cell types were ordered by hierarchical clustering implemented in ComplexHeatmap (*101*).
(C) Bar plot showing the number of main cell types derived from immune or non-immune cell types within aging-associated, sex-independent (aging-up and aging-down), or age-sex interaction groups.
(D-E) Scatter and box plots showing examples of immune cell types that expand (D) or decline (E) with age, with a linear regression line (and a Pearson correlation coefficient). Each dot represents the cell-type specific proportion of the cell type in each animal.

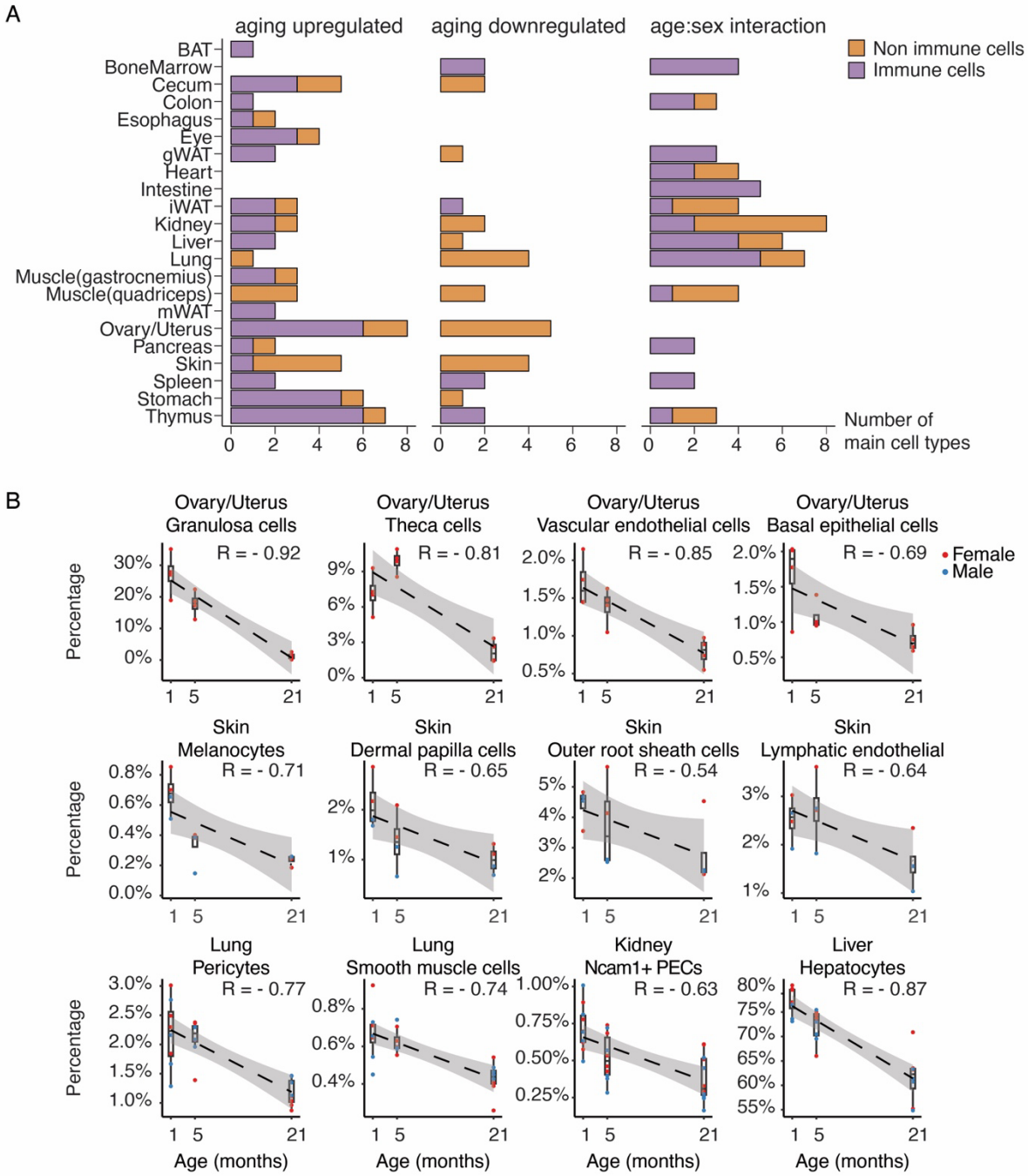

Figure S6. Aging-associated depletion of functional cell types across tissues.
(A) Bar plot showing the number of main cell types derived from immune cell types or non-immune cell types within aging-associated, sex-independent (aging-up and aging-down), or age-sex interaction groups for each tissue.
(B) Scatterplot showing examples of main cell types that decline with age across tissues, with a linear regression line (and a Pearson correlation coefficient). Each dot represents the cell-type specific proportion of the cell type in each animal.

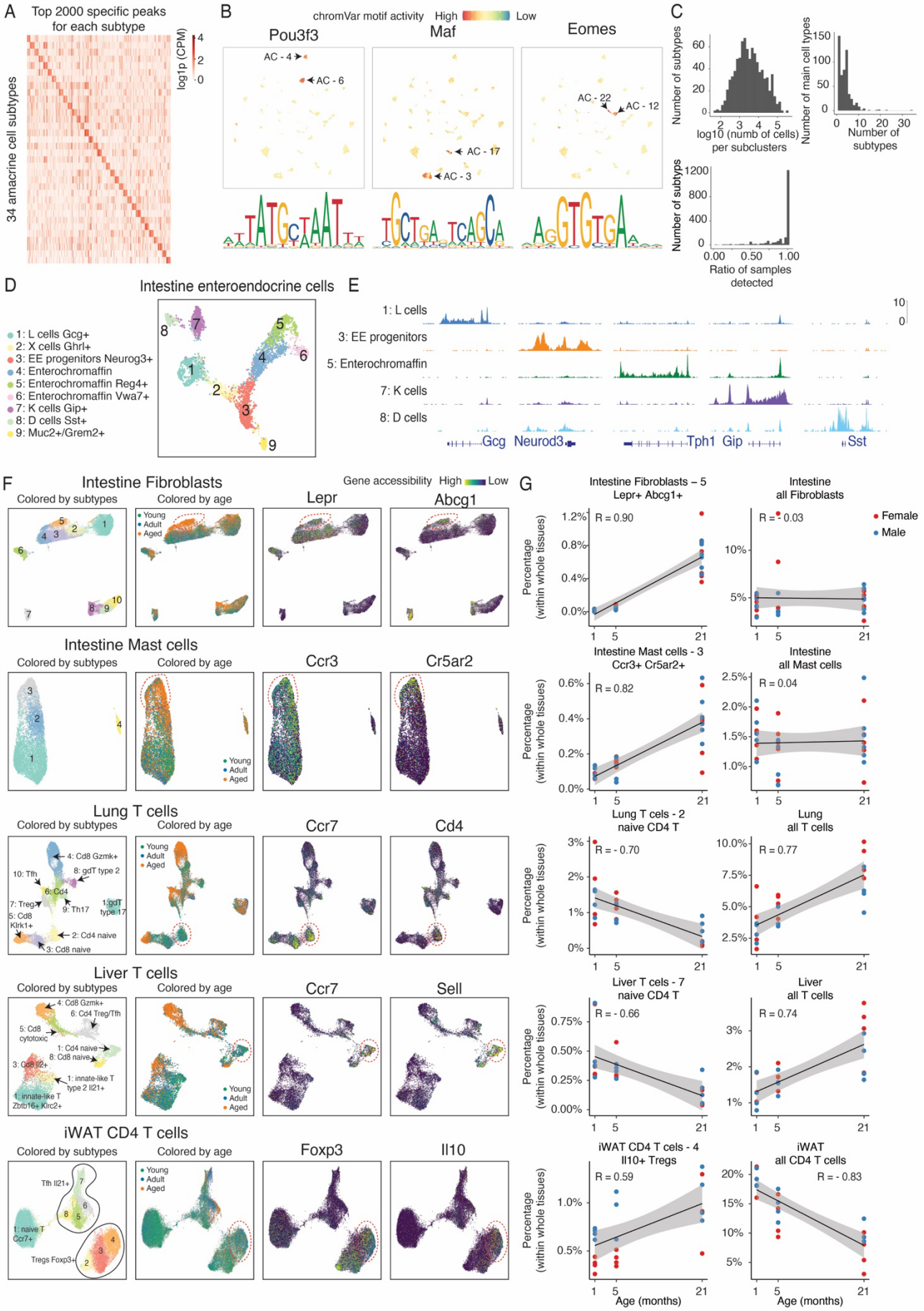
A
Top 2000 specific peaks for each subtype
34 amacrine cell subtypes
log1p (CPM)
B
chromVar motif activity High Low
Pou3f3
Maf
Eomes
AC - 4
AC - 6
AC - 17
AC - 3
AC - 22
AC - 12
C
Number of subtypes
log10 (numb of cells) per subclusters
Number of main cell types
Number of subtypes
Ratio of samples detected
D
Intestine enteroendocrine cells
1: L cells Gcg+
2: X cells Ghrl+
3: EE progenitors Neurog3+
4: Enterochromaffin
5: Enterochromaffin Reg4+
6: Enterochromaffin Vwa7+
7: K cells Gip+
8: D cells Sst+
9: Muc2+/Grem2+
E
1: L cells
3: EE progenitors
5: Enterochromaffin
7: K cells
8: D cells
Gcg
Neurod3
Tph1
Gip
Sst
F
Intestine Fibroblasts
Colored by subtypes
Colored by age
Lepr
Abcg1
Gene accessibility High Low
Young
Adult
Aged
Intestine Mast cells
Ccr3
Cr5ar2
Lung T cells
Ccr7
Cd4
4: Cd8 Gzmk+
8: gdT type 2
10: Tfh
6: Cd4
7: Treg
9: Th17
1: gdT type 17
5: Cd8 Klrk1+
2: Cd4 naive
3: Cd8 naive
Liver T cells
Sell
4: Cd8 Gzmk+
6: Cd4 Treg/Tfh
5: Cd8 cytotoxic
1: Cd4 naive
8: Cd8 naive
3: Cd8 Il2+
1: innate-like T type 2 Il21+
1: innate-like T Zbtb16+ Klrc2+
iWAT CD4 T cells
Foxp3
Il10
Tfh Il21+
1: naive T Ccr7+
Tregs Foxp3+
G
Intestine Fibroblasts – 5 Lepr+ Abcg1+
R = 0.90
Intestine all Fibroblasts
R = - 0.03
Female
Male
Intestine Mast cells - 3 Ccr3+ Cr5ar2+
R = 0.82
Intestine all Mast cells
R = 0.04
Lung T cels - 2 naive CD4 T
R = - 0.70
Lung all T cells
R = 0.77
Liver T cels - 7 naive CD4 T
R = - 0.66
Liver all T cells
R = 0.74
iWAT CD4 T cels - 4 Il10+ Tregs
R = 0.59
iWAT all CD4 T cells
R = - 0.83
Percentage (within whole tissues)
Age (months)

Figure S7. Identifications of cell subtypes and associated population changes in aging.

(A) Heatmap showing the aggregated accessibility of peaks specific to each main subtype in amacrine cells, quantified by counts per million.

(B) UMAP visualization of eye amacrine cells, colored by motif accessibilities of example transcription factors specific to distinct subtypes. Motif activities were quantified by chromVar (*21*).

(C) Histograms showing the distribution of cell numbers per subtype (Top left), the number of subtypes per main cell type (Top right), and the fraction of tissue samples that contain cells from each cell subtype (Bottom left).

(D) UMAP visualization of intestine enteroendocrine cells, colored by subtype identity.

(E) Genomic tracks showing the gene accessibilities marking different subtypes of intestine enteroendocrine cells.

(F) UMAP plots showing subclustering results for intestine fibroblasts, intestine mast cells, lung T cells, liver T cells and iWAT CD4 T cells, colored by subtype ID, age group, and accessibilities of genes marking circled subclusters.

(G) Scatterplot showing the proportion changes of indicated subclusters and their parental main cell types with age, along with a linear regression line.

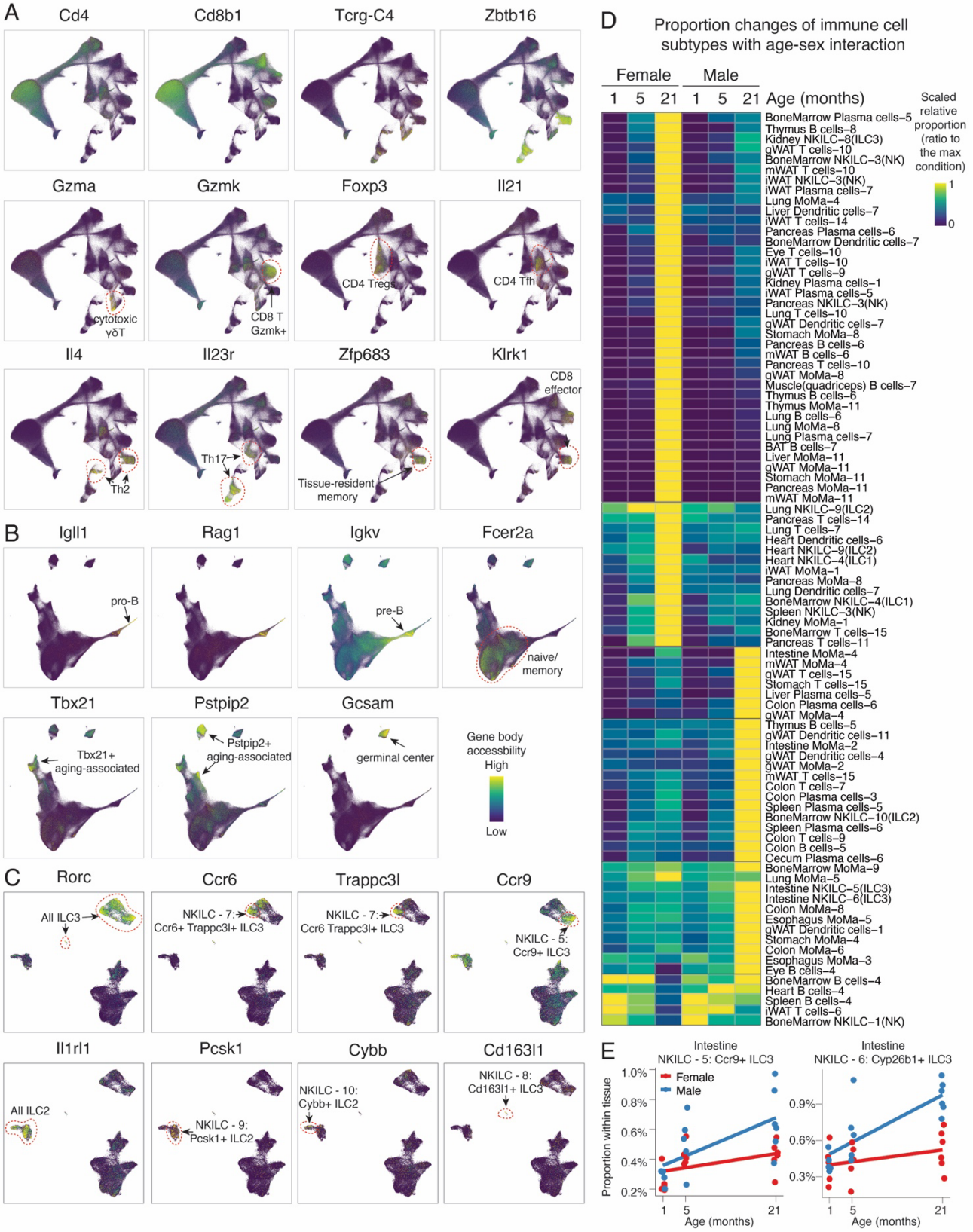
A
Cd4
Cd8b1
Tcrg-C4
Zbtb16
Gzma
Gzmk
Foxp3
Il21
cytotoxic γδT
CD8 T Gzmk+
CD4 Treg
CD4 Tfh
Il4
Il23r
Zfp683
Klrk1
Th2
Th17
Tissue-resident memory
CD8 effector
B
Igll1
Rag1
Igkv
Fcer2a
pro-B
pre-B
naive/ memory
Tbx21
Pstpip2
Gcsam
Tbx21+ aging-associated
Pstpip2+ aging-associated
germinal center
Gene body accessbility
High
Low
C
Rorc
Ccr6
Trappc3l
Ccr9
All ILC3
NKILC - 7: Ccr6+ Trappc3l+ ILC3
NKILC - 7: Ccr6 Trappc3l+ ILC3
NKILC - 5: Ccr9+ ILC3
Il1rl1
Pcsk1
Cybb
Cd163l1
All ILC2
NKILC - 9: Pcsk1+ ILC2
NKILC - 10: Cybb+ ILC2
NKILC - 8: Cd163l1+ ILC3
D
Proportion changes of immune cell subtypes with age-sex interaction
Female
Male
1 5 21 1 5 21 Age (months)
Scaled relative proportion (ratio to the max condition)
1
0
BoneMarrow Plasma cells–5
Thymus B cells–8
Kidney NKILC–8(ILC3)
gWAT T cells–10
BoneMarrow NKILC–3(NK)
mWAT T cells–10
iWAT NKILC–3(NK)
iWAT Plasma cells–7
Lung MoMa–4
Liver Dendritic cells–7
iWAT T cells–14
Pancreas Plasma cells–6
BoneMarrow Dendritic cells–7
Eye T cells–10
iWAT T cells–10
gWAT T cells–9
Kidney Plasma cells–1
iWAT Plasma cells–5
Pancreas NKILC–3(NK)
Lung T cells–10
gWAT Dendritic cells–7
Stomach MoMa–8
Pancreas B cells–6
mWAT B cells–6
Pancreas T cells–10
gWAT MoMa–8
Muscle(quadriceps) B cells–7
Thymus B cells–6
Thymus MoMa–11
Lung B cells–6
Lung MoMa–8
Lung Plasma cells–7
BAT B cells–7
Liver MoMa–11
gWAT MoMa–11
Stomach MoMa–11
Pancreas MoMa–11
mWAT MoMa–11
Lung NKILC–9(ILC2)
Pancreas T cells–14
Lung T cells–7
Heart Dendritic cells–6
Heart NKILC–9(ILC2)
Heart NKILC–4(ILC1)
iWAT MoMa–1
Pancreas MoMa–8
Lung Dendritic cells–7
BoneMarrow NKILC–4(ILC1)
Spleen NKILC–3(NK)
Kidney MoMa–1
BoneMarrow T cells–15
Pancreas T cells–11
Intestine MoMa–4
mWAT MoMa–4
gWAT T cells–15
Stomach T cells–15
Liver Plasma cells–5
Colon Plasma cells–6
gWAT MoMa–4
Thymus B cells–5
gWAT Dendritic cells–11
Intestine MoMa–2
gWAT Dendritic cells–4
gWAT MoMa–2
mWAT T cells–15
Colon T cells–7
Colon Plasma cells–3
Spleen Plasma cells–5
BoneMarrow NKILC–10(ILC2)
Spleen Plasma cells–6
Colon T cells–9
Colon B cells–5
Cecum Plasma cells–6
BoneMarrow MoMa–9
Lung MoMa–5
Intestine NKILC–5(ILC3)
Intestine NKILC–6(ILC3)
Colon MoMa–8
Esophagus MoMa–5
gWAT Dendritic cells–1
Stomach MoMa–4
Colon MoMa–6
Esophagus MoMa–3
Eye B cells–4
BoneMarrow B cells–4
Heart B cells–4
Spleen B cells–4
iWAT T cells–6
BoneMarrow NKILC–1(NK)
E
Intestine
NKILC - 5: Ccr9+ ILC3
Intestine
NKILC - 6: Cyp26b1+ ILC3
Female
Male
Proportion within tissue
1.0%
0.8%
0.6%
0.4%
0.2%
0.9%
0.6%
0.3%
1 5 21
Age (months)

Figure S8. Global characterizations of immune cell states and their proportional changes with age.

(A) UMAP plots showing combined clustering of all T cells across tissues, colored by accessibilities of genes marking distinct subtypes.

(B) UMAP plots showing combined clustering of all B cells across tissues, colored by accessibilities of genes marking distinct subtypes.

(C) UMAP plots showing combined clustering of all innate lymphoid cells across tissues, including NK cells, ILC1, ILC2 and ILC3, colored by accessibilities of genes marking distinct subtypes.

(D) Heatmap of relative proportions of immune cell subtypes with significant age-sex interactions. Rows represent immune cell subtypes within their respective tissues, while columns correspond to mouse conditions grouped by age and sex. For each immune cell subtype within each tissue, its proportion (within each tissue) were first averaged across samples and then normalized to the maximum value within each row.

(E) Scatterplot showing male-baised expansions of *Ccr9*+ ILC3 and *Ccr6*+ *Cyp26b1*+ ILC3 in intestine along aging. Each dot represents one animal, with linear regression lines added for each sex.

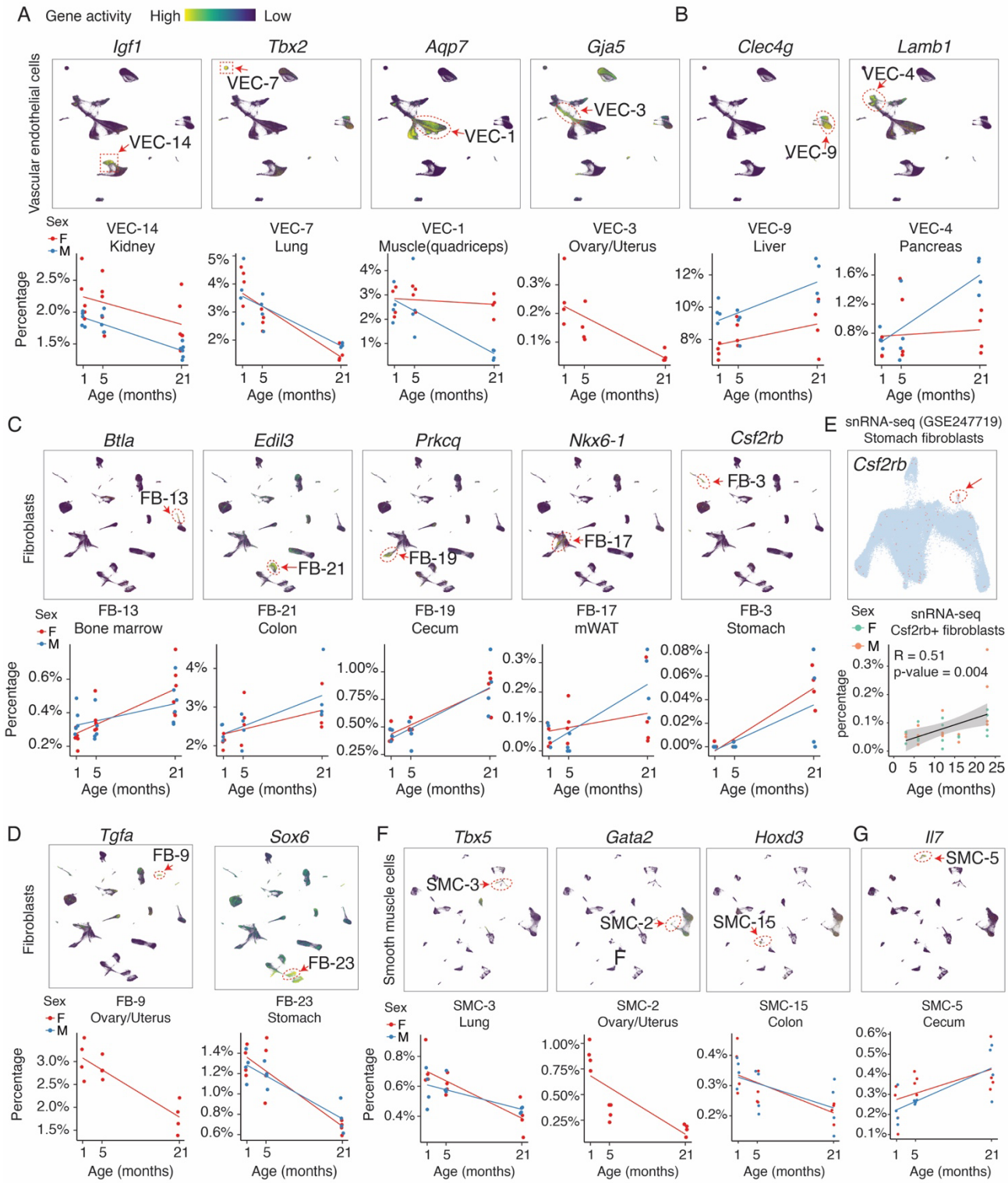
A
Gene activity
High
Low
B
Igf1
Tbx2
Aqp7
Gja5
Clec4g
Lamb1
Vascular endothelial cells
VEC-14
VEC-7
VEC-1
VEC-3
VEC-9
VEC-4
Sex
F
M
VEC-14 Kidney
VEC-7 Lung
VEC-1 Muscle(quadriceps)
VEC-3 Ovary/Uterus
VEC-9 Liver
VEC-4 Pancreas
Percentage
Age (months)
C
Btla
Edil3
Prkcq
Nkx6-1
Csf2rb
Fibroblasts
FB-13
FB-21
FB-19
FB-17
FB-3
FB-13 Bone marrow
FB-21 Colon
FB-19 Cecum
FB-17 mWAT
FB-3 Stomach
E
snRNA-seq (GSE247719)
Stomach fibroblasts
Csf2rb
snRNA-seq Csf2rb+ fibroblasts
R = 0.51
p-value = 0.004
percentage
D
Tgfa
Sox6
FB-9
FB-23
FB-9 Ovary/Uterus
FB-23 Stomach
F
Tbx5
Gata2
Hoxd3
Smooth muscle cells
SMC-3
SMC-2
SMC-15
SMC-3 Lung
SMC-2 Ovary/Uterus
SMC-15 Colon
G
Il7
SMC-5
SMC-5 Cecum

Figure S9. Cross-tissue identifications of subtypes for vascular endothelial cells, fibroblasts, smooth muscle cells and their aging-associated population changes.

(A-B) Top: UMAP plots showing the combined clustering results of vascular endothelial cells, colored by the accessibility of genes representing subtypes that expand (A) or deplete (B) with age. Bottom: Scatterplots showing the proportions of the indicated subtypes (normalized to total cells within the tissue) across three age groups, with linear regression lines added for each sex.

(C-D) UMAP plots showing the combined clustering results of fibroblasts, colored by the accessibility of genes representing subtypes that expand (C) or deplete (D) with age. Bottom: Scatterplots showing the proportions of the indicated subtypes (normalized to total cells within the tissue) across three age groups, with linear regression lines added for each sex.

(E) Validation of *Csf2rb*+ fibroblast expansion, as shown in (C), in aged stomach tissue using published snRNA-seq data (*7*). Left: UMAP plot of stomach fibroblasts colored by *Csf2rb* expression. Right: Scatterplot showing age-dependent expansion in *Csf2rb*+ fibroblasts, together with a linear regression line.

(F-G) Top: UMAP plots showing the combined clustering results of smooth muscle cells, colored by the accessibility of genes representing subtypes that deplete (F) or expand (G) with age. Bottom: Scatterplots showing the proportions of the indicated subtypes (normalized to total cells within the tissue) across three age groups, with linear regression lines added for each sex.

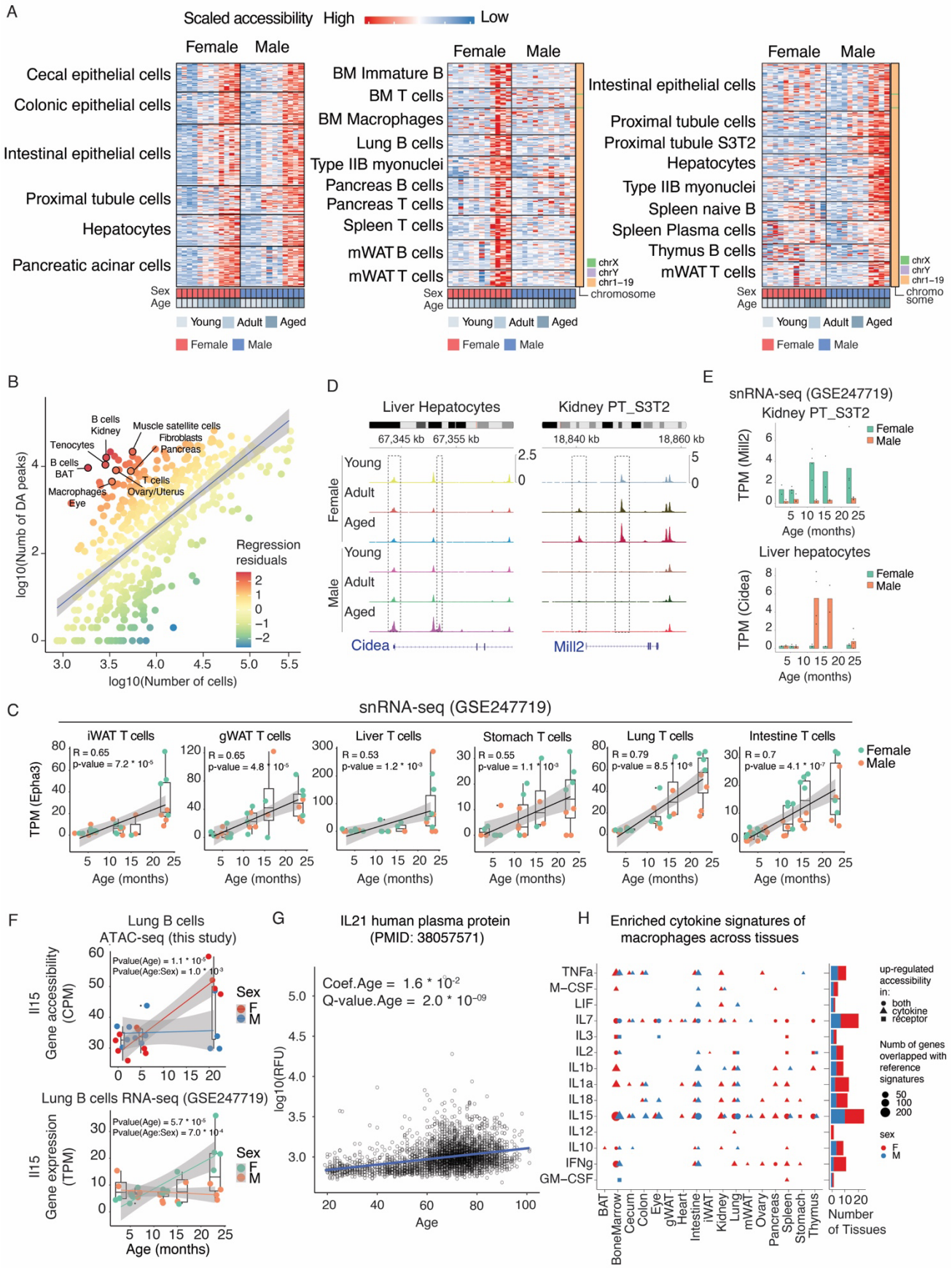
A
Scaled accessibility High Low
Female Male
Cecal epithelial cells
Colonic epithelial cells
Intestinal epithelial cells
Proximal tubule cells
Hepatocytes
Pancreatic acinar cells
BM Immature B
BM T cells
BM Macrophages
Lung B cells
Type IIB myonuclei
Pancreas B cells
Pancreas T cells
Spleen T cells
mWAT B cells
mWAT T cells
Proximal tubule S3T2
Spleen naive B
Spleen Plasma cells
Thymus B cells
chrX
chrY
chr1–19
chromosome
Sex
Age
Young Adult Aged
Female Male
B
log10(Numb of DA peaks)
log10(Number of cells)
B cells
Kidney
Muscle satellite cells
Fibroblasts
Pancreas
Tenocytes
B cells
BAT
T cells
Ovary/Uterus
Macrophages
Eye
Regression residuals
D
Liver Hepatocytes
Kidney PT_S3T2
67,345 kb 67,355 kb
18,840 kb 18,860 kb
Young
Adult
Aged
Female
Male
Cidea
Mill2
E
snRNA-seq (GSE247719)
Kidney PT_S3T2
TPM (Mill2)
Liver hepatocytes
TPM (Cidea)
Age (months)
C
snRNA-seq (GSE247719)
iWAT T cells
gWAT T cells
Liver T cells
Stomach T cells
Lung T cells
Intestine T cells
TPM (Epha3)
R = 0.65
p-value = 7.2 * 10-5
R = 0.65
p-value = 4.8 * 10-5
R = 0.53
p-value = 1.2 * 10-3
R = 0.55
p-value = 1.1 * 10-3
R = 0.79
p-value = 8.5 * 10-6
R = 0.7
p-value = 4.1 * 10-7
Age (months)
F
Lung B cells
ATAC-seq (this study)
Il15 Gene accessibility (CPM)
Pvalue(Age) = 1.1 * 10-5
Pvalue(Age:Sex) = 1.0 * 10-3
Lung B cells RNA-seq (GSE247719)
Il15 Gene expression (TPM)
Pvalue(Age) = 5.7 * 10-5
Pvalue(Age:Sex) = 7.0 * 10-4
Sex
F
M
Age (months)
G
IL21 human plasma protein
(PMID: 38057571)
Coef.Age = 1.6 * 10-2
Q-value.Age = 2.0 * 10-09
log10(RFU)
Age
H
Enriched cytokine signatures of
macrophages across tissues
TNFa
M-CSF
LIF
IL7
IL3
IL2
IL1b
IL1a
IL18
IL15
IL12
IL10
IFNg
GM-CSF
BAT
BoneMarrow
Cecum
Colon
Eye
gWAT
Heart
Intestine
iWAT
Kidney
Lung
mWAT
Ovary
Pancreas
Spleen
Stomach
Thymus
up-regulated accessibility in:
both
cytokine
receptor
Numb of genes overlapped with reference signatures
50
100
200
sex
F
M
Number of Tissues

Figure S10. Identifications of cell-type-specific molecular changes in aging.

(A) Heatmaps showing examples of differentially accessible (DA) peaks that are sex-shared (left), female-specific (middle), and male-specific (right). Rows correspond to DA peaks identified in each main cell type, while columns represent individual mice. Peak accessibility was quantified as counts per million for each sample in each cell type.

(B) Scatterplot showing the correlation between the number of cells and the number of DA peaks across cell types, with a linear regression fit. Cell types with high regression residuals are labeled.

(C) Scatterplot showing the increased expression of *Epha3* in T cells across multiple tissues, with a linear regression line, validating the chromatin changes in Figure 6F.

(D) Genomic tracks of male-specific DA peak in liver hepatocytes (left) and female-specific DA peak kidney proximal tubule cells S3T2 (right).

(E) Barplot showing validation of sex-specific chromatin accessibility changes in (D) using gene expression data of the same cell type. Dot represents animals.

(F) Scatterplots showing the increased gene accessibility (top) and expression (bottom) of *Il15* in lung B cells, specifically in females, with linear regression lines added for each sex.

(G) Scatterplot showing the age-related increase in plasma protein levels of IL-21. Data was obtained from (*3*), with a linear regression line included.

(H) Left: Dot plot summarizing cytokine signatures enriched in aged macrophages across tissues. Only signatures supported by accessibility changes in secretion or receptor genes are shown. Right: Bar plot summarizing the number of tissues exhibiting activated signatures for each cytokine, separated by sex.

Supplementary Tables

Table S1. Metadata for animals included in this study.
Table S2. List of gene markers used for cell type annotations.
Table S3.List of cell-type-specific peaks, including the counts per million (CPM) value for the most accessible cell type and the mean CPM across all cell types for each peak
Table S4. Differentially abundant main cell types with age across tissues. “qvalue_age” indicates the significance of a non-zero coefficient for the age term. “qvalue_interaction” indicates the significance of a non-zero coefficient for the age-sex interaction term. “Regression R2” refers to the coefficient of determination of the regression model. “Pearson r” means the Pearson correlation r calculated between cell fraction of each main cell type within their corresponding tissues and ages, including samples of both sexes.
Table S5. Differentially abundant subtypes with age across tissues. “qvalue_age” indicates the significance of a non-zero coefficient for the age term. “qvalue_interaction” indicates the significance of a non-zero coefficient for the age-sex interaction term. “Regression R2” refers to the coefficient of determination of the regression model. “Pearson r” means the Pearson correlation r calculated between cell fraction of each subtype within their corresponding tissues and ages, including samples of both sexes.
Table S6. Differential accessible peaks with age shared in both sexes, including logFC, p-value, and q-value for each peak in both females and males.
Table S7. Differential accessible peaks with age unique to females, logFC, p-value, and q-value for each peak in both females and males.
Table S8. Differential accessible peaks with age unique to males, logFC, p-value, and q-value for each peak in both females and males.
Table S9. Aging-associated linkages with consistent changes in gene expression and chromatin accessibility at promoters and putative cis-regulatory elements. Each row represents a gene-peak-CRE linkage, including the gene name and genomic coordinates of the promoter and linked cis-regulatory site. The column “group” indicates whether the linkage is identified from both sexes or from one sex.

References:

1. T. Niccoli, L. Partridge, Ageing as a risk factor for disease. *Curr Biol* **22**, R741–52 (2012).

2. Y. E. Tian, V. Cropley, A. B. Maier, N. T. Lautenschlager, M. Breakspear, A. Zalesky, Heterogeneous aging across multiple organ systems and prediction of chronic disease and mortality. *Nat Med* **29**, 1221–1231 (2023).

3. H. S.-H. Oh, J. Rutledge, D. Nachun, R. Pálovics, O. Abiose, P. Moran-Losada, D. Channappa, D. Y. Urey, K. Kim, Y. J. Sung, L. Wang, J. Timsina, D. Western, M. Liu, P. Kohlfeld, J. Budde, E. N. Wilson, Y. Guen, T. M. Maurer, M. Haney, A. C. Yang, Z. He, M. D. Greicius, K. I. Andreasson, S. Sathyan, E. F. Weiss, S. Milman, N. Barzilai, C. Cruchaga, A. D. Wagner, E. Mormino, B. Lehallier, V. W. Henderson, F. M. Longo, S. B. Montgomery, T. Wyss-Coray, Organ aging signatures in the plasma proteome track health and disease. *Nature* **624**, 164–172 (2023).

4. K. Jin, Z. Yao, C. T. J. van Velthoven, E. S. Kaplan, K. Glattfelder, S. T. Barlow, G. Boyer, D. Carey, T. Casper, A. B. Chakka, R. Chakrabarty, M. Clark, M. Departee, M. Desierto, A. Gary, J. Gloe, J. Goldy, N. Guilford, J. Guzman, D. Hirschstein, C. Lee, E. Liang, T. Pham, M. Reding, K. Ronellenfitch, A. Ruiz, J. Sevigny, N. Shapovalova, L. Shulga, J. Sulc, A. Torkelson, H. Tung, B. Levi, S. M. Sunkin, N. Dee, L. Esposito, K. A. Smith, B. Tasic, H. Zeng, Brain-wide cell-type-specific transcriptomic signatures of healthy ageing in mice. *Nature*, doi: 10.1038/s41586-024-08350-8 (2025).

5. R. Wang, P. Zhang, J. Wang, L. Ma, W. E, S. Suo, M. Jiang, J. Li, H. Chen, H. Sun, L. Fei, Z. Zhou, Y. Zhou, Y. Chen, W. Zhang, X. Wang, Y. Mei, Z. Sun, C. Yu, J. Shao, Y. Fu, Y. Xiao, F. Ye, X. Fang, H. Wu, Q. Guo, X. Fang, X. Li, X. Gao, D. Wang, P.-F. Xu, R. Zeng, G. Xu, L. Zhu, L. Wang, J. Qu, D. Zhang, H. Ouyang, H. Huang, M. Chen, S.-C. Ng, G.-H. Liu, G.-C. Yuan, G. Guo, X. Han, Construction of a cross-species cell landscape at single-cell level. *Nucleic Acids Res* **51**, 501–516 (2023).

6. T.-C. Lu, M. Brbić, Y.-J. Park, T. Jackson, J. Chen, S. S. Kolluru, Y. Qi, N. S. Katheder, X. T. Cai, S. Lee, Y.-C. Chen, N. Auld, C.-Y. Liang, S. H. Ding, D. Welsch, S. D'Souza, A. O. Pisco, R. C. Jones, J. Leskovec, E. C. Lai, H. J. Bellen, L. Luo, H. Jasper, S. R. Quake, H. Li, Aging Fly Cell Atlas identifies exhaustive aging features at cellular resolution. *Science* **380**, eadg0934 (2023).

7. Z. Zhang, C. Schaefer, W. Jiang, Z. Lu, J. Lee, A. Sziraki, A. Abdulraouf, B. Wick, M. Haeussler, Z. Li, G. Molla, R. Satija, W. Zhou, J. Cao, A panoramic view of cell population dynamics in mammalian aging. *Science* **387**, eadn3949 (2025).

8. J. J. Beintema, R. N. Campagne, M. Gruber, Rat pancreatic ribonuclease. I. Isolation and properties. *Biochim Biophys Acta* **310**, 148–160 (1973).

9. A. M. Al-Adsani, S. A. Barhoush, N. K. Bastaki, S. A. Al-Bustan, K. K. Al-Qattan, Comparing and Optimizing RNA Extraction from the Pancreas of Diabetic and Healthy Rats for Gene Expression Analyses. *Genes (Basel)* **13** (2022).

10. F. V. De Rop, G. Hulselmans, C. Flerin, P. Soler-Vila, A. Rafels, V. Christiaens, C. B. González-Blas, D. Marchese, G. Caratù, S. Poovathingal, O. Rozenblatt-Rosen, M. Slyper, W. Luo, C. Muus, F. Duarte, R. Shrestha, S. T. Bagdatli, M. R. Corces, L. Mamanova, A. Knights, K. B. Meyer, R. Mulqueen, A. Taherinasab, P. Maschmeyer, J. Pezoldt, C. L. G. Lambert, M. Iglesias, S. R. Najle, Z. Y. Dossani, L. G. Martelotto, Z. Burkett, R. Lebofsky, J. I. Martin-Subero, S. Pillai, A. Sebé-Pedrós, B. Deplancke, S. A. Teichmann, L. S. Ludwig, T. P. Braun, A. C. Adey, W. J. Greenleaf, J. D. Buenrostro, A. Regev, S. Aerts, H. Heyn, Systematic benchmarking of single-cell ATAC-sequencing protocols. *Nat Biotechnol* **42**, 916–926 (2024).

11. S. Domcke, A. J. Hill, R. M. Daza, J. Cao, D. R. O'Day, H. A. Pliner, K. A. Aldinger, D. Pokholok, F. Zhang, J. H. Milbank, M. A. Zager, I. A. Glass, F. J. Steemers, D. Doherty, C. Trapnell, D. A. Cusanovich, J. Shendure, A human cell atlas of fetal chromatin accessibility. *Science* **370** (2020).

12. K. Zhang, J. D. Hocker, M. Miller, X. Hou, J. Chiou, O. B. Poirion, Y. Qiu, Y. E. Li, K. J. Gaulton, A. Wang, S. Preissl, B. Ren, A single-cell atlas of chromatin accessibility in the human genome. *Cell* **184**, 5985–6001.e19 (2021).

13. Y. E. Li, S. Preissl, M. Miller, N. D. Johnson, Z. Wang, H. Jiao, C. Zhu, Z. Wang, Y. Xie, O. Poirion, C. Kern, A. Pinto-Duarte, W. Tian, K. Siletti, N. Emerson, J. Osteen, J. Lucero, L. Lin, Q. Yang, Q. Zhu, N. Zemke, S. Espinoza, A. M. Yanny, J. Nyhus, N. Dee, T. Casper, N. Shapovalova, D. Hirschstein, R. D. Hodge, S. Linnarsson, T. Bakken, B. Levi, C. D. Keene, J. Shang, E. Lein, A. Wang, M. M. Behrens, J. R. Ecker, B. Ren, A comparative atlas of single-cell chromatin accessibility in the human brain. *Science* **382**, eadf7044 (2023).

14. S. Zu, Y. E. Li, K. Wang, E. J. Armand, S. Mamde, M. L. Amaral, Y. Wang, A. Chu, Y. Xie, M. Miller, J. Xu, Z. Wang, K. Zhang, B. Jia, X. Hou, L. Lin, Q. Yang, S. Lee, B. Li, S. Kuan, H. Liu, J. Zhou, A. Pinto-Duarte, J. Lucero, J. Osteen, M. Nunn, K. A. Smith, B. Tasic, Z. Yao, H. Zeng, Z. Wang, J. Shang, M. M. Behrens, J. R. Ecker, A. Wang, S. Preissl, B. Ren, Single-cell analysis of chromatin accessibility in the adult mouse brain. *Nature* **624**, 378–389 (2023).

15. A. Sziraki, Z. Lu, J. Lee, G. Banyai, S. Anderson, A. Abdulraouf, E. Metzner, A. Liao, J. Banfelder, A. Epstein, C. Schaefer, Z. Xu, Z. Zhang, L. Gan, P. T. Nelson, W. Zhou, J. Cao, A global view of aging and Alzheimer's pathogenesis-associated cell population dynamics and molecular signatures in human and mouse brains. *Nature Genetics* **55**, 2104–2116 (2023).

16. Z. Lu, M. Zhang, J. Lee, A. Sziraki, S. Anderson, Z. Zhang, Z. Xu, W. Jiang, S. Ge, P. T. Nelson, W. Zhou, J. Cao, Tracking cell-type-specific temporal dynamics in human and mouse brains. *Cell* **186**, 4345–4364.e24 (2023).

17. K. Zhang, N. R. Zemke, E. J. Armand, B. Ren, A fast, scalable and versatile tool for analysis of single-cell omics data. *Nature Methods* **21**, 217–227 (2024).

18. A. Charrier, D. R. Brigstock, Regulation of pancreatic function by connective tissue growth factor (CTGF, CCN2). *Cytokine Growth Factor Rev* **24**, 59–68 (2013).

19. Å. Segerstolpe, A. Palasantza, P. Eliasson, E.-M. Andersson, A.-C. Andréasson, X. Sun, S. Picelli, A. Sabirsh, M. Clausen, M. K. Bjursell, D. M. Smith, M. Kasper, C. Ämmälä, R. Sandberg, Single-Cell Transcriptome Profiling of Human Pancreatic Islets in Health and Type 2 Diabetes. *Cell Metab* **24**, 593–607 (2016).

20. J. E. Moore, M. J. Purcaro, H. E. Pratt, C. B. Epstein, N. Shoresh, J. Adrian, T. Kawli, C. A. Davis, A. Dobin, R. Kaul, J. Halow, E. L. Van Nostrand, P. Freese, D. U. Gorkin, Y. Shen, Y. He, M. Mackiewicz, F. Pauli-Behn, B. A. Williams, A. Mortazavi, C. A. Keller, X.-O. Zhang, S. I. Elhajjajy, J. Huey, D. E. Dickel, V. Snetkova, X. Wei, X. Wang, J. C. Rivera-Mulia, J. Rozowsky, J. Zhang, S. B. Chhetri, J. Zhang, A. Victorsen, K. P. White, A. Visel, G. W. Yeo, C. B. Burge, E. Lécuyer, D. M. Gilbert, J. Dekker, J. Rinn, E. M. Mendenhall, J. R. Ecker, M. Kellis, R. J. Klein, W. S. Noble, A. Kundaje, R. Guigó, P. J. Farnham, J. M. Cherry, R. M. Myers, B. Ren, B. R. Graveley, M. B. Gerstein, L. A. Pennacchio, M. P. Snyder, B. E. Bernstein, B. Wold, R. C. Hardison, T. R. Gingeras, J. A. Stamatoyannopoulos, Z. Weng, Expanded encyclopaedias of DNA elements in the human and mouse genomes. *Nature* **583**, 699–710 (2020).

21. A. N. Schep, B. Wu, J. D. Buenrostro, W. J. Greenleaf, chromVAR: inferring transcription-factor-associated accessibility from single-cell epigenomic data. *Nat. Methods* **14**, 975–978 (2017).

22. Q. Shan, Z. Zeng, S. Xing, F. Li, S. M. Hartwig, J. A. Gullicksrud, S. P. Kurup, N. Van Braeckel-

Budimir, Y. Su, M. D. Martin, S. M. Varga, I. Taniuchi, J. T. Harty, W. Peng, V. P. Badovinac, H.-H. Xue, The transcription factor Runx3 guards cytotoxic CD8 effector T cells against deviation towards follicular helper T cell lineage. *Nat Immunol* **18**, 931–939 (2017).

23. C. V. Laiosa, M. Stadtfeld, T. Graf, Determinants of lymphoid-myeloid lineage diversification. *Annu Rev Immunol* **24**, 705–738 (2006).

24. U. Klein, S. Casola, G. Cattoretti, Q. Shen, M. Lia, T. Mo, T. Ludwig, K. Rajewsky, R. Dalla-Favera, Transcription factor IRF4 controls plasma cell differentiation and class-switch recombination. *Nat Immunol* **7**, 773–782 (2006).

25. R. Nechanitzky, D. Akbas, S. Scherer, I. Györy, T. Hoyler, S. Ramamoorthy, A. Diefenbach, R. Grosschedl, Transcription factor EBF1 is essential for the maintenance of B cell identity and prevention of alternative fates in committed cells. *Nature Immunology* **14**, 867–875 (2013).

26. F. Pagani, E. Tratta, P. Dell'Era, M. Cominelli, P. L. Poliani, EBF1 is expressed in pericytes and contributes to pericyte cell commitment. *Histochem Cell Biol* **156**, 333–347 (2021).

27. D. McClellan, M. J. Casey, D. Bareyan, H. Lucente, C. Ours, M. Velinder, J. Singer, M. D. Lone, W. Sun, Y. Coria, C. C. Mason, M. E. Engel, Growth Factor Independence 1B-Mediated Transcriptional Repression and Lineage Allocation Require Lysine-Specific Demethylase 1-Dependent Recruitment of the BHC Complex. *Mol Cell Biol* **39** (2019).

28. B. K. Bulik-Sullivan, P.-R. Loh, H. K. Finucane, S. Ripke, J. Yang, N. Patterson, M. J. Daly, A. L. Price, B. M. Neale, LD Score regression distinguishes confounding from polygenicity in genome-wide association studies. *Nature Genetics* **47**, 291–295 (2015).

29. Y. Li, S. M. Laws, L. A. Miles, J. S. Wiley, X. Huang, C. L. Masters, B. J. Gu, Genomics of Alzheimer's disease implicates the innate and adaptive immune systems. *Cell Mol Life Sci* **78**, 7397–7426 (2021).

30. C. Scholz, K. T. Patton, D. E. Anderson, G. J. Freeman, D. A. Hafler, Expansion of autoreactive T cells in multiple sclerosis is independent of exogenous B7 costimulation. *J Immunol* **160**, 1532–1538 (1998).

31. G. Comi, A. Bar-Or, H. Lassmann, A. Uccelli, H.-P. Hartung, X. Montalban, P. S. Sørensen, R. Hohlfeld, S. L. Hauser, Expert Panel of the 27th Annual Meeting of the European Charcot Foundation, Role of B Cells in Multiple Sclerosis and Related Disorders. *Ann Neurol* **89**, 13–23 (2021).

32. J. L. Goldstein, M. S. Brown, Regulation of low-density lipoprotein receptors: implications for pathogenesis and therapy of hypercholesterolemia and atherosclerosis. *Circulation* **76**, 504–507 (1987).

33. C. Wysham, J. Shubrook, Beta-cell failure in type 2 diabetes: mechanisms, markers, and clinical implications. *Postgrad Med* **132**, 676–686 (2020).

34. H. Yamaguchi, R. A. Gomez, M. L. S. Sequeira-Lopez, Renin Cells, From Vascular Development to Blood Pressure Sensing. *Hypertension* **80**, 1580–1589 (2023).

35. L. Rodríguez-Montes, S. Ovchinnikova, X. Yuan, T. Studer, I. Sarropoulos, S. Anders, H. Kaessmann, M. Cardoso-Moreira, Sex-biased gene expression across mammalian organ development and evolution. *Science*, doi: 10.1126/science.adf1046 (2023).

36. A. Christianto, T. Baba, F. Takahashi, K. Inui, M. Inoue, M. Suyama, Y. Ono, Y. Ohkawa, K.-I. Morohashi, Sex differences in metabolic pathways are regulated by Pfkfb3 and Pdk4 expression in

493 rodent muscle. *Commun Biol* **4**, 1264 (2021).

494 37. D. Janosevic, J. Myslinski, T. W. McCarthy, A. Zollman, F. Syed, X. Xuei, H. Gao, Y.-L. Liu, K. S.
495 Collins, Y.-H. Cheng, S. Winfree, T. M. El-Achkar, B. Maier, R. Melo Ferreira, M. T. Eadon, T. Hato,
496 P. C. Dagher, The orchestrated cellular and molecular responses of the kidney to endotoxin define a
497 precise sepsis timeline. *Elife* **10** (2021).

498 38. A. Jagger, Y. Shimojima, J. J. Goronzy, C. M. Weyand, Regulatory T cells and the immune aging
499 process: a mini-review. *Gerontology* **60**, 130–137 (2014).

500 39. X. Li, C. Li, W. Zhang, Y. Wang, P. Qian, H. Huang, Inflammation and aging: signaling pathways and
501 intervention therapies. *Signal Transduct Target Ther* **8**, 239 (2023).

502 40. D. Frasca, M. Romero, D. Garcia, A. Diaz, B. B. Blomberg, Hyper-metabolic B cells in the spleens of
503 old mice make antibodies with autoimmune specificities. *Immun Ageing* **18**, 9 (2021).

504 41. S. N. Hilmer, V. C. Cogger, D. G. Le Couteur, Basal activity of Kupffer cells increases with old age. *J*
505 *Gerontol A Biol Sci Med Sci* **62**, 973–978 (2007).

506 42. S. Mukherjee, M. E. C. Bruno, J. Oakes, G. S. Hawk, A. J. Stromberg, D. A. Cohen, M. E. Starr,
507 Mechanisms of γδ T cell accumulation in visceral adipose tissue with aging. *Front Aging* **4**, 1258836
508 (2023).

509 43. Systematic analysis of muscle aging using joint single-cell and single-nucleus sequencing. *Nat*
510 *Aging* **4**, 621–622 (2024).

511 44. F. M. Gribble, F. Reimann, Function and mechanisms of enteroendocrine cells and gut hormones in
512 metabolism. *Nat Rev Endocrinol* **15**, 226–237 (2019).

513 45. J. de Mol, J. Kuiper, D. Tsiantoulas, A. C. Foks, The Dynamics of B Cell Aging in Health and
514 Disease. *Front Immunol* **12**, 733566 (2021).

515 46. R. Aspinall, Age-associated thymic atrophy in the mouse is due to a deficiency affecting
516 rearrangement of the TCR during intrathymic T cell development. *J Immunol* **158**, 3037–3045
517 (1997).

518 47. K. B. Menees, R. H. Earls, J. Chung, J. Jernigan, N. M. Filipov, J. M. Carpenter, J.-K. Lee, Sex- and
519 age-dependent alterations of splenic immune cell profile and NK cell phenotypes and function in
520 C57BL/6J mice. *Immun Ageing* **18**, 3 (2021).

521 48. E. R. Zacca, M. I. Crespo, R. P. Acland, E. Roselli, N. G. Núñez, M. Maccioni, B. A. Maletto, M. C.
522 Pistoresi-Palencia, G. Morón, Aging Impairs the Ability of Conventional Dendritic Cells to Cross-
523 Prime CD8+ T Cells upon Stimulation with a TLR7 Ligand. *PLoS One* **10**, e0140672 (2015).

524 49. C. Jin, X. Wang, J. Yang, S. Kim, A. D. Hudgins, A. Gamliel, M. Pei, D. Contreras, M. Devos, Q.
525 Guo, J. Vijg, M. Conti, J. Hoeijmakers, J. Campisi, R. Lobo, Z. Williams, M. G. Rosenfeld, Y. Suh,
526 Molecular and genetic insights into human ovarian aging from single-nuclei multi-omics analyses.
527 *Nat Aging*, doi: 10.1038/s43587-024-00762-5 (2024).

528 50. F. J. Broekmans, M. R. Soules, B. C. Fauser, Ovarian aging: mechanisms and clinical
529 consequences. *Endocr Rev* **30**, 465–493 (2009).

530 51. J. P. Ortonne, Pigmentary changes of the ageing skin. *Br J Dermatol* **122 Suppl 35**, 21–28 (1990).

531 52. R. P. Kataru, H. J. Park, J. Shin, J. E. Baik, A. Sarker, S. Brown, B. J. Mehrara, Structural and
532 Functional Changes in Aged Skin Lymphatic Vessels. *Front Aging* **3**, 864860 (2022).

53. A. Gillich, F. Zhang, C. G. Farmer, K. J. Travaglini, S. Y. Tan, M. Gu, B. Zhou, J. A. Feinstein, M. A. Krasnow, R. J. Metzger, Capillary cell-type specialization in the alveolus. *Nature* **586**, 785–789 (2020).

54. E. A. Hermann, A. Motahari, E. A. Hoffman, N. Allen, A. G. Bertoni, D. A. Bluemke, A. Eskandari, S. E. Gerard, J. Guo, G. T. Hiura, D. W. Kaczka, E. D. Michos, P. Nagpal, J. Pankow, S. Shah, B. M. Smith, K. Hinckley Stukovsky, Y. Sun, K. Watson, R. G. Barr, Pulmonary Blood Volume Among Older Adults in the Community: The MESA Lung Study. *Circ Cardiovasc Imaging* **15**, e014380 (2022).

55. S. J. Shankland, Y. Wang, A. S. Shaw, J. C. Vaughan, J. W. Pippin, O. Wessely, Podocyte Aging: Why and How Getting Old Matters. *J Am Soc Nephrol* **32**, 2697–2713 (2021).

56. W.-B. Liu, G.-R. Huang, B.-L. Liu, H.-K. Hu, J. Geng, H.-L. Rui, C. Gao, Y.-J. Huang, G.-Y. Huo, J.-R. Mao, C.-J. Lu, A.-L. Xu, Single cell landscape of parietal epithelial cells in healthy and diseased states. *Kidney Int* **104**, 108–123 (2023).

57. Tabula Muris Consortium, A single-cell transcriptomic atlas characterizes ageing tissues in the mouse. *Nature* **583**, 590–595 (2020).

58. W.-C. Tsai, H.-N. Chang, T.-Y. Yu, C.-H. Chien, L.-F. Fu, F.-C. Liang, J.-H. S. Pang, Decreased proliferation of aging tenocytes is associated with down-regulation of cellular senescence-inhibited gene and up-regulation of p27. *J Orthop Res* **29**, 1598–1603 (2011).

59. J. V. Chakkalakal, K. M. Jones, M. A. Basson, A. S. Brack, The aged niche disrupts muscle stem cell quiescence. *Nature* **490**, 355–360 (2012).

60. R. Pellegrino, R. Paganelli, A. Di Iorio, S. Bandinelli, A. Moretti, G. Iolascon, E. Sparvieri, D. Tarantino, L. Ferrucci, Temporal trends, sex differences, and age-related disease influence in Neutrophil, Lymphocyte count and Neutrophil to Lymphocyte-ratio: results from InCHIANTI follow-up study. *Immun Ageing* **20**, 46 (2023).

61. P. J. Busse, S. K. Mathur, Age-related changes in immune function: effect on airway inflammation. *J Allergy Clin Immunol* **126**, 690–9; quiz 700–1 (2010).

62. J. Li, J. Choi, X. Cheng, J. Ma, S. Pema, J. R. Sanes, G. Mardon, B. J. Frankfort, N. M. Tran, Y. Li, R. Chen, Comprehensive single-cell atlas of the mouse retina. *iScience* **27**, 109916 (2024).

63. S. J. Purohit, R. P. Stephan, H.-G. Kim, B. R. Herrin, L. Gartland, C. A. Klug, Determination of lymphoid cell fate is dependent on the expression status of the IL-7 receptor. *EMBO J* **22**, 5511–5521 (2003).

64. D. M. Poscablo, A. K. Worthington, S. Smith-Berdan, M. G. E. Rommel, B. A. Manso, R. Adili, L. Mok, R. E. Reggiardo, T. Cool, R. Mogharrab, J. Myers, S. Dahmen, P. Medina, A. E. Beaudin, S. W. Boyer, M. Holinstat, V. D. Jonsson, E. C. Forsberg, An age-progressive platelet differentiation path from hematopoietic stem cells causes exacerbated thrombosis. *Cell* **187**, 3090–3107.e21 (2024).

65. S. J. Dumas, E. Meta, M. Borri, J. Goveia, K. Rohlenova, N. V. Conchinha, K. Falkenberg, L.-A. Teuwen, L. de Rooij, J. Kalucka, R. Chen, S. Khan, F. Taverna, W. Lu, M. Parys, C. De Legher, S. Vinckier, T. K. Karakach, L. Schoonjans, L. Lin, L. Bolund, M. Dewerchin, G. Eelen, T. J. Rabelink, X. Li, Y. Luo, P. Carmeliet, Single-Cell RNA Sequencing Reveals Renal Endothelium Heterogeneity and Metabolic Adaptation to Water Deprivation. *J Am Soc Nephrol* **31**, 118–138 (2020).

66. D. A. Mogilenko, I. Shchukina, M. N. Artyomov, Immune ageing at single-cell resolution. *Nature Reviews Immunology* **22**, 484–498 (2021).

576 67. M. Kohyama, W. Ise, B. T. Edelson, P. R. Wilker, K. Hildner, C. Mejia, W. A. Frazier, T. L. Murphy,
577 K. M. Murphy, Role for Spi-C in the development of red pulp macrophages and splenic iron
578 homeostasis. *Nature* **457**, 318–321 (2009).

579 68. T. A. Fehniger, S. F. Cai, X. Cao, A. J. Bredemeyer, R. M. Presti, A. R. French, T. J. Ley, Acquisition
580 of murine NK cell cytotoxicity requires the translation of a pre-existing pool of granzyme B and
581 perforin mRNAs. *Immunity* **26**, 798–811 (2007).

582 69. V. Chiurchiù, M. Lanuti, M. De Bardi, L. Battistini, M. Maccarrone, The differential characterization of
583 GPR55 receptor in human peripheral blood reveals a distinctive expression in monocytes and NK
584 cells and a proinflammatory role in these innate cells. *Int Immunol* **27**, 153–160 (2015).

585 70. Gender differences in autoimmune disease. *Frontiers in Neuroendocrinology* **35**, 347–369 (2014).

586 71. M. Elderman, P. de Vos, M. Faas, Role of Microbiota in Sexually Dimorphic Immunity. *Front*
587 *Immunol* **9**, 1018 (2018).

588 72. J. Kalucka, L. P. M. H. de Rooij, J. Goveia, K. Rohlenova, S. J. Dumas, E. Meta, N. V. Conchinha, F.
589 Taverna, L.-A. Teuwen, K. Veys, M. García-Caballero, S. Khan, V. Geldhof, L. Sokol, R. Chen, L.
590 Treps, M. Borri, P. de Zeeuw, C. Dubois, T. K. Karakach, K. D. Falkenberg, M. Parys, X. Yin, S.
591 Vinckier, Y. Du, R. A. Fenton, L. Schoonjans, M. Dewerchin, G. Eelen, B. Thienpont, L. Lin, L.
592 Bolund, X. Li, Y. Luo, P. Carmeliet, Single-Cell Transcriptome Atlas of Murine Endothelial Cells. *Cell*
593 **180**, 764–779.e20 (2020).

594 73. S. Heinz, C. Benner, N. Spann, E. Bertolino, Y. C. Lin, P. Laslo, J. X. Cheng, C. Murre, H. Singh, C.
595 K. Glass, Simple combinations of lineage-determining transcription factors prime cis-regulatory
596 elements required for macrophage and B cell identities. *Mol Cell* **38**, 576–589 (2010).

597 74. J. Palomero, M. C. Vegliante, M. L. Rodríguez, A. Eguileor, G. Castellano, E. Planas-Rigol, P. Jares,
598 I. Ribera-Cortada, M. C. Cid, E. Campo, V. Amador, SOX11 promotes tumor angiogenesis through
599 transcriptional regulation of PDGFA in mantle cell lymphoma. *Blood* **124**, 2235–2247 (2014).

600 75. A. Orang, B. K. Dredge, C. Y. Liu, J. M. Bracken, C.-H. Chen, L. Sourdin, H. J. Whitfield, R. Lumb,
601 S. T. Boyle, M. J. Davis, M. S. Samuel, P. A. Gregory, Y. Khew-Goodall, G. J. Goodall, K. A.
602 Pillman, C. P. Bracken, Basonuclin-2 regulates extracellular matrix production and degradation. *Life*
603 *Sci Alliance* **6** (2023).

604 76. Y. Li, J. Zhang, P. Zhai, C. Hu, J. Suo, J. Wang, C. Liu, Z. Peng, The potential biomarker TIFA
605 regulates pyroptosis in sepsis-induced acute kidney injury. *Int Immunopharmacol* **115**, 109580
606 (2023).

607 77. M. D. Robinson, D. J. McCarthy, G. K. Smyth, edgeR: a Bioconductor package for differential
608 expression analysis of digital gene expression data. *Bioinformatics* **26**, 139–140 (2010).

609 78. S. A. John, J. L. Clements, L. M. Russell, L. A. Garrett-Sinha, Ets-1 regulates plasma cell
610 differentiation by interfering with the activity of the transcription factor Blimp-1. *J Biol Chem* **283**,
611 951–962 (2008).

612 79. H. Yamamoto, M. S. Lamphier, T. Fujita, T. Taniguchi, H. Harada, The oncogenic transcription factor
613 IRF-2 possesses a transcriptional repression and a latent activation domain. *Oncogene* **9**, 1423–
614 1428 (1994).

615 80. H. Cui, S. Banerjee, S. Guo, N. Xie, G. Liu, IFN Regulatory Factor 2 Inhibits Expression of Glycolytic
616 Genes and Lipopolysaccharide-Induced Proinflammatory Responses in Macrophages. *J Immunol*
617 **200**, 3218–3230 (2018).

81. D. J. Hodson, A. L. Shaffer, W. Xiao, G. W. Wright, R. Schmitz, J. D. Phelan, Y. Yang, D. E. Webster, L. Rui, H. Kohlhammer, M. Nakagawa, T. A. Waldmann, L. M. Staudt, Regulation of normal B-cell differentiation and malignant B-cell survival by OCT2. *Proc Natl Acad Sci U S A* **113**, E2039–46 (2016).

82. A. Cui, T. Huang, S. Li, A. Ma, J. L. Pérez, C. Sander, D. B. Keskin, C. J. Wu, E. Fraenkel, N. Hacohen, Dictionary of immune responses to cytokines at single-cell resolution. *Nature* **625**, 377–384 (2024).

83. S. Wang, J. Wang, V. Kumar, J. L. Karnell, B. Naiman, P. S. Gross, S. Rahman, K. Zerrouki, R. Hanna, C. Morehouse, N. Holoweckyj, H. Liu, Z. Manna, R. Goldbach-Mansky, S. Hasni, R. Siegel, M. Sanjuan, K. Streicher, M. P. Cancro, R. Kolbeck, R. Ettinger, IL-21 drives expansion and plasma cell differentiation of autoreactive CD11chiT-bet+ B cells in SLE. *Nature Communications* **9**, 1–14 (2018).

84. M. Terekhova, A. Swain, P. Bohacova, E. Aladyeva, L. Arthur, A. Laha, D. A. Mogilenko, S. Burdess, V. Sukhov, D. Kleverov, B. Echalar, P. Tsurinov, R. Chernyatchik, K. Husarcikova, M. N. Artyomov, Single-cell atlas of healthy human blood unveils age-related loss of NKG2CGZMBCD8 memory T cells and accumulation of type 2 memory T cells. *Immunity* **56**, 2836–2854.e9 (2023).

85. S. Ma, Z. Ji, B. Zhang, L. Geng, Y. Cai, C. Nie, J. Li, Y. Zuo, Y. Sun, G. Xu, B. Liu, J. Ai, F. Liu, L. Zhao, J. Zhang, H. Zhang, S. Sun, H. Huang, Y. Zhang, Y. Ye, Y. Fan, F. Zheng, J. Hu, B. Zhang, J. Li, X. Feng, F. Zhang, Y. Zhuang, T. Li, Y. Yu, Z. Bao, S. Pan, C. Rodriguez Esteban, Z. Liu, H. Deng, F. Wen, M. Song, S. Wang, G. Zhu, J. Yang, T. Jiang, W. Song, J. C. Izpisua Belmonte, J. Qu, W. Zhang, Y. Gu, G.-H. Liu, Spatial transcriptomic landscape unveils immunoglobin-associated senescence as a hallmark of aging. *Cell* **187**, 7025–7044.e34 (2024).

86. L. Duong, F. J. Pixley, D. J. Nelson, C. Jackaman, Aging Leads to Increased Monocytes and Macrophages With Altered CSF-1 Receptor Expression and Earlier Tumor-Associated Macrophage Expansion in Murine Mesothelioma. *Front Aging* **3**, 848925 (2022).

87. F. Angum, T. Khan, J. Kaler, L. Siddiqui, A. Hussain, The Prevalence of Autoimmune Disorders in Women: A Narrative Review. *Cureus* **12**, e8094 (2020).

88. M. K. Desai, R. D. Brinton, Autoimmune Disease in Women: Endocrine Transition and Risk Across the Lifespan. *Front Endocrinol (Lausanne)* **10**, 265 (2019).

89. A. Sziraki, Z. Lu, *Computational Pipeline for Processing EasySci Data* (2023; https://zenodo.org/record/8395492).

90. B. K. Martin, C. Qiu, E. Nichols, M. Phung, R. Green-Gladden, S. Srivatsan, R. Blecher-Gonen, B. J. Beliveau, C. Trapnell, J. Cao, J. Shendure, Optimized single-nucleus transcriptional profiling by combinatorial indexing. *Nat Protoc* **18**, 188–207 (2023).

91. J. Cao, D. R. O'Day, H. A. Pliner, P. D. Kingsley, M. Deng, R. M. Daza, M. A. Zager, K. A. Aldinger, R. Blecher-Gonen, F. Zhang, M. Spielmann, J. Palis, D. Doherty, F. J. Steemers, I. A. Glass, C. Trapnell, J. Shendure, A human cell atlas of fetal gene expression. *Science* **370** (2020).

92. L. McInnes, J. Healy, J. Melville, UMAP: Uniform Manifold Approximation and Projection for Dimension Reduction, *arXiv [stat.ML]* (2018). http://arxiv.org/abs/1802.03426.

93. Y. Hao, S. Hao, E. Andersen-Nissen, W. M. Mauck 3rd, S. Zheng, A. Butler, M. J. Lee, A. J. Wilk, C. Darby, M. Zager, P. Hoffman, M. Stoeckius, E. Papalexi, E. P. Mimitou, J. Jain, A. Srivastava, T. Stuart, L. M. Fleming, B. Yeung, A. J. Rogers, J. M. McElrath, C. A. Blish, R. Gottardo, P. Smibert, R. Satija, Integrated analysis of multimodal single-cell data. *Cell* **184**, 3573–3587.e29 (2021).

94. Y. Zhang, T. Liu, C. A. Meyer, J. Eeckhoute, D. S. Johnson, B. E. Bernstein, C. Nusbaum, R. M. Myers, M. Brown, W. Li, X. S. Liu, Model-based analysis of ChIP-Seq (MACS). *Genome Biol.* **9**, R137 (2008).

95. J. Schug, W.-P. Schuller, C. Kappen, J. M. Salbaum, M. Bucan, C. J. Stoeckert Jr, Promoter features related to tissue specificity as measured by Shannon entropy. *Genome Biol* **6**, R33 (2005).

96. H. K. Finucane, Y. A. Reshef, V. Anttila, K. Slowikowski, A. Gusev, A. Byrnes, S. Gazal, P.-R. Loh, C. Lareau, N. Shoresh, G. Genovese, A. Saunders, E. Macosko, S. Pollack, Brainstorm Consortium, J. R. B. Perry, J. D. Buenrostro, B. E. Bernstein, S. Raychaudhuri, S. McCarroll, B. M. Neale, A. L. Price, Heritability enrichment of specifically expressed genes identifies disease-relevant tissues and cell types. *Nat Genet* **50**, 621–629 (2018).

97. D. A. Cusanovich, A. J. Hill, D. Aghamirzaie, R. M. Daza, H. A. Pliner, J. B. Berletch, G. N. Filippova, X. Huang, L. Christiansen, W. S. DeWitt, C. Lee, S. G. Regalado, D. F. Read, F. J. Steemers, C. M. Disteche, C. Trapnell, J. Shendure, A Single-Cell Atlas of In Vivo Mammalian Chromatin Accessibility. *Cell* **174**, 1309–1324.e18 (2018).

98. E. Sollis, A. Mosaku, A. Abid, A. Buniello, M. Cerezo, L. Gil, T. Groza, O. Güneş, P. Hall, J. Hayhurst, A. Ibrahim, Y. Ji, S. John, E. Lewis, J. A. L. MacArthur, A. McMahon, D. Osumi-Sutherland, K. Panoutsopoulou, Z. Pendlington, S. Ramachandran, R. Stefancsik, J. Stewart, P. Whetzel, R. Wilson, L. Hindorff, F. Cunningham, S. A. Lambert, M. Inouye, H. Parkinson, L. W. Harris, The NHGRI-EBI GWAS Catalog: knowledgebase and deposition resource. *Nucleic Acids Res* **51**, D977–D985 (2023).

99. T. Stuart, A. Srivastava, S. Madad, C. A. Lareau, R. Satija, Single-cell chromatin state analysis with Signac. *Nat Methods* **18**, 1333–1341 (2021).

100. J. A. Castro-Mondragon, R. Riudavets-Puig, I. Rauluseviciute, R. B. Lemma, L. Turchi, R. Blanc-Mathieu, J. Lucas, P. Boddie, A. Khan, N. Manosalva Pérez, O. Fornes, T. Y. Leung, A. Aguirre, F. Hammal, D. Schmelter, D. Baranasic, B. Ballester, A. Sandelin, B. Lenhard, K. Vandepoele, W. W. Wasserman, F. Parcy, A. Mathelier, JASPAR 2022: the 9th release of the open-access database of transcription factor binding profiles. *Nucleic Acids Res* **50**, D165–D173 (2022).

101. Z. Gu, R. Eils, M. Schlesner, Complex heatmaps reveal patterns and correlations in multidimensional genomic data. *Bioinformatics* **32**, 2847–2849 (2016).

7. Z. Zhang, C. Schaefer, W. Jiang, Z. Lu, J. Lee, A. Sziraki, A. Abdulraouf, B. Wick, M. Haeussler, Z. Li, G. Molla, R. Satija, W. Zhou, J. Cao, A panoramic view of cell population dynamics in mammalian aging. Science 387, eadn3949 (2025).